NANO-FABRICATION OF CELLULAR FORCE SENSORS AND SURFACE COATINGS VIA DENDRITIC SOLIDIFICATION

by

GOVIND PANERU

B. Sc. Tribhuvan University, Kathmandu, Nepal, 2002
M. Sc. Tribhuvan University, Kathmandu, Nepal, 2004

AN ABSTRACT OF A DISSERTATION

submitted in partial fulfillment of the requirements for the degree

DOCTOR OF PHILOSHOPY

Department of Physics
College of Arts and Sciences

KANSAS STATE UNIVERSITY
Manhattan, Kansas

2014

Abstract

Directed electrochemical nanowire assembly (DENA) is a method for fabricating nano-structured materials via electrochemical dendritic solidification. This thesis presents two new applications of nano-structured materials that are fabricated via the DENA methodology: cellular force sensors to probe adhesive sites on living cells and single-crystalline metallic dendrites as surface coating materials.

Fast migrating cells like *D. discoideum*, leukocytes, and breast cancer cells migrate by attachment and detachment of discrete adhesive contacts, known as *actin foci*, to the substrate where the cell transmits traction forces. Despite their importance in migration, the physics by which actin foci bind and release substrates is poorly understood. This gap is largely due to the compositional complexity of actin foci in living cells and to a lack of technique for directly probing these sub-cellular structures. Recent theoretical work predicts these adhesive structures to depend on the density of adhesion receptors in the contact sites, the receptor-substrate potential, and cell-medium surface tension. This thesis describes the fabrication of sub-microscopic force sensors composed of poly(3,4-ethylene dioxythiophene) fibers that can interface directly with sub-cellular targets such as actin foci. The spring constants of these fibers are in the range of 0.07-430 nN μm^{-1}. These fibers were used to characterize the strength and lifetime of adhesion between the single adhesive contacts of *D. discoideum* cells and the fibers, finding an average force of 3.1 ± 2.7 nN and lifetime of 23.4 ± 18.5 s. This capability is significant because direct measurement of these properties will be necessary to measure the cell-medium surface tension and to characterize the receptor-substrate potential in the next (future) stage of this project.

The fabrication of *smart* materials that are capable of the high dynamic range structural reconfiguration would lead to their use to confer hydrophobic, lipophobic, and anti-corrosive character to substrates in a *regenerative* manner. As a step towards this goal, we have extended the DENA method to enable repetitive growth and dissolution of metallic dendrites to substrates. The experimental parameters that control this process are the frequency and duty cycle of the alternating voltage signal that initiates the dendritic growth.

NANO-FABRICATION OF CELLULAR FORCE SENSORS AND SURFACE COATINGS VIA DENDRITIC SOLIDIFICATION

by

GOVIND PANERU

B. Sc. Tribhuvan University, Kathmandu, Nepal, 2002
M. Sc. Tribhuvan University, Kathmandu, Nepal, 2004

A DISSERTATION

submitted in partial fulfillment of the requirements for the degree

DOCTOR OF PHILOSHOPY

Department of Physics
College of Arts and Sciences

KANSAS STATE UNIVERSITY
Manhattan, Kansas

2014

Approved by:

Major Professor
Bret N Flanders

Copyright

Abstract

Directed electrochemical nanowire assembly (DENA) is a method for fabricating nano-structured materials via electrochemical dendritic solidification. This thesis presents two new applications of nano-structured materials that are fabricated via the DENA methodology: cellular force sensors to probe adhesive sites on living cells and single-crystalline metallic dendrites as surface coating materials.

Fast migrating cells like *D. discoideum*, leukocytes, and breast cancer cells migrate by attachment and detachment of discrete adhesive contacts, known as *actin foci*, to the substrate where the cell transmits traction forces. Despite their importance in migration, the physics by which actin foci bind and release substrates is poorly understood. This gap is largely due to the compositional complexity of actin foci in living cells and to a lack of technique for directly probing these sub-cellular structures. Recent theoretical work predicts these adhesive structures to depend on the density of adhesion receptors in the contact sites, the receptor-substrate potential, and cell-medium surface tension. This thesis describes the fabrication of sub-microscopic force sensors composed of poly(3,4-ethylene dioxythiophene) fibers that can interface directly with sub-cellular targets such as actin foci. The spring constants of these fibers are in the range of 0.07-430 nN μm^{-1}. These fibers were used to characterize the strength and lifetime of adhesion between the single adhesive contacts of *D. discoideum* cells and the fibers, finding an average force of 3.1 ± 2.7 nN and lifetime of 23.4 ± 18.5 s. This capability is significant because direct measurement of these properties will be necessary to measure the cell-medium surface tension and to characterize the receptor-substrate potential in the next (future) stage of this project.

The fabrication of *smart* materials that are capable of the high dynamic range structural reconfiguration would lead to their use to confer hydrophobic, lipophobic, and anti-corrosive character to substrates in a *regenerative* manner. As a step towards this goal, we have extended the DENA method to enable repetitive growth and dissolution of metallic dendrites to substrates. The experimental parameters that control this process are the frequency and duty cycle of the alternating voltage signal that initiates the dendritic growth.

Table of Contents

List of Figures

List of Tables

Acknowledgements

I would like express my sincere gratitude to my advisor Professor Bret Flanders for having me in his group for the past five and half years. His continuous guidance, encouragement and support helped me at all time of my research and writing of this thesis. I am indebted to Professor Larry Weaver for his numerous helpful advices and insightful discussions on the theoretical parts of this thesis. I am also grateful to my PhD committee members, Professors Chris Sorensen, Bruce Law, Ryszard Jankowiak, and Om Prakash. Their insightfulness and suggestions are of immense value.

I am thankful to all the former members of the Flanders group. Especially, I would like to thank Dr. Prem Thapa for helping me to learn some of the experimental skills and his contribution to this work. I would like to thank Professor Bruce Law and his former student Dr. Sean McBride for their collaboration to take AFM measurements. I would also like to thank all my mentors from department of physics at KSU and from my home country Nepal.

I would like to thank my parents for their constant guidance and encouragement throughout my life. I would like to thank my wife Sangam for her constant support to achieve this rewarding journey. Finally, I would like to acknowledge my lovely children Manaswi and Samwat. They are my source of inspiration.

Chapter 1 - Introduction

1.1. Overview of thesis

With the advent of nanotechnology, fabrication of nanoscale materials has stimulated great interest due to their importance in basic scientific research and potential technological applications. We are interested in two directions of application in this general area: mechanical probe methodologies for biological studies at the single cellular level and surface coating methodologies for corrosion and bio-fouling control. Key challenges lie in controlling the nanoscale and microscale dimensions of the material, and in controlling the composition of the material. To meet these requirements, we need to better understand the fabrication mechanism. The primary method by which we fabricate the nano-structured materials is *directed electrochemical nanowire assembly* (DENA).[1, 2] DENA is an electrochemical method based on dendritic solidification.[3-7] We have demonstrated two newer controls over the DENA methodology: control over the length and the radius of the polymeric fibers and the ability to quickly and completely structurally reconfigure (growth followed by dissolution) metallic fibers and dendrites on conducting surfaces. Control over fiber-length and radius provides control over their stiffness and thereby enables the fabrication of fibers that have stiffness comparable to the stiffness of living cells; as a result, such fibers are useful as cellular force probes. The ability to structurally reconfigure metallic dendrites would lead to the fabrication of surface coating materials that provide wettability and adhesion control and that have potential for use as environmentally adaptive *smart* materials.

1.1.1. Adhesion dynamics of fast migrating cells

Cell-substrate adhesion is essential in many physiological processes, such as tissue growth, cellular development, cellular migration, and wound healing. Depending on migration speed, there are two types of cells: slow migrating cells (speed 5-10 μm/hr),[8] and fast migrating cells (speed 10 μm/min)[9]. The mechanism underlying cell-substrate adhesion is well characterized in slow migrating cells, like fibroblasts.[10] Fibroblasts express many discrete ~1 μm diameter adhesive contacts to a substrate at a given time. These well-studied contacts are called *focal adhesions* and are distributed on their basal surfaces. *Focal adhesions* are composed of integrins, a transmembrane glycoprotein that is involved in cell-substrate adhesion.[11] The *focal adhesions* are internally connected to the actin filaments via intracellular linkers like talin, paxillin, and vinculin, and thereby allow cells to transmit traction force to the substratum.[12] A typical lifetime of a single focal adhesion is greater than 20 min;[13] due to the long-lasting nature of these integrin-based adhesive contacts, cells that utilize them can only migrate at rather slow rates.

The mechanism underlying cell-substrate adhesion in fast migrating cells (speed 10 μm/min)[9] like *D. discoideum*,[14] leukocytes,[15] and breast cancer cells[16] is poorly understood, but depends on the establishment of adhesive contacts to the substrate where the cell transmits traction forces. In pre-aggregative *D. discoideum*, these adhesive contacts are discrete complexes known as *actin-foci*.[17, 18] These contacts are different from focal adhesions; they have an area of ~ 0.5 μm^2 and a lifetime of only ~ 20 s.[17] The actin foci are composed of polymerized form of actin, and are connected internally to the actin meshwork.[17] A cell typically expresses ~20 actin foci with a (glass) substrate at a time. The surface area of a typical *D. discoideum* is

~300 μm^2, so these complexes are both small and dynamic. The dynamics are fundamental to the migratory properties, as the cell must release the substrate in order to move. We (naively) recover the migration rate for a 10 μm diameter cell by assuming first order kinetics for the decay of the ~20 actin foci and taking $\frac{10\mu m}{(20s)\ln 20} \approx 10\mu m/min$. Despite their importance in migration, the physics by which actin foci bind and release the substrates is not known.[17, 19] This gap is due largely to the compositional complexity of the actin foci in living cells and to lack of a technique for directly probing these sub-cellular structures. It is important to push through these barriers because insight into how these adhesive contacts work would potentially facilitate improved strategies for controlling adhesion and, thereby, migration, in cells that share the amoeboid paradigm of movement. The future goal of this project is to understand the adhesion and de-adhesion mechanism of actin foci. As a step towards our long term goal, this thesis presents methodology for fabricating cantilevered force sensors that are capable of directly probing the actin foci of *D. discoideum* cells without making unintentional secondary contacts to the cell.

The *significance* of having developed this methodology is as follows. We have designed sub-microscopic force sensors for measuring the adhesive forces and lifetimes of individual actin foci of *D. discoideum* cells. Recently, Brochard-Wyart and de Gennes have presented a general theory for the rupture of adhesive contacts by pulling forces.[20, 21] We have adapted this theory to describe actin-foci rupture, where an actin focus is taken to consist of multiple receptor-substrate bonds (R-S bonds). In order to test this theory, the cell-medium surface tension, the surface density of adhesion receptors, and the potential energy well that describes the interaction between the adhesion receptors and the substrate must be measured. The force sensors will

allow for the quantification of two of these three properties: the cell-medium surface tension and the potential energy well of a single R-S bond.

1.1.2. Structural reconfiguration of metallic dendrites

The fabrication of *smart* materials that are capable of high dynamic range structural reconfiguration that, say, cuttlefish-skin[22] or photosynthetic corals[23] are capable of, would permit hydrophobic, lipophobic, and anti-corrosive character to be conferred to substrates in a *regenerative* manner. To this end, a number of materials have been developed in the past few years that exhibit high dynamic range structural reconfiguration. Regan and co-workers have synthesized smart gels with pore-sizes sufficient to trap 26 kDa proteins and which exhibit complete, salinity-dependent dissolution (and cargo-release) and reformation.[24] Pine and co-workers have designed colloidal magnetic building blocks that self-assemble into aggregates with reproducible geometries. These configurations can be fully disassembled and then re-assembled by controlling the external magnetic field or the salinity of the solution.[25] To realize the reconfigurable assemblies, both of these studies employed specialized building blocks—modular peptides for the smart gels and quasi-monopolar magnets for the colloids—that switches its character in response to a changing external field. It would be advantageous if one could control the assembly and disassembly process of more fundamental building blocks, such as the components of salts, found in naturally occurring environments such as oceans or rivers. This ability could then lead to the fabrication of nanostructured coatings on the surfaces immersed in such environments in order to provide corrosion, reflectivity, or adhesion control that could be regenerated as needed.[26-28]

As a step towards this end, this thesis extends the DENA methodology to enable the complete dissolution of an array of single crystalline gold dendrites following their growth on conducting surfaces from their simple salt solutions. DENA is an *electrochemical* technique based on the dendritic solidification that occurs when the growth of a crystal is limited by the diffusion of the building blocks through a bulk medium to the solidification front. In DENA, the driving force that induces the diffusion of the building blocks is the alternating electric field applied to the metallic salt solution. In addition to the bulk diffusion, electrochemical crystallization depends on the electrochemical oxidation and reduction of metal atoms at the crystal-solution interface. We can control both the overall size and the diameter of the dendrites, thereby providing both micro- and nanoscale control. Hence, the structural reconfiguration of arrays of such dendrites holds promise as surface modifications that provide reconfigurable or self-healing wettability and adhesion control.

1.2. References

1. I. Talukdar, B. Ozturk, T. D. Mishima and B. N. Flanders, *Appl. Phys. Lett.*, 2006, **88**, 221907.
2. P. S. Thapa, B. J. Ackerson, D. R. Grischkowsky and B. N. Flanders, *Nanotechnology*, 2009, **20**, 235307.
3. G. E. Nash and M. E. Glicksman, *Acta Metall.*, 1974, **22**, 1291.
4. S. C. Huang and M. E. Glicksman, *Acta Metall.*, 1981, **29**, 701-715.
5. S. C. Huang and M. E. Glicksman, *Acta Metall.*, 1981, **29**, 717-734.
6. J. S. Langer, *Rev. Mod. Phys.*, 1980, **52**, 1-28.
7. D. A. Kessler, J. Koplik and H. Levine, *Adv. Phys.*, 1988, **37**, 255-339.
8. S. Park, D. Koch, R. Cardenas, J. Käs and C. K. Shih, *Biophysical Journal*, 2005, **89**, 4330-4342.
9. N. Andrew and R. H. Insall, *Nature Cell Biology*, 2007, **9**, 193-U191.
10. V. Petit and J.-P. Thiery, *Biology of the Cell*, 2000, **92**, 477-494.
11. X.-D. Ren, W. B. Kiosses, D. J. Sieg, C. A. Otey and D. D. Schlaepfer, *Journal of Cell Science*, 2000, **113**, 3673-3678.
12. K. A. Beningo, M. Dembo, I. Kaverina, J. V. Small and Y. L. Wang, *Journal of Cell Biology*, 2001, **153**, 881-888.

13. X. S. Ren, W. B. Kiosses, D. J. Sieg, C. A. Otey, D. D. Schlaepfer and M. A. Schwartz, *J. Cell .Sci.*, 2000, **113**, 3673-3678.
14. H. Bodeker, C. Beta, T. Frank and E. Bodenschatz, *Eur. Phys. J* 2010, **90**, 28005.
15. P. Friedl, S. Borgmann and E. B. Broecker, *J. Leukoc. Biol.*, 2001, **70**, 491-509.
16. A. Muller, B. Homey, H. Soto, N. F. Ge, D. Catron, M. E. Buchanan, T. McClanahan, E. Murphy, W. Yuan, S. N. Wagner, J. L. Barrera, A. Mohar, E. Verastegui and A. Zlotnik, *Nature*, 2001, **410**, 50-56.
17. K. S. K. Uchida and S. Yumura, *J. Cell .Sci.*, 2004, **117**, 1443-1455.
18. S. Yumura and T. Kitanishi-Yumura, *Cell Struct. Funct.*, 1990, **15**, 355-364.
19. A. S. Kowal and R. L. Chisholm, *Eukaryotic Cell*, 2011, **10**, 662-671.
20. F. Brochard-Wyart and P. G. deGennes, *C. R. Physique*, 2003, **4**.
21. S. Pierrat, F. Brochard-Wyart and P. Nassoy, *Biophysical Journal*, 2004, 2855-2869.
22. R. Hanlon, *Curr. Biol.*, 2007, **17**, R400-R404.
23. B. Brown and S. Gibb, *Journal of Experimental Marine Biology and Ecology*, 2002, **277**, 129-144.
24. T. Z. Grove, C. O. Osuji, J. D. Forster, E. R. Dufresne and L. Regan, *J. Am. Chem. Soc.*, 2010, **132**, 14024-14026.
25. S. Sacanna, L. Rossi and D. J. Pine, *J. Am. Chem. Soc.*, 2012, **134**, 6112-6115.
26. W. H. Hilbertz, *IEEE J. Oceanic Engineering*, 1979, **OE-4**, 94-113.
27. A. Neville and A. P. Morizot, *J. Crystal Growth*, 2002, **243**, 490-502.
28. M. H. Lee, K. M. Moon, J. D. Kim, K. Jun and K. H. Kim, *Trans. Nonferrous met. Soc. China*, 2009, **19**, s110-s113.

Chapter 2 - Theoretical model for cell-substrate adhesion in fast migrating cells

2.1. Introduction

D. discoideum cells migrate on substrates by establishing discrete adhesive contacts known as *actin foci*. The actin foci of *D. discoideum* express a variety of cell-substrate adhesion molecules such as *sibA-E*,[1, 2] *sadA*,[3-5] talin,[1, 6] and cortexillin I.[3] The mean lifetime of an actin focus is short: ~20 s.[7] There is need of a theory that will explain the experimentally measured strength and lifetimes of actin foci. This chapter presents a theoretical model that describes adhesion dynamics of actin foci and in particular, it provides an expression for the lifetime of actin foci as a function of pulling force. This theory will be significant to interpret the physics by which fast migrating cells rapidly migrate on substrates.

2.2. Theory

Figure 2.1(a) shows a cell of size R that has adhered to a substrate. The contact area has a radius R_C and contact angle θ. When the cell is pulled with force F, $R_C(t)$ diminishes and $\theta(t)$ increases until the adhesion ruptures. Brochard-Wyart and de Gennes (BWdG) wrote a general theory for this process in 2003[8] as an extension of the classic Bell[9] and Evans[10] models. This theory has served as the basis for several recent studies on rupture by pulling forces[11] and spreading by pushing forces[12] of both vesicles and live cells.[13] The geometry for which BWdG theory was originally developed is shown in Figure 2.1(a). Next we illustrate our direct application of this theory to actin foci.

Cell-substrate contacts by *D. discoideum* consist of numerous, submicron feet. These feet, also called actin foci, make direct contact with the substrate. Each actin-focus is of sub-micron size; typically, numerous actin foci exist between a cell and the substrate, as opposed to the uniform contact across the whole base of the cell that figure 2.1(a) shows. Figure 2.1(b) illustrates this case of discrete contacts. Below we describe a probe that we have engineered to

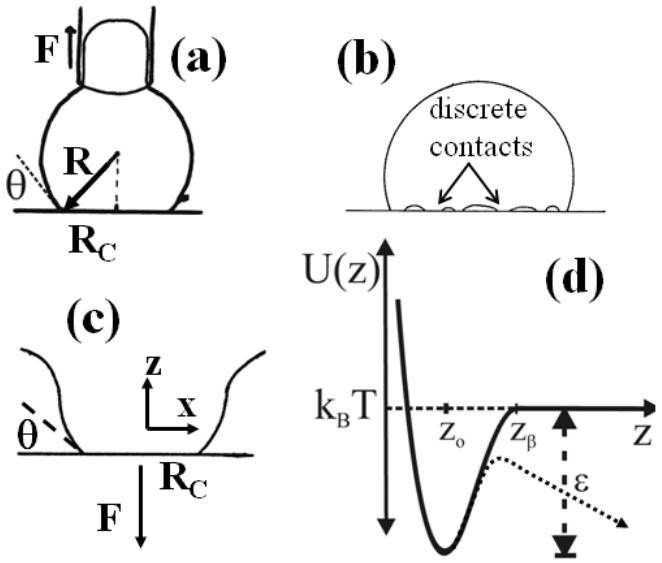

Figure 2.1. (a) Schematic of an aspirated cell or vesicle with uniform contact to substrate. This situation is that for which BWdG theory was originally developed. (b) Sketch of *D. discoideum* cell with discrete contacts to substrate. (c) Enlarged view of a single, discrete contact. (d) Potential energy well describing a single R-S bond.

pull with a known force F on a single actin focus. This situation is depicted in figure 2.1(c). Here we apply BWdG, to this mesoscopic geometry, in order to describe how R_C changes

(decreases) as a function of the applied force *F*. The adhesiveness of a given mesoscopic contact is due to numerous molecular-level receptor-substrate (R-S) bonds within the contact area.

When force *F* is applied to the contact, it first acts on the outermost annulus of receptor-R-S bonds in the contact. We assert that the applied force *F* is (primarily) balanced by uniform stretching of the membrane around a circular contact line. Hence, [8]

$$F \cong 2\pi R_C \gamma \sin\theta \qquad (1a)$$

$$\overline{F} \cong R_C \theta / C, \qquad (1b)$$

where γ is the cell-medium surface tension, and θ the contact angle. The second equality in (1b) invokes the small angle approximation and sets $\overline{F} = F / 2\pi\gamma C$ where C is an undetermined length that will cancel out; its purpose is to simplify (1b) by making $\overline{F}$ unitless. The binding of intracellular actin filaments to the contact would alter the simple balance of forces in (1); experimentally, we are able to investigate contacts that are unbound to intracellular f-actin.

The annulus of bonds has area $2\pi R_C a$ where *a* is the lateral width of a receptor. There are $N = 2\pi R_C a \Gamma$ of these bonds, where Γ is the surface density of *R-S* bonds. *N* will decrease in time as R_C diminishes. The per site force *f* is of order *F/N*. The first law of thermodynamics states $\Delta U = Q + W_{on}$, where ΔU is the change in internal energy of the system, *Q* is the amount of heat, and W_{on} is the work done on the system. We assume that the internal energy *U* of the system of R-S bonds remains constant *i.e.*, $\Delta U = 0$. So, all work done by pulling on the *R-S* bond is dissipated as heat *Q*. This situation is analogous isothermal compression of an ideal gas or stretching a rubber band. The rate at which work is done in breaking the bonds is

$$\dot{W}_{on} = Nf\frac{dz}{dt}, \tag{2a}$$

where f is the applied force on a R-S bond in the contact area and z is the out-of-equilibrium displacement along the bond axis. By expressing N as $2\pi R_C \Gamma a$, (2a) becomes:

$$\dot{W}_{on} = 2\pi R_C \Gamma a f\frac{dz}{dt}. \tag{2b}$$

$\frac{dz}{dt} = v_z$ is the average vertical velocity of a receptor when bond breaks. Equation (2b) has three unknowns: f, v_z, and $\dot{W}_{on}$. However, f can be re-expressed in terms of v_z, using Kramers theory.[14] This step is described below.

Figure 2.1(d) shows the potential energy well associated with a single *R-S* bond. The depth of this well is ε. The basic chemical reaction associated with this well is

$$R - S \underset{k_+}{\overset{k_-}{\leftrightarrow}} R + S, \tag{3}$$

where k_- and k_+ are the dissociation and rebinding rate constants, respectively. The average velocity of a receptor when a bond breaks v_z equals the molecular distance z_β at which the bond breaks multiplied by the probability per time k_- to move that distance. k_- is the product of an attempt frequency ν (of order 10^9 s^{-1})[15] multiplied by a Boltzmann factor $e^{-\varepsilon/kT}$ for the probability of a thermal fluctuation of order ε; the well-depth of the unstressed potential. If there is no external force on the bond, k_- is called k_o, which is defined as

$$k_0 = \nu e^{-\frac{\varepsilon}{kT}} \tag{4a}$$

The application of a macroscopic force F to the actin foci translates into a microscopic force f on single R-S bond. We expect the external force f on the R-S bond to amplify the dissociation rate

constant k_- by lowering the barrier to *R-S* dissociation [figure 2.1(d), dotted profile]; following Kramers,[14] this amplification is described as

$$k_- = k_0 e^{\frac{f}{f_\beta}} \tag{4b}$$

In (5b), $f_\beta = kT/z_\beta$ is the intrinsic force scale and k_0 is called the unstressed off-rate.[14] In this view, f is the slope of the mechanical potential shown by the dotted line in figure 2.1(d). Hence,

$$v_z = v_1 e^{\frac{f.z_\beta}{kT}}, \tag{5a}$$

where $v_1 = z_\beta k_0$.

From (5a),

$$fz_\beta = kT\, ln\left(\frac{v_z}{v_1}\right). \tag{5b}$$

Inserting (5b) into (2b) yields:

$$\dot{W}_{on} = 2\pi R_C \Gamma \frac{a}{z_\beta} kT\, ln(\frac{v_z}{v_1})\frac{dz}{dt}. \tag{6}$$

A microscopic formulation of work of adhesion G_{Ad} (work per area) is found by integrating (6) with respect to time until the detachment is complete and dividing by the area of the annulus:

$$\begin{aligned} G_{Ad} &= \frac{1}{2\pi R_C a}\int \dot{W}_{on} dt \\ &= \frac{\Gamma}{z_\beta} kT \int ln\left(\frac{v_z}{v_1}\right)\frac{dz}{dt} dt \end{aligned}. \tag{7a}$$

$ln(\frac{v_z}{v_1})$ varies slowly in time relative to $\frac{dz}{dt}$. Then, (7a) is approximately written as

$$G_{Ad} \cong \frac{\Gamma kT}{z_\beta} ln(\frac{v_z}{v_1}) \int_0^{z_\beta} dz$$
$$= \Gamma kT\, ln(\frac{v_z}{v_1}) \quad , \tag{7b}$$

or
$$G_{Ad} = \Gamma kT\, ln(\frac{v_z}{v_1}) . \tag{7c}$$

Macroscopically, we know that G_{Ad} is related to the contact angle θ:[16]

$$G_{Ad} = \gamma(1 - cos\,\theta)$$
$$\cong \frac{1}{2}\gamma\theta^2 , \tag{8a}$$

or
$$G_{Ad} = \frac{1}{2}\gamma \frac{\overline{F}^2 C^2}{R_C^2} , \tag{8b}$$

where equation (1b) was used to attain 8(b). Equating (7c) and (8b) relates the microscopic bond dynamics to the macroscopic applied force $\overline{F}$, leading to:

$$v_z = v_1 e^{\overline{F}^2 C^2 / \alpha R_C^2} , \tag{9}$$

where $\alpha = 2\Gamma kT / \gamma$. α essentially compares the adhesion energy to the stretching energy. Using the axes imposed on figure 2.1(c) and chain rule, v_z may be re-written as

$$v_z = -\frac{dz}{dx}\frac{dR_C}{dt} . \tag{10}$$

Equating (9) and (10), we arrive at a differential equation that describes how R_C decays in time in response to the applied force:

$$\frac{dR_C}{dt} = -\frac{v_1}{\delta} e^{\frac{\overline{F}^2 C^2}{\alpha R_C^2}} , \tag{11}$$

where $\delta=dz/dx$, which we approximate as a constant of order 1. Equation (11) is a first order nonlinear differential equation. Rather than integrate (11) directly, which appears to defy analytic solution, we approximate its solution by the following set of steps. First, we define

$$\phi = e^{\overline{F}^2/\alpha\psi^2}, \tag{12a}$$

$$\psi = \frac{R_C}{C}. \tag{12b}$$

Differentiating ϕ with respect to t we get

$$\frac{d\phi}{dt} = e^{\overline{F}^2/\alpha\psi^2}\left(\frac{\overline{F}^2}{\alpha}\right)\left(-\frac{2}{\psi^3}\right)\frac{d\psi}{dt}, \tag{13a}$$

which can further be simplified as

$$\frac{d\phi}{dt} = \phi\left(-\frac{2\overline{F}^2}{\alpha}\right)\frac{1}{\psi^3}\left(\frac{1}{C}\frac{dR_C}{dt}\right). \tag{13b}$$

Substituting for $\frac{dR_C}{dt}$ using (11) we obtain,

$$\frac{d\phi}{dt} = \phi^2\left(\frac{2\overline{F}^2 v_1}{\alpha C}\right)\frac{1}{\psi^3} \tag{14}$$

where we took $\delta \sim 1$.

From (12a), $\frac{1}{\psi^3} = \left(\frac{\alpha \ln\phi}{\overline{F}^2}\right)^{3/2}$, and we approximate the logarithmic term as constant i.e., $\ln\phi \cong \ln\phi_0$.[8] Then, (14) becomes

$$\frac{d\phi}{dt} \cong \frac{2v_1\alpha^{1/2}}{C\overline{F}}(\ln\phi_0)^{3/2}\phi^2,$$

or

$$\frac{d\phi}{dt} = C_2\phi^2, \tag{15}$$

where $$C_2 = \frac{2\nu_1 \alpha^{1/2}}{C\overline{F}} (ln\phi_0)^{3/2}. \quad (16)$$

Equation (15) is in a form that can be solved directly, yielding a solution for R_C. The solution to (15) is found by integrating $\int_{\phi_0}^{\phi} \frac{d\phi}{\phi^2} = C_2 \int_0^t dt$, to obtain

$$ln\phi = ln\phi_0 - ln\left(1 - \frac{t}{\tau_s}\right), \quad (17)$$

where $\tau_s = C_2\phi_0$. We will see that τ_s sets the time scale for decay of an adhesive contact.

From (12a), we see that $ln\phi = \overline{F}^2 / \alpha\psi^2$ and $ln\phi_0 = \overline{F}^2 / \alpha\psi_0^2$. Substituting these values into (17) and using (12b), we obtain

$$R_C(t) = \left[\left(\frac{1}{R_{CO}}\right)^2 - \frac{8\pi^2 \Gamma\gamma kT}{F^2} ln\left(1 - \frac{t}{\tau_s}\right)\right]^{-1/2}, \quad (18)$$

$$\tau_s = \frac{F}{4\pi\gamma\nu_1\alpha^{1/2}} e^{-\frac{F^2}{4\pi^2\gamma^2 R_{CO}^2 \alpha}}. \quad (19)$$

R_{CO} is the initial contact radius, and τ_s is the decay time. Equation (18) is the analytic solution for $R_C(t)$. A representative plot of R_C vs t is shown in figure 2.2. The plot shows that the contact radius R_C decreases suddenly after some time. This is because the applied force F ruptures the R-S bonds in an *outside-in* manner. As time increases, the outer bonds decay and the applied force becomes concentrated on the relatively fewer inner bonds. (Recall that N decreases as R

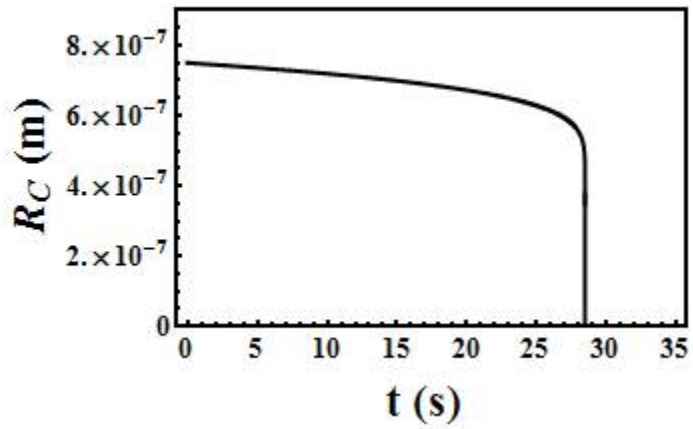

Figure 2.2. Plot of R_C vs t.

decreases in time). As a result, after an initial period where R_C changes slowly, the contact rapidly ruptures and detaches from the substrate. The contact has a characteristic time τ_s which decreases with increasing force; when $t = \tau_s$, the bracketed term diverges, $R_C(t) \to 0$, and the cluster ruptures completely. Note that $v_1 = z_\beta k_0$. Hence, testing this theory will require measurement of the receptor density Γ, the cell-medium surface tension γ, the unstressed off rate k_0 and the spatial extent of the potential z_β. However, in practice, k_0 dictates the time-scale of the detachment more so than other parameters in (19) due to its strong dependence on the well-depth $k_0 = \nu e^{-\frac{\varepsilon}{kT}}$. Thus, critical to understanding detachment is to understand the R-S potential energy well. In the following chapters, we present methodology for the fabrication of sub-micron force probes that will be used to characterize this potential in future work.

2.3. References

1. S. Cornillon, L. Gebbie, M. Benghezal, P. Nair, S. Keller, B. Wehrle-Haller, S. J. Charette, F. Bruckert, F. Letourneur and P. Cosson, *EMBO Reports*, 2006, **7**, 617-621.
2. S. Cornillon, R. Froquet and P. Cosson, *Eukaryotic Cell*, 2008, **7**, 1600-1605.
3. A. S. Kowal and R. L. Chisholm, *Eukaryotic Cell*, 2011, **10**, 662-671.
4. P. Fey, S. Stephens, M. A. Titus and R. L. Chisholm, *J. Cell. Biol.*, 2002, **159**, 1109-1119.
5. N. P. Barry and M. S. Bretscher, *Proc. Natl. Acad. Sci.*, 2010, **107**, 11376-11380.
6. J. Niewohner, I. Weber, M. Maniak, A. Muller-Taubenberger and G. Gerisch, *J. Cell. Biol.*, 1997, **138**, 349-361.
7. K. S. K. Uchida and S. Yumura, *J. Cell .Sci.*, 2004, **117**, 1443-1455.
8. F. Brochard-Wyart and P. G. deGennes, *C. R. Physique*, 2003, **4**.
9. G. I. Bell, *Science*, 1978, **200**, 618-627.
10. E. Evans, D. Berk and A. Leung, *Biophysical Journal*, 1991, **59**, 838-848.
11. S. Pierrat, F. Brochard-Wyart and P. Nassoy, *Biophysical Journal*, 2004, 2855-2869.
12. D. Cuvelier and P. Nassoy, *Physical Review Letters*, 2004, **93**, 228101.
13. M.-J. Colbert, A. N. Raegen, C. Fradin and K. Dalnoki-Veress, *Eur. Phys. J. E*, 2009, **30**, 117-121.
14. P. Hänggi, P. Talkner and M. Borkovec, *Rev. Mod. Phys.*, 1990, **62**, 251-342.
15. R. Merkel, P. Nassoy, A. Leung, K. Ritchie and E. Evans, *Nature*, 1999, **397**, 50-53.
16. J. Israelachvili, *Intermolecular & Surface Forces*, Academic Press, London, 1992.

Chapter 3 - Design and Performance of Experimental Equipment

3.1. Introduction

This chapter details the experimental techniques used in this work. The first part of this chapter describes the methodology for the fabrication of cellular force sensors composed of poly(3,4-ethylene dioxythiophene) poly(sodium styrene sulfonate) (PEDOT:PSS) fibers using a technique called *directed electrochemical nanowire assembly* (DENA). These fibers are capable of probing submicron sized adhesive contacts like actin foci of living cells without making an unintentional secondary contact with the cell. We have described the methodology to characterize the duration and strength of adhesion between the actin foci of highly migratory *D. discoideum* cells and the fiber. The later part of this chapter describes our methodology of fabrication of single crystalline metallic nanowires and nano-dendrites at the tips of movable electrodes. We also describe methodology for performing cyclic voltammetry of single gold dendrites.

3.2. Nanofiber Growth

3.2.1. Preparation of electrode for nanofiber growth

Our group fabricates metallic[1, 2] and polymeric[3] nanofibers primarily by a method called *directed electrochemical nanowire assembly* (DENA), which will be described below. We have extended the DENA technique to grow metallic and polymeric nanofibers and nano-dendrites at the tips of electro-etched tungsten electrodes. These electrodes can be mounted on a movable 3D stage MicroManioulator) and can be positioned cleanly, near sites of interest. Furthermore, this

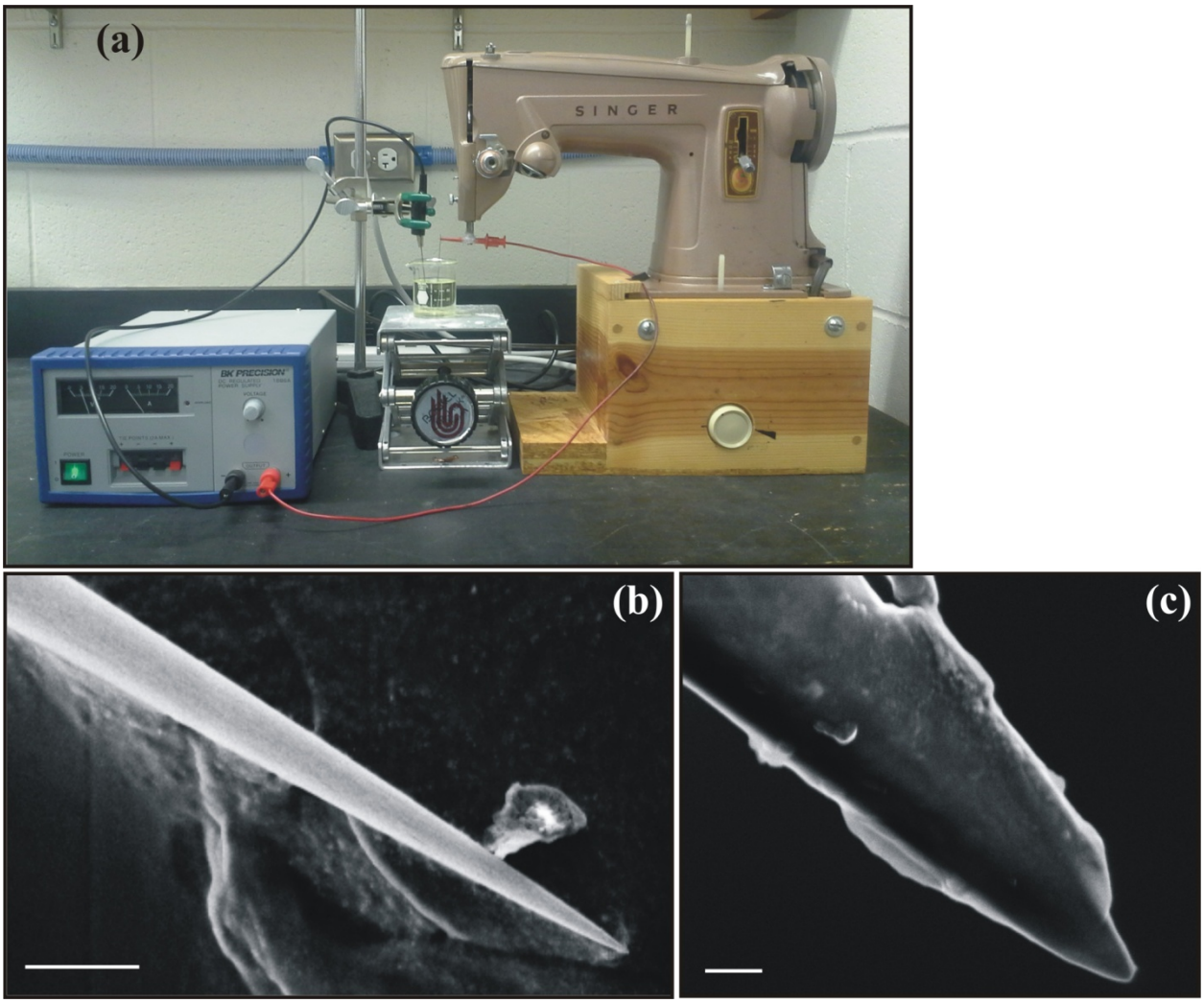

Figure 3.1. (a) Experimental set-up for tungsten wire etching. (b) SEM image of an elctro-etched tungsten electrode. Scale bar = 20 μm. (c) SEM image of an electro-eched, gold-coated tungaten electrode. Scale bar = 200 nm.

capability of fabricating movable fibers permits their calibration by the resonance vibration method (described below) and allows their use in various biological applications, such as cellular force sensing and nano-surgery.

Tungsten wire-etching was accomplished by a method described elsewhere. [4] The wire etching set-up is shown in Figure 3.1(a). A 0.13 mm diameter piece of tungsten wire (SmallParts) of ~5 cm length was electro-etched by mounting it vertically in the needle bar of a sewing machine. A 50 ml beaker containing 40.0 ml volume of aqueous 10 M $NaNO_2$ 6 M KOH solution was placed beneath the wire on a lab jack. A graphite counter electrode was placed in the solution. The tungsten wire was biased +4.0 V DC, while the graphite electrode was grounded. A DC power supply (BK Precision 1686A) was used to supply the voltage. The wire was then cycled in and out of the solution using the sewing machine at a constant rate for ~5 minutes. This procedure yields a fine conical tip with radii-of-curvature of 1 μm or less. Figure 3.1(b) shows Scanning Electron Micrograph (SEM) of a typical electro-etched tungsten filament. The radius of curvature of the tip of this filament is ~65 nm. The chemical mechanisms underlying the etching of tungsten wire in aqueous basic solution are as follows:[5]

$$\text{cathode}: \quad 6H_2O + 6e^- \rightarrow 3H_2(g) + 6OH^- \qquad (1a)$$

$$\text{anode}: \quad W(s) + 8OH^- \rightarrow WO_4^{2-} + 4H_2O + 6e^- \qquad (1b)$$

$$W(s) + 2OH^- + 4H_2O \rightarrow WO_4^{2-} + 3H_2(g) \qquad (1c)$$

The etching of tungsten wire takes place at the air-electrolyte interface, where *W* undergoes an oxidative dissolution to produce soluble WO_4^{2-} ions at the anode (equation 1(b)). The reaction also involves reduction of water; which produces the bubbles of H_2 gas and OH^- ions at the cathode (equation 1(a)).

The growth of DENA based PEDOT:PSS fibers requires gold electrodes. In order to prepare such electrodes, the etched tungsten electrodes are evaporatively coated with ~200 nm layers of chromium and gold respectively using a vacuum evaporator (Varian VE10). This is

done as follows: etched tungsten filaments are taped to two different glass slides at the rate of six filaments per slide. These glass slides are mounted on the sample holder of the vacuum evaporator. A ~ 4 mm sized chromium pallet (Cerac Inc) is loaded in the rear tungsten basket (coil), and ~ 1.5 cm long, 0.5 mm diameter piece of gold wire (Kurt J. Lesker) is loaded in the front tungsten basket of the vacuum evaporator. Before closing the chamber lid, the sample holder is positioned on top of the rear basket by rotating the manipulator knob. After evacuating the chamber, the tungsten filaments are first evaporatively coated with a layer of chromium. This is done by passing the current to the rear basket for 30.0 s. The sample holder is then moved so that it sits above the front basket. Finally, a gold layer is deposited on the tungsten filaments. This is done by passing current to the front basket until all of the gold evaporates (~30 s). Since the tungsten filaments are attached to the glass slide, only half of their surfaces get coated at a time. The remaining half-surfaces are coated by flipping over the filaments, and by repeating the procedure mentioned above. Figure 3.1(c) shows the SEM image of resulting (electro-etched gold coated) tungsten filament that has a sharp tip of ~50 nm radius of curvature.

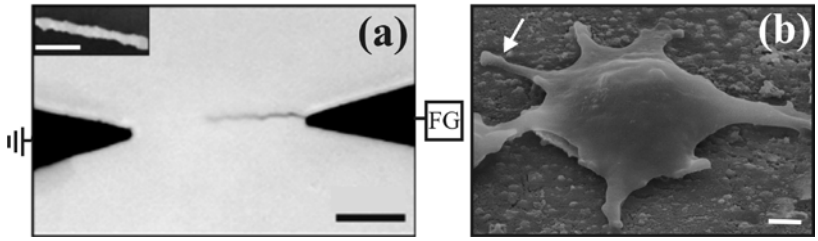

Figure 3.2. (a) Optical micrograph of PEDOT:PSS fiber grown at the tip of lithographic electrode by DENA technique. FG = function generator. Scale bar = 10 μm. Inset: SEM image of a PEDOT fiber. (b) SEM image of fixed D. discoideum cell with extending pseudopods. Scale bar = 1 μm.

3.2.2. DENA based PEDOT:PSS fiber growth

We have employed two different electrode configurations for the fabrication of PEDOT:PSS fibers. The first set-up [see Figure 3.2(a)] consists of PEDOT:PSS fibers fabricated at the tip of on-chip lithographic Au electrodes that are fixed to a glass substrate. Briefly, a 3 μl aliquot of aqueous solution containing 10.0 mM 3,4 ethylene dioxythiophene (EDOT) and 20.0 mM poly(sodium styrene sulfonate) was deposited across the ~30 μm gap between a pair of tapered lithographic electrodes. By applying a 3.5 V 20 kHz square wave voltage signal via a function generator across the electrodes, the PEDOT:PSS fiber was grown from the tip of the biased electrode towards the grounded electrode. The alternating voltage induces rapid electrochemical polymerization at the electrode tip. Polymerization at the sides of the electrode is much slower. As a result of this anisotropy in deposition-rates, a fiber grows outward from the tip. The voltage signal was terminated when the fiber reached the desired length. In order to remove the growth solution, an additional ~10 μl of de-ionized (DI) water was deposited in the gap between the electrodes; the resulting volume was then removed gently by wicking it away with a Kimwipe. This process was twice-repeated before depositing a ~10 μl volume of cell medium across the gap between the electrodes. The inset of Figure 3.2(a) shows the SEM image of a PEDOT:PSS fiber whose lengthwise-averaged width is 320 ± 30 nm, which is comparable to the width of a pseudopod as shown by an arrow in Figure 3.2(b), as desired. These fibers are rigidly bonded to the tip of the on-chip electrode but not to the glass substrate, and, hence, are cantilevered structures.

The second configuration [see Figure 3.3(a)] consists of PEDOT:PSS fibers fabricated at the tips of electro-etched gold coated tungsten filaments. After mounting the tungsten filament

in a 3D stage (MicroManipulator), a 20 μL aliquot of aqueous solution containing 10.0 mM 3,4-ethylene dioxythiophene and 20.0 mM poly(sodium styrene sulfonate) was deposited across the ~30 μm gap between the wire tip and an Au counter-electrode. The PEDOT:PSS fiber was grown from the tip of tungsten electrode towards the Au counter electrode by applying a ±3.5 V 10 kHz square wave voltage signal across these electrodes using a function generator (Agilent, 33220A). The voltage signal was terminated when the fiber reached the desired length. The fiber is removed from the growth solution by translating the microscope stage. This pulls the drop of aqueous solution away from the fiber. During this step, the surface tension at the air-filament-solution contact line slightly stretches the fiber lengthwise, straightening it as shown in Figure 3.3(b)-(e). After the fiber is completely pulled out of the solution, often the tip of the fiber is bent slightly [Figure 3.3(f)]. Therefore, as a final step, the bent part of the fiber is cut by short-circuiting between the fiber and the counter electrode by applying ~ 40 V alternating signal across them [Figure 3.3(g)-(h)]. The resulting straight fiber is shown in figure 3.3(i). Figure 3.3(j) shows a scanning electron microscopy (SEM) image of the resulting force sensor. The enlarged view in the inset shows its diameter to be ~500 nm, comparable to the dimension of pseudopod.

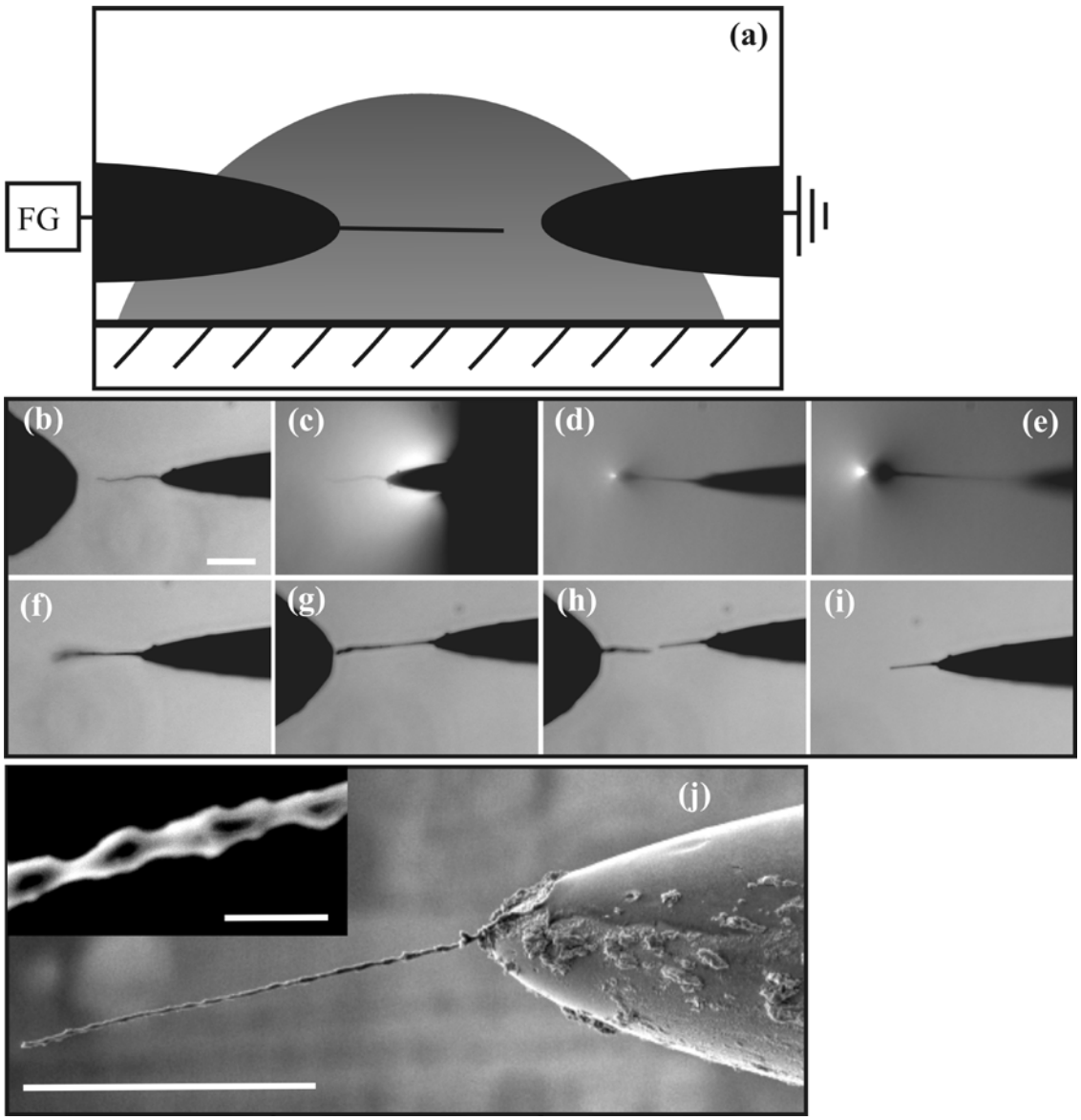

Figure 3.3. (a) Schematic depicting the side-view of the experimental setup for PEDOT:PSS fiber growth. FG designates a function generator. (b)-(i) The steps we employ for the fabrication of straight PEDOT:PSS fiber. (j) SEM image of a PEDOT:PSS fiber grown from an etched tungsten tip. Scale bar = 20 μm. Inset: enlarged view of the fiber. Scale bar = 1 μm.

Dendritic solidification[6-10] is an important mechanism underlying the DENA technique.[11, 12] Dendritic solidification occurs when the growth rate of a crystal or other solid is limited by the diffusion of the molecular building blocks through a *bulk* medium to the solidification front.[13, 14] Due to thermal fluctuations in the deposition rate, sharp protrusions are formed on the surface of the front. These protrusions perturb the concentration profile (of building blocks) in the solution creating the steepest gradients in front of the sharpest tips. The diffusive flux at the sharp tips is greater than that at neighboring depressions, so the growth rate of protrusions is enhanced. This effect is known as the Mullins-Sekerka instability[15] and, if not controlled, it would cause the runaway growth of randomly positioned sharp protrusions with reduced tip-radius. However, according to the Gibbs-Thomson effect[10], the rate of dissolution of a protrusion scales with the curvature of its tip. Hence, sharper tips tend to dissolve faster; that is, the Gibbs-Thomson effect tends to retard the growth rate and fatten the tip. The balance between the Mullins-Sekera instability and the Gibbs-Thompsons effect causes the steady growth of a dendrite with a fixed tip size.[16-18]

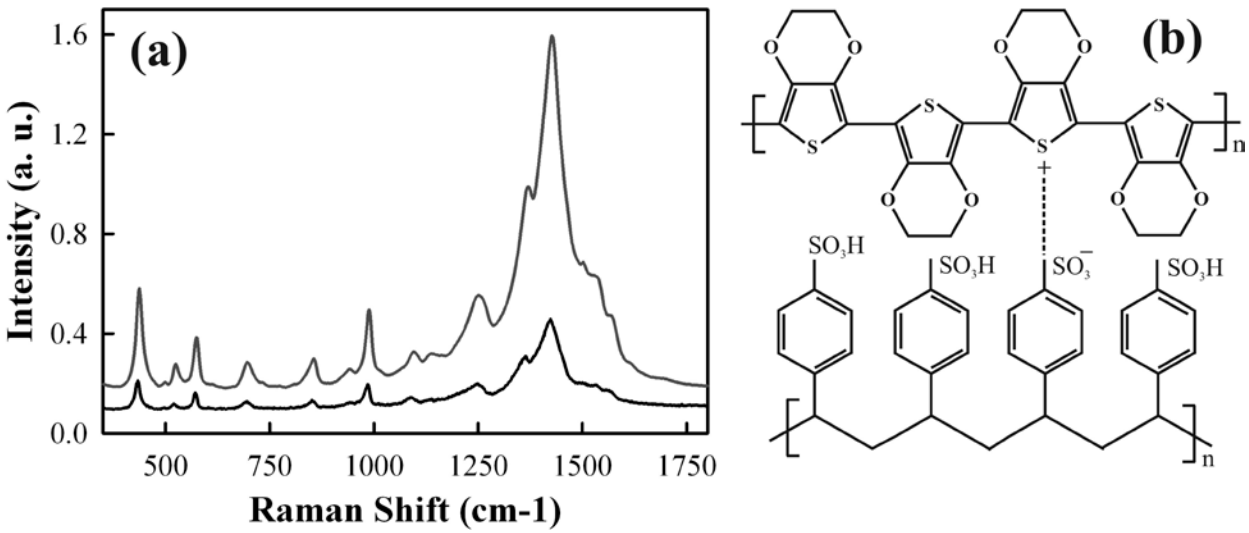

Figure 3.4. Raman spectrum of a PEDOT:PSS fiber (lower profile), and Raman spectra of PEDOT film (upper profile). (b) Chemical structure of PEDOT:PSS.

3.2.3. Raman spectral measurement for PEDOT:PSS fibers

The PEDOT:PSS composition of the fiber was confirmed by measuring the Raman spectrum of the fiber. For this, the fiber grown at the tip of tungsten filament was pulled out of the solution by translating the microscope stage away from the mounted fiber. The resulting dry fiber was mounted on the stage of a Raman microscope (iHR550 Horriba-Jobin Yvon spectrometer fiber coupled to a BX-41 Olympus upright microscope). The microscope was equipped with a 0.8 NA 50 × objective and a 633.2 nm *HeNe* laser (Melles Griot), providing a diffraction-limited laser spot size of ~400 nm. The Raman spectra were recorded using Labspec Application software. Figure 3.4 shows a Raman spectrum (lower profile) that was collected from a ~0.8 μm^2 area of a DENA-grown PEDOT:PSS fiber. For comparison, we have measured the Raman spectrum (upper profile) of a PEDOT:PSS film. The PEDOT:PSS film was prepared by electrochemical deposition of aqueous 20.0 mM PSS and 10.0 mM EDOT solution on a gold coated (prepared by use of a vacuum evaporator) glass slide by applying 1.8 V DC bias between the glass slide and a

Pt counter-electrode for ~5 min. The measured spectra are in agreement with each other and with previously reported spectra of PEDOT:PSS, [19] confirming that the fiber is made up of PEDOT:PSS. The features in the spectra are assigned as follows. The features at 1427 cm^{-1}, 1365 cm^{-1}, 1534 cm^{-1} correspond to the C=C symmetric stretching, C=C anti-symmetric stretching, and C-C stretching vibrational modes of PEDOT, respectively. The features at 1259 cm^{-1}, 1091 cm^{-1}, 701 cm^{-1}, 990 cm^{-1} and 576 cm^{-1} correspond to C-C inter-ring stretching, C-O-C deformation, C-S-C deformation, and oxyethylene ring deformation vibrational modes of PEDOT, respectively.[19] The chemical structure of PEDOT:PSS is shown in Figure 3.4(b).

3.3. Frequency dependent diameter

The application of nanowires as cellular force sensors requires that their stiffness be comparable to the stiffness of the cells. Cantilever rod theory predicts that the spring constant k for a cylindrical rod depends on its Young's modulus E, radius r, and length L as

$$k = \frac{3\pi r^4 E}{4L^3} \qquad (1)$$

The stiffness of PEDOT force sensors fabricated via DENA technique can be controlled by controlling their length or their diameter. The diameter of the fibers is controlled by controlling the frequency of the voltage signal.[11] Fibers grown at a lower frequency are thicker than those grown at a higher frequency. Figure 3.5 shows the radial distributions of PEDOT fibers grown at 20.0 kHz (blue), 10.0 kHz (red), and 5.0 kHz (green) respectively. The PEDOT fibers grown at 20.0 kHz have the mean radius of 0.14 ± 0.02 μm, and the PEDOT fibers grown at 10.0 kHz have the mean radius of 0.20 ± 0.023 μm, and those grown at 5.0 kHz have the mean radius of 0.32 ± 0.025 μm. The radii were determined by measuring length L and the fundamental resonance frequency ω_0 of the fiber. To measure ω_0, we position a single PEDOT

fiber ~10 μm away from an Au counter electrode. The fiber is resonated by applying ±20.0 V ac signal of frequency *f* and 20.0 V DC offset with respect to the Au counter electrode. Images of the vibrating fibers were collected as *f* is increased in 5.0 kHz steps. The frequency at which the amplitude reaches its first maximum locates the fundamental resonance frequency f_0, and angular frequency ω_0 is defined in terms of f_0 as $\omega_0 = 2\pi f_0$. The expression for ω_0 is given by beam theory:[20]

$$\omega_0 = 1.75\sqrt{E\rho_m^{-1}}rL^{-2} \tag{2}$$

where ρ_m is the mass density of the rod material. Solving (2) for *r* gives

$$r = \frac{1}{1.75}\sqrt{\rho_m E^{-1}}\omega_0 L^2 \tag{3}$$

Using equation (1), we can show that for a PEDOT fiber of fixed length, say, L = 20.0 μm, the spring constant *k* is found to be 0.23 nN/μm, 0.94 nN/μm, and 6.17 nN/μm, for r = 0.14 μm, 0.20 μm, and 0.32 μm respectively.

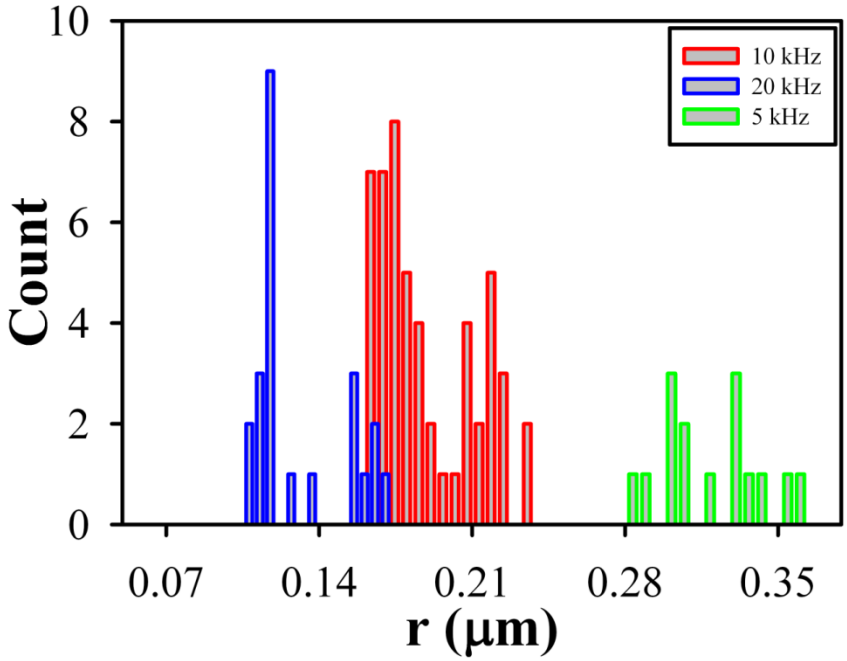

Figure 3.5. Radial distributions for PEDOT fibers grown at 20.0 kHz (blue bars), 10.0 kHz (red bars), and 5.0 kHz (green bars) frequency of the applied voltage signal.

3.4. Procedure for interfacing force sensors with *D. discoideum* cells

3.4.1. Dictyostelium Cell culture

In order to prevent contamination, all manipulation of *D. discoideum* cells is done in a sterile hood by the following technique. *D. discoideum* are grown in sterile petri dishes with ~ 10 ml of HL-5 medium, which provides the nutrients the cells need to grow. Live cells will adhere to the bottom of the dishes. Generally, dead cells are round and will not attach to the petri dish. The medium should be changed every 2-3 days by aspirating off the old medium and dead cells and then adding new medium. It is helpful to remove as many dead and alive cells as possible to allow for optimum growth. The transfer of old medium from petri dish to a flask is accomplished by the following procedure. A sterile Pasteur pipet attached to the pipet-aid (Drummond) is used to remove old medium and also to scrape live cells off the bottom of the

petri dish. The old medium and cells are disposed in a flask and ~ 2 ml of freshly prepared HL-5 medium is added to the petri dish. The cells are dislodged from the bottom of the petri dish by squirting the medium on to the bottom of the petri dish. This process is repeated until the cloudy looking coating is completely washed off of the petri dish surface. The cell-suspended medium is again disposed in the flask with the help of pipet and ~10 ml of freshly prepared HL-5 medium is added to the dish. When finished, ~1 ml of bleach solution is added to the flask to kill the disposed cells. New stocks of cells should be raised from frozen spores approximately every 2 months.

3.4.2. Preparation of HL-5 (oxoid peptone) medium

HL-5 medium provides nutrients for the cells and is used as cell culturing medium. The HL-5 medium is prepared in 1 liter orange-capped bottle. To make 1.0 liter of solution, 15.0 g "Oxoid" bacteriological peptone L37, 7.0 g Yeast extract, 0.6 g $Na_2HPO_4(7H_20)$, and 0.4 g KH_2PO_4 are added to 1.0 liter of 18.0 MΩ deionized water. After preparing the solution, it is stirred by gently shaking the bottle for ~2 minutes. After 30 minutes, the solution is autoclaved for 1 hour (remember to add water to the bottom of Autoclave tray) at 120 ^oC, allowed it to cool for 24 hours, and then autoclaved again for 1 hour at 120 ^oC. The stock solution is cooled for another 24 hours before use. Just before use, 800 μl of 50% glucose solution and 400 μl of Antibiotic/antimycotic (6.0 ml) solution is added per 40.0 ml HL-5 medium.

3.4.3. Preparation of 50% Glucose solution

Prior to cell culture, the glucose solution is mixed in HL-5 culturing medium at the ratio of 800.0 µl of 50 % glucose solution per 40.0 ml of HL-5 medium. In order to prepare this solution, 100.0 g dextrose is gradually added to about 130.0 ml of 18.0 MΩ deionized water while stirring (stir bar in flask) in orange-capped bottle. More 18.0 MΩ deionized water is added to make 200.0 ml of solution. One may need to heat solution to dissolve dextrose (do not let solution to boil). The solution is autoclaved for 30 minutes at 120 ^{o}C (remember to add water to the bottom of Autoclave tray).

3.4.4. Preparation of Na^{+}/K^{+} Phosphate Buffer solution

10× (120.0 mM) Na^{+}/K^{+} phosphate buffer solution is used to make Agar plates. The detailed protocol and uses of Agar plates is described below. To prepare 10× phosphate buffer solutions, 16.6 g NaH_2PO_4 is added to 1.0 liter of ultrapure water in orange capped bottle. The pH of the solution should be adjusted to 6.1 with 1.0 M KOH. The solution is autoclaved for 30 min at 120 ^{0}C (remember to add water to the bottom of Autoclave tray).

D. discoideum cells show rapid migration when they are starved for 4-6 hours. So, prior to each cellular force experiments, *D. discoideum* cells needs to be starved. This is done by transferring the cells from its food medium (HL-5 culturing medium) to 1× (12.0 mM) phosphate buffer solution. The detailed protocol for this process is described below. To prepare 1× phosphate buffer solution, 100.0 ml of 10× solution is added in 900.0 ml of 18.0 MΩ deionized water. The solution is then autoclaved for 30 min at 120 ^{0}C.

3.4.5. Preparation of Agar plates

Agar plates are used to grow *D. discoideum* spores. The agar solution is prepared by mixing 100.0 ml of 10× stock solution of Na^+/K^+ phosphate buffer and 15.0 g Agar in 900.0 ml of 18.0 MΩ deionized water in an orange capped bottle. A stir bar is added to the flask and the mixture is stirred briefly. The mixture is then autoclaved for 30 minutes. After cooling down to ~70 ^{0}C, the mixture is poured into petri dishes. When cooled down to room temperature, the mixture forms a gel (agar) on bottom surface of the petri dishes. The rest of the mixture is stored in a refrigerator for future use; it can be reused by melting the mixture using the microwave.

3.4.6. Storage of Dictyostelium spores at -70 ^{0}C

D. Discoideum spores are grown on agar plates (prepared on petri dishes). This is done by pouring 1000.0 μl of HL-5 medium containing cell suspension into an agar plate. The cells aggregate to form slugs and then fruiting bodies with spores over the next two days. For storage of the spores, they are first transferred to a petri dish lid by slamming the dish (inverted) onto the bench top. The spores are then suspended in 1-2 ml of sterilized Freezer Spore Storage Buffer (FSSB) Solution (10.0 mM NaCl, 10.0 mM KCl, 2.7 mM $CaCl_2$, and 15% Glycerol) and transfered to freezer tube (cryogenic vial or eppi tube). The tube is stored in a refrigerator at -70 ^{0}C. In order to re-inoculate, a sterilized toothpick is used to scrape an amount of frozen spores into a sterile petri dish and then covered with ~10 ml of HL-5 medium. The remaining frozen spores are returned to the freezer for future use.

3.4.7. Removal of D. Discoideum cells from HL-5 medium for cellular force experiment

Prior to each cellular force experiment, *D. discoideum* cells, grown at 24 ^{o}C, were removed from HL-5 culturing medium by drawing 1000 μL of the cell-medium suspension from a Petri dish and centrifuging the aliquot for ~10 s at 1.34×10^3 g. In order to get rid of all traces of the HL-5 medium, the supernatant was discarded and the cells were washed with 1.5 ml of 12.0 mM phosphate buffer, shaken, and centrifuged twice before suspending the cells a final time in phosphate buffer. These cells were starved for 4-6 hours. 50 μL volumes of cell suspension and phosphate buffer were deposited in the side-view imaging chamber described below. A waiting time of ~20 minutes, following cell deposition, was required for the cells to settle and begin migrating on the surfaces of the chamber.

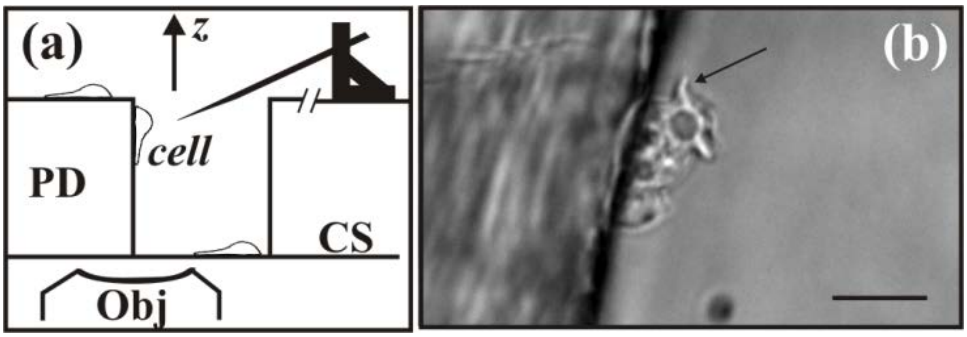

Figure 3.6. (a) Schematic of cell side-view imaging setup depicting the Petri dish (PD), coverslip (CS), and microscope objective (obj). (b) Side-view micrograph of a D. discoideum cell extending apical pseudopods. Scale bar = 10 μm.

3.4.8. Cell side-view imaging

To facilitate investigation of apical adhesive contacts, which are important for amoeboid migration through 3D matrices, cells were visualized *in profile* so that the size, shape and cellular location of the cell-fiber contact could be clearly observed. This mode requires that the imaging plane of the microscope be perpendicular to the substrate on which the cells crawl. Our set-up for realizing this perspective, which differs from that reported elsewhere,[21] is diagrammed in Figure 3.6(a). Briefly, a hole was bored in the base of a Petri dish (Fisherbrand) using a 7/32" drill bit at 990 rpm; these parameters minimized lip and sidewall roughness (~3 μm). A cover-slip was cemented to the underside of the dish to seal the hole. *D. discoideum* cells were cultured and introduced to the chamber at cell surface densities of ~10^3 mm^{-2}. The dish was mounted on the stage of an inverted microscope (Leica IRB) for optical imaging, primarily with a 63× water immersion objective of 0.90 numerical aperture. Side-view imaging of the cells was accomplished by focusing the microscope on those migrating on the sidewalls of the hole. A typical side-view image of a *D. discoideum* cell is shown in Figure 3.6(b). The arrow points to an apical pseudopod.

3.5. DENA based metallic wire growth

Over the past decades, our group has developed the directed electrochemical nanowire assembly (DENA) method for fabricating metallic nanowires and nano-dendrites composed of different types of metal at the tips of other electrodes. This process is performed in aqueous metallic salt solutions.[2, 11] The parameters that control the wire growth are the metallic salt concentration, frequency and voltage of the square wave signal and the inter-electrode gap. By controlling

these wire growth parameters, we are able to fabricate either single needle-shaped wires or highly branched dendrites with sizes ranging from 20 nm up to ~1 μm.

3.5.1. Gold wire growth

Figure 3.7(a) depicts the set-up for controlling the growth of metallic nanowires and nanodendrites via the DENA technique. The set-up consists of an electrode pair immersed in simple *metallic salt* solution. The counter-electrode (CE) is composed of gold wire (Kurt J. Lesker, 0.5 mm diameter). The working electrode (WE), which has a sharper tip, is composed of a piece of tungsten wire, the tip of which is electro-etched to a ~1 μm radius-of-curvature.[4, 22] The etched tungsten electrode is mounted in a 3D stage and positioned ~1 μm above a microscope slide that is mounted on an inverted microscope (Leica, IRB). The inter-electrode spacing is adjusted to ~ 30 μm. For the fabrication of gold nanowire, a 20 μl aliquot of solution

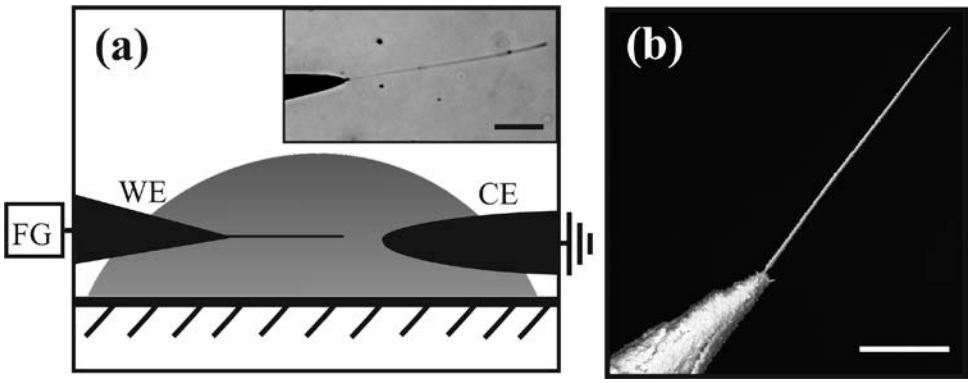

Figure 3.7. (a) Schematic depicting the side-view of the experimental set-up for the growth of metallic nanowires via DENA technique. FG designates a function generator. Inset: optical image of an Indium wire. Scale bar = 25 μm. (b) SEM image of a gold nanowire grown at the tip of etched tungsten electrode. Scale bar = 10 μm.

composed of de-ionized (18 MΩ) water and 20.0 mM $HAuCl_4$ (Sigma Aldrich) is deposited across the inter-electrode gap. A function generator (Hewlett Packard, 8116A) is used to apply a square wave voltage signal (± 4.0 V, 20.0 MHz) to the working electrode while grounding the counter-electrode and, thereby induce growth of the gold nanowire at the sharper working electrode. Growth occurs within a range of frequencies, from 10.0 MHz to 50.0 MHz. Figure 3.7 (b) shows the SEM image of a typical gold nanowire that was grown at 20.0 MHz. We have shown elsewhere that the electron diffraction patterns collected from such nanowires quantitatively match the known diffraction patterns of bulk gold, indicating that these nanowires are composed of gold.[1]

3.5.2. Indium wire growth

For the fabrication of indium nanowires, a 20 μl aliquot of solution composed of de-ionized (18 MΩ) water and 55.0 mM $In(CH_3OO)_3$ (Aldrich) is deposited across the inter-electrode gap [Figure 3.7(a)]. A function generator (Hewlett Packard, 8116A) and alternating voltage amplifier (FLC electronics, F10A) are used to create a square wave voltage signal of ± 49.0 V, 3.0 MHz that is then applied to the working electrode while grounding the counter- electrode. This signal induces growth of the indium wire at the sharper working electrode. The inset of Figure 3.7(a) shows an optical micrograph of a typical indium wire that was grown by this process. We have shown elsewhere that the diameters of an individual indium wires grown by this process are found to be as small as 114 nm.[11] The electron diffraction patterns collected from such wires indicate that they are single crystalline in nature.[2]

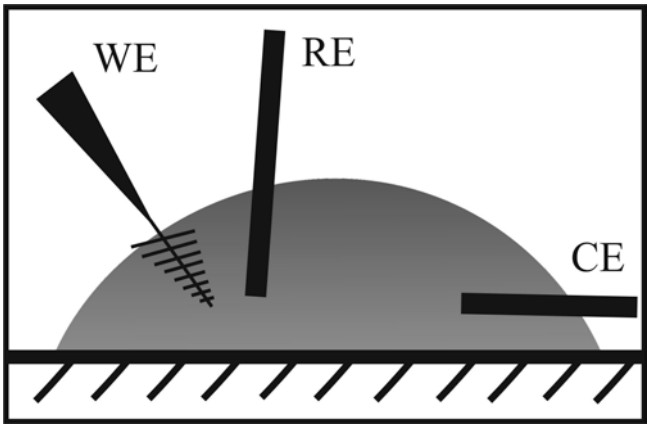

Figure 3.8. Schematic depicting the 3-electrode setup used to measure cyclic voltammograms of gold dendrites. WE, RE, and CE designates the working electrode, reference electrode, and counter electrode, respectively.

3.6.1. Cyclic voltammetry of gold dendrite

Cyclic voltammetry is an electrochemical technique for studying electroactive species in solution. Essentially, a cyclic voltammagram is a current-voltage profile of a chemical solution, analogous to the current-voltage profiles that are used to characterize electronic components. Figure 3.8 is a schematic depicting the 3-electrode arrangement that we employed to measure cyclic voltammagrams of individual gold dendrites and also of bulk gold samples. To measure a cyclic voltammagram, the potential is advanced in cyclic manner. Due to the electroactive nature of the components of the solution, the solution resistance will vary in time under a given potential. Therefore, to hold the potential fixed during each step, the cyclic voltammetric measurements are done using three electrodes. After growing a dendrite from the tip of the working electrode, the $HAuCl_4$ solution was gently withdrawn and replaced with 0.1 M *KCl*. The working electrode was pulled out of the solution via a translational stage until only the dendrite remained in the solution; hence, the dendrite alone served as the working electrode. This arrangement ensures that only the electrochemistry of the gold dendrite and not that of the

tungsten electrode will contribute to the cyclic voltammagram. Care must be taken that the air-water surface tension does not separate the dendrite from its substrate. The reference electrode consists of Ag/AgCl and is prepared by dipping a piece of Ag wire (0.5 mm in diameter, Alfa Aesar) in 4.0 M KCl solution for 1 hour. The counter electrode consists of a Pt wire (0.5 mm in diameter, Kurt J. Lesker).

The circuit design of a homebuilt potentiostat[23] is shown in Figure 3.9. The circuit was built on a breadboard using LM148J quadruple operational amplifier (Digi-Key). The input voltage e_{in} is supplied to the current buffer operational amplifier A and to the reference electrode RE. In a current buffer amplifier the output is isolated from the input, so the current at its output is not limited by the input current. This feature is important for the counter electrode CE, which needs to able to provide any current required by the electrochemical activity at the working electrode WE. The reference electrode RE is connected to the input of operational amplifier B. The input impedance of operational amplifier B is essentially infinite, hence no current flow through its input (i.e. through RE). The operational amplifier C is a current-to-voltage convertor, so the electrochemical current generated at the working electrode W is converted into equivalent voltage by operational amplifier C. The input voltage was supplied via a Source meter (Keithley 2400), and the output voltage was measured by a nano-voltmeter (Keithley 2182A). The Source meter and nano-voltmeter were controlled by Labview software.

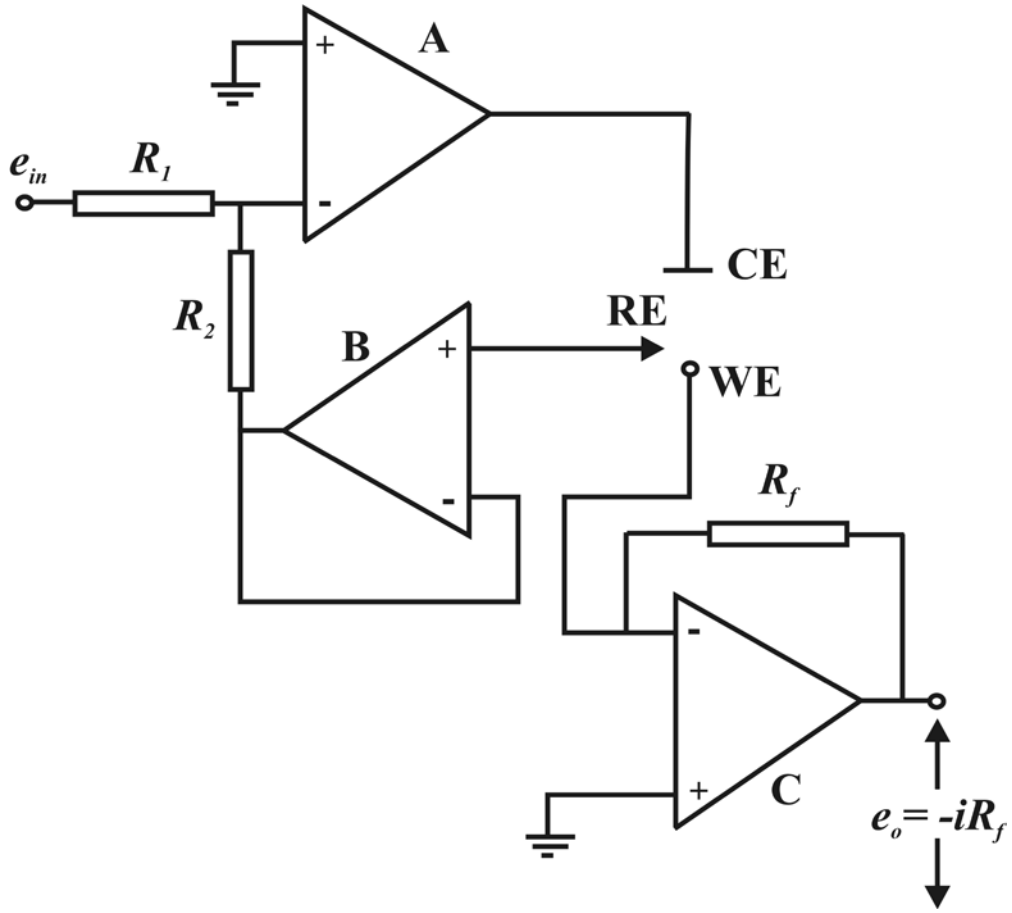

Figure 3.9. Circuit diagram for a potentiostat.

In a typical cyclic scan, the Labview software records the values of input and output voltages. These data are copied in the SigmaPlot worksheet. The cross-cell current i that flows in the working electrode is obtained by dividing the output voltage e_o by R_f. Finally, i vs ΔV plot is obtained via SigmaPlot software. In plotting the current, we use the IUPAC convention that a positive (negative) current corresponds to negative (positive) charge flowing into (out of) the working electrode. The plot of i versus ΔV constitutes a cyclic voltammagram (CV). A typical CV of gold dendrites is shown in Figure 3.10.

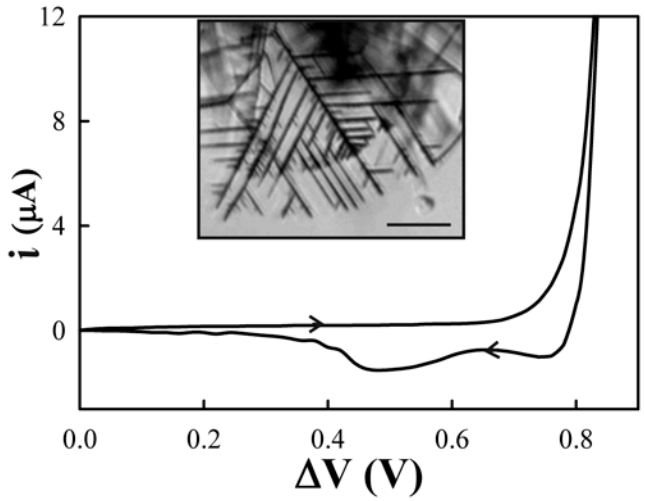

Figure 3.10. Cyclic voltammagrams of obtained in 0.1 M KCl with a dendritic gold working electrode. Scan rate = 25 mV s^{-1}. Inset: optical image of a gold dendrite.

3.7. References

1. B. Ozturk, T. Mishima, D. R. Grischkowsky and B. N. Flanders, *Nanotechnology*, 2007, **18**, 175707.
2. I. Talukdar, B. Ozturk, T. D. Mishima and B. N. Flanders, *Appl. Phys. Lett.*, 2006, **88**, 221907.
3. P. S. Thapa, D. J. Yu, J. P. Wicksted, J. A. Hadwiger, J. N. Barisci, R. Baughman and B. N. Flanders, *Appl. Phys. Lett.*, 2009, **94**, 033104.
4. Y. Qiao, J. Chen, X. Guo, D.cantrell, R. Ruoff and J. Troy, *Nanotechnology*, 2005, **16**, 1598-1602.
5. J. P. Ibe, P. P. Bey, S. L. Brandow, R. A. Brizzolara, N. A. Burnham, D. P. DiLella, K. P. Lee, C. R. K. Marrian and R. J. Colton, *Journal of Vacuum Science & Technology A*, 1990, **8**, 3570-3575.
6. G. E. Nash and M. E. Glicksman, *Acta Metall.*, 1974, **22**, 1291.
7. S. C. Huang and M. E. Glicksman, *Acta Metall.*, 1981, **29**, 701-715.
8. S. C. Huang and M. E. Glicksman, *Acta Metall.*, 1981, **29**, 717-734.
9. J. S. Langer, *Rev. Mod. Phys.*, 1980, **52**, 1-28.
10. D. A. Kessler, J. Koplik and H. Levine, *Adv. Phys.*, 1988, **37**, 255-339.
11. B. Ozturk, I. Talukdar and B. N. Flanders, *Nanotechnology*, 2007, **18**, 365302.
12. P. S. Thapa, B. J. Ackerson, D. R. Grischkowsky and B. N. Flanders, *Nanotechnology*, 2009, **20**, 235307.
13. G. P. Ivantsov, *Dokl. Akad. Nauk USSR*, 1947, **58**, 567.
14. Y. Saito, *Statistical Physics of Crystal Growth*, World Scientific, River Edge, 1996.
15. W. W. Mullins and R. F. Sekerka, *J. Appl. Phys.*, 1964, **35**, 444-451.
16. J. S. Langer and H. Müller-Krumbhaar, *Acta Metallurgica*, 1978, **26**, 1681-1687.
17. J. S. Langer and H. Müller-Krumbhaar, *Acta Metallurgica*, 1978, **26**, 1689-1695.

18. J. S. Langer and H. Müller-Krumbhaar, *Acta Metallurgica*, 1978, **26**, 1697-1708.
19. M. Stavytska-Barba and A. M. Kelley, *The Journal of Physical Chemistry C*, 2010, **114**, 6822-6830.
20. L. Meirovitch, *Elements of Vibration Analysis*, Mc Graw-Hill Book Company, New York, 1986.
21. O. Chaudhuri, S. Parekh, W. Lam and D. Fletcher, *Nature Methods*, 2009, **6**, 383-387.
22. G. Paneru, P. S. Thapa, S. P. Mcbride, A. Ramm, B. M. Law and B. N. Flanders, *Nanotechnology*, 2012, **23**, 455105.
23. A. J. Bard and L. R. Faulkner, *Electrochemical Methods: Fundamentals and Applications*, John Wiley & Sons, New York, 1980.

Chapter 4 - Forces at individual pseudopod-filament adhesive contacts

(Published in *Applied Physics Letters*, 2011, **99**, 093702. The original manuscript is presented in Appendix A.)

Abstract

On-chip cellular force sensors are fabricated from cantilever poly(3,4-ethylene dioxythiophene) filaments that visibly deflect under forces exerted at individual pseudopod-filament adhesive contacts. The shape of the deflected filaments and their ~ 3 nN/μm spring constants are predicted by cantilever rod theory. Pulling forces exerted by *D. discoideum* cells at these contacts are observed to reach ~20 nN without breaking the contact.

4.1 Introduction

The forces that cells exert on substrates at adhesive contacts are critical to basic processes such as migration and cell division. Pseudopods are exploratory appendages that crawling cells like *D. discoideum*, leukocytes,[1] and breast cancer cells[2] extend to probe the anterior substrate surface. Adhesive contact between the tips of the pseudopods and the substrate occurs frequently. These are the first contacts that the cell makes with the anterior substrate region. In addition to force-application, environmental sensing occurs at these contact sites, influencing whether the cell alters or persists in its direction-of-migration.[3] Despite the importance of pseudopod-substrate adhesive contacts in force transmission and environmental sensing, there has been little characterization of pseudopod-substrate adhesion at the single contact-level.

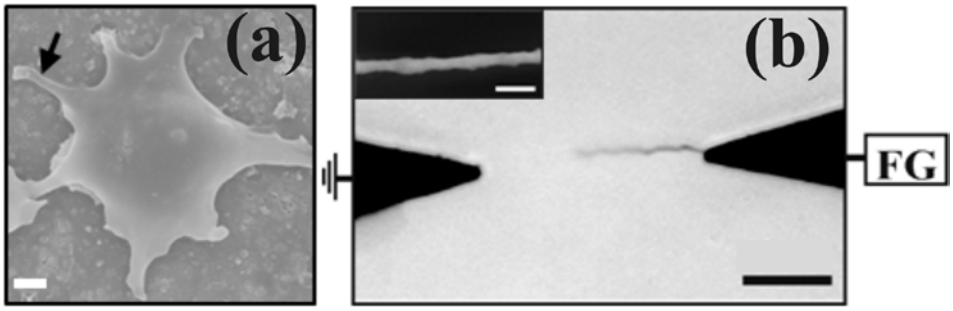

Figure 4.1. (a) Scanning electron micrograph of fixed *D. discoideum* cell with extending pseudopods. Scale bar = 1 μm. (b) Optical micrograph of PEDOT filament grown by the DENA technique. FG ≡ function generator. Scale bar = 10 μm. Inset: a scanning electron micrograph of a filament. Scale bar = 1 μm.

The most widely used technique for characterizing cellular forces is the deformable substrate method where cell-induced wrinkling or marker-displacement of the elastic substrate is observed.[4] A key advantage of this approach is that the substrate displacements occur in the imaging plane of the optical microscope, permitting direct visualization of the process. However, the forces at the discrete adhesive contact sites are not directly measured but are instead extracted by a non-trivial modeling effort that correlates the measured substrate displacement-field with the inferred force field and with the discrete sites.[5] Off-substrate forces may be directly measured with an atomic force microscope (AFM) with exquisite precision;[6] however, visualization during such measurements, which are usually made in a plane normal to the optical imaging plane, can be a challenge. Methodology for the simultaneous visualization and direct characterization of forces exerted by individual pseudopodia is needed.

4.2. Experimental methods

To this end, we have fabricated on-chip cantilever poly(3,4-ethylene dioxythiophene) (PEDOT) filaments that visibly deflect under forces exerted at individual pseudopod-filament contacts. PEDOT was chosen for its biocompatibility.[7] A typical 3.2 μm long, ~400 nm wide pseudopod is indicated by the arrow in Figure 4.1(a). Direct characterization of an individual pseudopod requires a probe of comparable dimension. To produce such filaments, the simple polymerization technique *directed electrochemical nanowire assembly* (DENA) was employed.[8] Briefly, a 3 μL aliquot of aqueous solution containing 0.01 M 3,4-ethylene dioxythiophene and 0.02 M poly(sodium styrene sulfonate) was deposited across the ~30 μm gap between a pair of tapered, lithographic Au electrodes. The filament in Figure 4.1(b) was produced by applying a ±3.5 V 20 kHz square wave voltage signal across the electrodes to induce filament growth from the right electrode at a rate of ~5 μm/s. The voltage signal was terminated when the filament reached the desired length of ~14 μm. The scanning electron microscopy (SEM) based image in the inset shows its lengthwise-averaged width to be 320 ± 30 nm. Comparison to Figure 4.1(a) shows filament and pseudopod widths to be comparable, as desired. These filaments are rigidly bonded to the on-chip electrode but not to the glass substrate and, hence, are cantilever structures.

Type KAx3 *D. discoideum* cells were grown at 24 ^{o}C in Petri dishes containing HL-5 culturing medium.[9] Prior to transfer to the chips, 1000 μL of the cell-medium suspension was centrifuged for ~10 s at 1.34×10^3 g. The HL-5 supernatant was replaced with 1000 μl of 12 mM phosphate buffer, followed by gentle shaking for 1 minute. This process was twice-repeated before suspending the cells in 300 μL of phosphate buffer and starving them for 4-6 hours. To

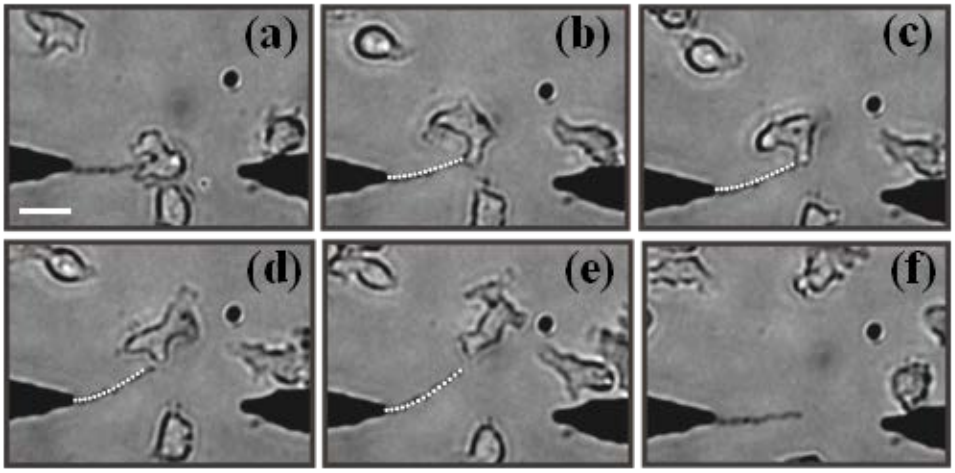

Figure 4.2. Series of optical micrographs of a cantilever PEDOT filament (a) in its neutral position 7 s after contact initiation by the pseudopod. Scale bar = 10 μm; (b)-(e) while being deflected upwards by the cell at times 37 s, 46 s, and 54 s, respectively; and (f) at time 105 s when the filament is back in its neutral position after release by the cell (enhanced online, where a video of this event is shown at 3 × the actual rate). The white dotted curves on panels (b)-(e) represent the deflected filament shapes predicted by cantilever rod theory.

prevent evaporation of the cell medium, a 60 μL hybridization chamber (Grace Biolabs) was adhered to the filament-laden chip. Before sealing with a transparent lid, 10 μL volumes of cell suspension and phosphate buffer were deposited in the chamber. Typical cell surface densities were ~10^3 mm^{-2}. A waiting time of ~20 minutes following cell deposition was required for the cells to settle, to begin migrating, and for a single cell to randomly contact the filament.

4.3 Results and discussion

Figures 4.2(a)-(f) constitute a series of bright-field images (collected on a microscope of 0.75 numerical aperture) of four *D. discoideum* cells migrating randomly on a glass slide. One of

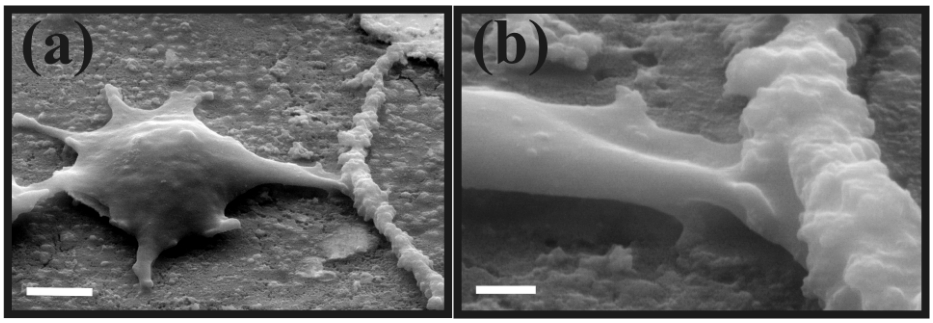

Figure 4.3. (a) Scanning electron micrograph of fixed cell with a pseudopod in direct contact with PEDOT filament. Scale bar = 2 μm. (b) Enlarged view of contact region. Scale bar = 500 nm.

these cells contacts the cantilever filament in Figure 4.2(a). This cell deflects the filament by exerting pulling force on it in Figures 4.2(b)-(e), and releases it in Figure 4.2(f). The shape of the pseudopod evolves throughout this event. We have observed ~10^2 such events. Clearly, these filaments are flexible enough to deflect visibly upon contact by a foraging cell (yet stiff enough to resist visible thermal motion). In the small deflection approximation, the shape of a cantilever rod of length L and radius r that is bent by a force F_A applied to its free end is described by[10]

$$\delta_F(x) = \frac{F_A}{6EI} x^2 (3L - x) \qquad (1)$$

where $I = \pi r^4/4$ is the area moment of inertia of the solid cylindrical rod, E is Young's modulus of the rod-material, and x denotes position along the rod length with respect to the fixed end. This function was fitted to the deflected filament profiles in panels (b)-(e), as designated by the white dashed curves overlaid upon these micrographs. As discussed below, no adjustable parameters were used in achieving these fits.

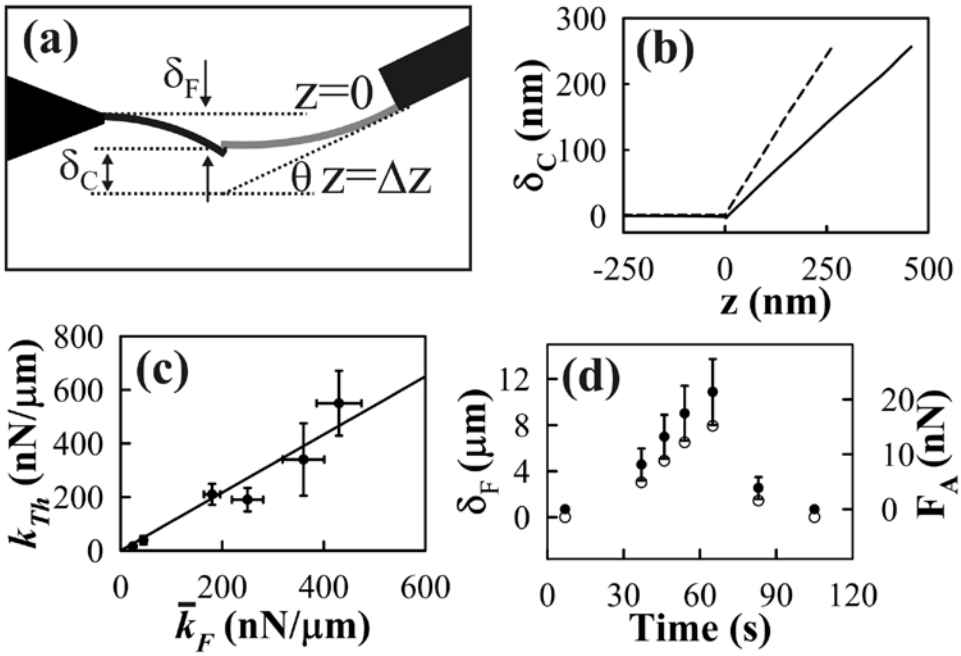

Figure 4.4. (a) Schematic of AFM-based determination of the filament spring constant. The gray curve denotes the AFM cantilever, while the black curve denotes the filament. (b) AFM cantilever deflection magnitude δ_C versus vertical position of AFM head z for pressure against a rigid surface (dashed profile) and a PEDOT filament (solid profile). (c) Plot of the theoretical spring constants of PEDOT filaments versus their measured spring constants. The solid line is the best linear fit to the points. (d) Cell enforced deflection (unfilled circles) and force (filled circles) measured during the event depicted in Figure 2.

Figure 4.3(a) shows a scanning electron micrograph of a *D. discoideum* cell that was fixed shortly (5 s) after establishing pseudopod-filament contact.[11] An enlarged view of the contact region is shown in Figure 4.3(b). The surface of the pseudopod-tip is butted against the left side of the filament. The pseudopod does not encompass the filament. The two other pseudopod-filament contacts that were characterized also exhibited butt-joint contact-structure. Deflection by a *pulling*-force (as illustrated in Figures 4.2(b)-(e)) that is applied at a simple butt-joint implies *adhesive* contact between the joined pseudopod and filament surfaces. As with better characterized adhesive contacts like focal adhesions[12] and actin foci,[13] adhesion is likely

due to numerous transmembrane cellular adhesion molecules (of undetermined type) that bind the substrate surface.

Knowledge of the radius, Young's modulus, and length of a solid, cylindrical cantilever rod permits calculation of its theoretical spring constant in the small deflection approximation: $k_{Th} = 3EI/L^3$.[10] To assess how well this simple equation predicts the spring constants of PEDOT filaments, we have used an AFM to directly measure the k_F values of several filaments and compared these values to the corresponding k_{Th} values. The AFM (MFP-3D, Asylum Research) was calibrated by pressing its cantilever (NP-0, Veeco) against a hard glass surface to quantify the cantilever deflection-photodiode voltage relationship. The spring constant k_C of this cantilever was determined by the thermal method.[14] Hooke's law then gives the magnitude of the elastic force exerted by the cantilever F_C for deflection δ_C: $F_C = k_C\delta_C$. To measure the spring constant of a PEDOT filament k_F, the AFM cantilever was pressed against an individual filament by lowering the AFM head by distance Δz, as depicted in Figure 4.4(a).[15] This measurement deflects the filament by distance δ_F and yields a δ_C vs Δz profile (solid line in Figure 4.4(b)). The opposing forces exerted by the filament F_F and cantilever F_C are equal in magnitude (Newton's 3rd Law); hence, $k_F\delta_F = k_C\delta_C$, where δ_F is the (unknown) filament displacement and $F_F = k_F\delta_F$. Δz is related to δ_C and δ_F by $\Delta z = \delta_C + \delta_F$, giving $k_F = k_C\left(\Delta z/\delta_C - 1\right)^{-1}$. The effects of AFM cantilever tilt by angle θ (11^o for all cases in this study) and off-end loading of the filament are accounted for by corrective factors, yielding[16]

$$k_F = k_C\left(\Delta z/\delta_C - 1\right)^{-1}\left(\frac{L-\Delta L}{L}\right)^3 \cos^{-2}\theta. \qquad (2)$$

Table 4.1: Measured properties of six PEDOT filaments and their associated spring constants (in units of nN/μm).

r (μm)	L (μm)	ΔL (μm)	$\delta_C/\Delta z$	k_c	k_{Th}	k_F	$\overline{k_F}$
0.72±0.08	13.24	1.3	0.59	450	550	490	430
0.64±0.06	15.55	2.2	0.49	270	210	170	180
0.52±0.06	12.18	1.8	0.77	110	190	240	250
0.61±0.12	12.38	0.5	0.57	310	340	380	360
0.28±0.06	12.04	2.2	0.42	58	16	20	24
0.29±0.06	9.50	0.5	0.90	55	39	40	45

ΔL is the distance from the filament tip to the loading point as measured via an internal optical microscope in the AFM. The spring constants of six different PEDOT filaments k_F were obtained by substituting into Eqn. (2) the corresponding k_C, L, ΔL, and $\delta_C/\Delta z$ values given in Table 4.1. Each filament was characterized three times with each of three different cantilevers whose spring constants varied significantly. The averages of these nine determinations for each of the six filaments are reported in column $\overline{k_F}$.

To calculate the k_{Th} values, we approximate the PEDOT filament shapes as cylinders having radii equal to the lengthwise averaged radii of the filaments. These SEM determined values are reported with their standard deviations in Table 1. Also, we have taken E = 2.0 GPa, the average of two recent determinations (1.8 GPa[17] and 2.26 GPa[18]) of the PEDOT Young's modulus. Figure 4.4(c) plots k_{Th} vs $\overline{k_F}$. The horizontal error bars denote the standard error

associated with the $\bar{k}_F$ determinations; the vertical error bars result from propagation of radial standard deviations and ±0.03 μm length non-uniformities in the k_{Th} calculations. The solid line, the best-fit to these points (constrained to pass through the origin), has a near-unity slope of 1.08. Hence, the correlation between k_{Th} and $\bar{k}_F$ is strong, indicating that cantilever rod theory provides reasonable predictions of the filament spring constants. While it lies beyond the scope of this letter to do so here, the PEDOT filaments have lengthwise radial variations of 10-20 %, so the success of $k_{Th} = 3EI/L^3$ deserves further examination.

Figure 4.4(d) shows the filament deflection-values (unfilled circles) corresponding to frames 4.2(a)-(f) (except for the point at 83 s whose image is not shown in Figure 4.2). SEM analysis of this filament revealed a 220 nm lengthwise averaged radius and 16.0 μm length. Hence, as demonstrated above, cantilever rod theory ($k_F = 3EI/L^3$) indicates a spring constant k_F of 2.7 ± 0.7 nN/μm; the sizable uncertainty is expected given the highly nonlinear functionality of k_F. Conversion of these δ_F-values to F_A-values via Hooke's law ($F_A = \delta_F k_F$) yields the filled circles in Figure 4.4(d). (The error bars reflect the propagated uncertainties of δ_F and k_F). As these data and Figure 4.2(e) show, F_A reaches 21 nN without breaking contact. The measured force values of 8, 13, 18, and 21 nN reported in Figure 4.4(d) (along with $I = 1.8 \times 10^{-27}$ m^4 and E = 2.0 GPa) were used to calculate the parameters $F_A/6EI$ in Eqn. (1) to fully determine the shape functions (white dotted lines) shown in Figures 3.2(b)-(e), respectively. The close agreement with the measured shapes confirms the usefulness of cantilever rod theory for predicting the elastic properties of these PEDOT filaments. In future studies, we will employ this methodology for the simultaneous visualization and measurement of forces exerted at single pseudopod-filament contacts to articulate the factors that dictate adhesion strength and duration.

4.4 Acknowledgements

This work was partially supported by National Science Foundation grants PHY-0646966 (BNF) and DMR-0603144 (BML).

4.5 References

1. P. Friedl, S. Borgmann and E. B. Broecker, *J. Leukoc. Biol.*, 2001, **70**, 491-509.
2. A. Muller, B. Homey, H. Soto, N. F. Ge, D. Catron, M. E. Buchanan, T. McClanahan, E. Murphy, W. Yuan, S. N. Wagner, J. L. Barrera, A. Mohar, E. Verastegui and A. Zlotnik, *Nature*, 2001, **410**, 50-56.
3. N. Andrew and R. H. Insall, *Nature Cell Biology*, 2007, **9**, 193-U191.
4. A. K. Harris, D. Stopak and P. Wild, *Science*, 1980, **208**, 177-179.
5. U. S. Schwartz, N. Q. Balaban, D. Riveline, A. Bershadsky, B. Geiger and S. A. Safran, *Biophys. J.*, 2002, **83**, 1380-1394.
6. G. Pfister, C. M. Stroh, H. Perschinka, M. Kind, M. Knoflach, P. Hinterdorfer and G. Wick, *Journal of Cell Science*, 2005, **118**, 1587-1594.
7. S. M. Richardson-Burns, J. L. Hendricks and D. C. Martin, *J. Neural Eng.*, 2007, **4**, L6-L13.
8. P. S. Thapa, B. J. Ackerson, D. R. Grischkowsky and B. N. Flanders, *Nanotechnology*, 2009, **20**, 235307.
9. D. J. Watts and J. M. Ashworth, *The Biochemical Journal.* , 1970, **119**, 171-174.
10. L. D. Landau and E. M. Lifshitz, *Theory of Elasticity*, Butterworth-Heinemann, Oxford, 2000.
11. J. A. Araujo, F. C. Téran, R. A. Oliveira, E. A. A. Nour, M. A. P. Montenegro, J. R. Campos and R. F. Vazoller, *J. Electron Micros.*, 2003, **52**, 429-433.
12. B. Geiger, J. P. Spatz and A. D. Bershadsky, *Nature Reviews*, 2009, **10**, 21-33.
13. K. S. K. Uchida and S. Yumura, *J. Cell .Sci.*, 2004, **117**, 1443-1455.
14. J. L. Hutter and J. Bechhoefer, *Rev. Sci. Instrum.*, 1993, **64**, 1868-1873.
15. S. Yang and T. Saif, *Rev. Sci. Instrum.*, 2005, **76**, 044301.
16. R. S. Gates and M. G. Reitsma, *Rev. Sci. Instrum.*, 2007, **78**, 086101.
17. H. Okuzaki and M. Ishihara, *Macromol. Rapid Commun.*, 2003, **24**, 261-264.
18. D. Tahk, H. H. Lee and D. Y. Khang, *Macromolecules*, 2009, **42**, 7079-7083.

Chapter 5 - Long reach cantilevers for sub-cellular force measurements

(Published in *Nanotechnology* 2012, **23**, 455105. The original manuscript is presented in Appendix B.)

Abstract

Maneuverable, high aspect ratio poly 3-4 ethylene dioxythiophene (PEDOT) fibers are fabricated for use as cellular force probes that can interface with individual pseudopod adhesive contact sites without forming unintentional secondary contacts to the cell. The straight fibers have lengths between 5 and 40 μm and spring constants in the 0.07-23.2 nN μm^{-1} range. The spring constants of these fibers were measured directly using an atomic force microscope (AFM). These AFM measurements corroborate determinations based on the transverse vibrational resonance frequencies of the fibers, which is a more convenient method. These fibers are employed to characterize the time dependent forces exerted at adhesive contacts between apical pseudopods of highly migratory *D. discoideum* cells and the PEDOT fibers, finding an average terminal force of 3.1 ± 2.7 nN and lifetime of 23.4 ± 18.5 s to be associated with these contacts.

5.1. Introduction

Pseudopod-facilitated motility is a critical aspect of the amoeboid migration exhibited by *D. discoideum*, neutrophils, T lymphocytes [1], and other highly migratory cells [2]. These cells crawl at rates as large as ~30 μm min^{-1} to forage for micro-organisms and antigens in their local environments [3]. To achieve such high speeds, the cells must adhere to and release the supporting substrates quickly. Pre-aggregative (*i.e.* migratory) *D. discoideum*, for example, were recently reported to form adhesive contacts (called actin foci) that form and decay on ~20 s time scales [4].

The short-lived nature of these contacts differs significantly from the ~20 min lifetimes of the *focal adhesion complexes* used by slow-migrating cells like keratinocytes and fibroblasts [5]. In contrast to focal adhesion complexes, which have been intensively studied at the single complex level for over a decade [6-8], comparatively little is known about the adhesive structures and dynamics of highly migratory cells.

The amoeboid paradigm of cellular movement [9, 10] essentially consists of reception of stimuli (*e.g.* a signaling molecule at a cell-surface receptor) followed by the localized protrusion of exploratory appendages, such as pseudopods, from the cell. A typical pseudopod [figure 5.1(a)] is a few microns in length and has a submicron tip size. A cell may protrude many pseudopods at a given time. Commonly, the pseudopod will adhere its foremost tip to the local substrate [9-11]. Contraction of the actin cytoskeleton along the pseudopod-axis (by molecular motors) pulls the cell towards the adhesive contact. The molecular-level mechanisms by which pseudopods adhere to substrates for both *D. discoideum* and *amoeboid* leukocytes are not known [12, 13]. However, these are the first contacts that the cell makes with the anterior substrate, and the traction forces exerted against the substrate at these sites dictate the cell's instantaneous direction-of-migration. Hence, they are a key aspect of amoeboid motility. Characterization of the dynamical forces exerted at these contacts would constitute a key step towards resolving the potential energy surface associated with the adhesion and, ultimately, controlling the transient adhesive contact mechanism in highly migratory cells.

A variety of methods are used to characterize the forces that cells exert at their adhesive substrate-contacts. The deformable substrate technique measures cell-induced wrinkling or

marker-displacement within an elastic substrate [14]. This approach does not directly measure the forces exerted at the individual contacts, but rather extracts them by modeling the deformation-map induced by the whole-cell. This can be a non-trivial undertaking [15]. Approaches that utilize atomic force microscopy (AFM) provide excellent resolution of the dynamical forces exerted between cells and substrates [16]. *Single-cell force spectroscopy* [17] entails the attachment of a living cell to an AFM cantilever that is then lowered into contact with a substrate. The substrate is typically functionalized with a ligand of interest (*e.g.* fibronectin) [18, 19]. The force on the AFM cantilever is then measured as the cantilever-cell unit is retracted from the substrate. This method has shed light on a wide range of ligand-receptor adhesive interactions [20-22], as have the conceptually similar biomembrane force probe [23] and laser trap [24] methods. A challenge for such cell-as-probe techniques lies in minimizing the contact area to a single, cell-initiated adhesive contact: that between a pseudopod tip and a substrate, for example.

What is needed is a long, thin probe that can interface with targeted sites, such as the adhesive contacts of pseudopods, without forming unintentional secondary contacts to the cell. Therefore, this study presents a methodology for fabricating and calibrating high aspect ratio PEDOT fibers for use as cellular force probes. These cantilevers are an improvement over on-chip PEDOT force sensors reported recently [25] because these cantilevers are considerably easier to calibrate, and they may be maneuvered independently around a cell and, permitting both lateral and apical (topside) targets on the cellular surface to be probed. This capability enables interrogation of the off-plane, pseudopod-facilitated motility that occurs in nature when amoeboid cells migrate through 3D matrices.

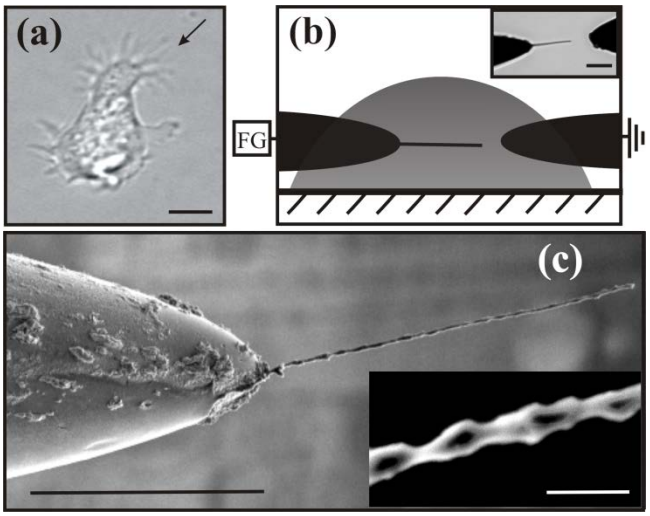

Figure 5.1. (a) Optical micrograph of a *D. Discoideum* cell extending pseudopods. A pseudopod is indicated by the arrow. Scale bar = 5 μm. (b) Schematic depicting the side-view of the experimental set-up for PEDOT fiber growth. FG designates a function generator. Inset: optical micrograph depicting the bottom view of the set-up. Scale bar = 10 μm. (c) SEM image of a PEDOT fiber grown from an etched tungsten tip. Scale bar = 20 μm. Inset: enlarged view of the fiber. Scale bar 1μm.

5.2. Experimental Methods

Direct characterization of a ~400 nm wide pseudopod [see figure 5.1(a)] requires a probe of comparable dimension. The probe should also have a sufficiently high aspect ratio to allow it to cleanly reach a targeted site without forming unintentional, secondary contacts with the cell. To meet these requirements, we have fabricated cantilevered force sensors composed of poly(3,4-ethylene dioxythiophene) (PEDOT) fibers grown from the tips of etched tungsten wire. The bottom 5 mm of a vertically oriented, electrically grounded tungsten filament (0.019 in diameter, SmallParts) were electro-etched by repeated dipping over a ~4 min period into a 10 M $NaNO_2$ 6MKOH solution that was biased at +4 V, as described elsewhere [26]. This procedure yields conical tips with radii-of-curvature of ~1 μm or less. Reproducibility was optimized by using a

sewing machine to cycle the filament in and out of solution at a rate of ~10 s^{-1}. We used the simple polymerization technique *directed electrochemical nanowire assembly* (DENA) to grow the PEDOT fiber from the tip of the tungsten filament [27-29]. Briefly, the tungsten filament was first evaporatively coated with ~200 nm of Au to promote strong attachment of the polymer. After mounting the coated filament in a 3D stage and positioning it ~1 μm above a microscope slide, a 20 μL aliquot of aqueous solution containing 0.01 M 3,4-ethylene dioxythiophene and 0.02 M poly(sodium styrene sulfonate) was deposited across the ~30 μm gap between the wire tip and an Au counter-electrode that was similarly mounted. Figure 5.1(b) is a schematic of this arrangement. A square wave voltage signal (±3.5 V, 10.0 kHz) was applied to the electrodes to induce PEDOT nano-fiber growth via electrochemical polymerization [30]. As explained elsewhere, the voltage-frequency sets the average radii of the fibers during growth [30], but spatio-temporal fluctuations in the polymerization rate of the amorphous PEDOT material give rise to radial variation (~50%) about the mean radius [28, 29]. The voltage signal is terminated after a few seconds when the PEDOT nano-fiber reaches the desired length. Translation of the microscope stage pulls the solution-drop away from the nano-fiber, straightening it due to the tension at the air-filament-solution contact line. The nano-fibers retain their straightened geometries upon re-immersion in aqueous solution. A scanning electron micrograph of a typical straightened nano-fiber is shown in figure 5.1(c).

We have used an atomic force microscope (AFM, *Model:* MFP-3D, Asylum Research) to directly measure the spring constants k_F of the PEDOT fibers, as detailed elsewhere [25]. Briefly, this was done by lowering a calibrated AFM cantilever (CSC12/tipless, MikroMasch) of spring constant k_C against an individual fiber in order to deflect it by distance Δz, as illustrated in figure

5.2(a) and plotted in figure 5.2(b) [31]. When the opposing forces exerted by the fiber and the cantilever are equal in magnitude, the following expression relates the spring constant of the fiber to the measured quantities [25, 32]:

$$k_F = k_C\left(\Delta z \big/ \delta_C - 1\right)^{-1}\left(\frac{L-\Delta L}{L}\right)^3 \cos^{-2}\theta. \qquad (1)$$

δ_c is the deflection of the cantilever and L is the length of the fiber. The tilt angle θ of the AFM cantilever was 11° for all cases in this study. The position of contact from the end of the fiber ΔL was measured via an internal optical microscope in the AFM.

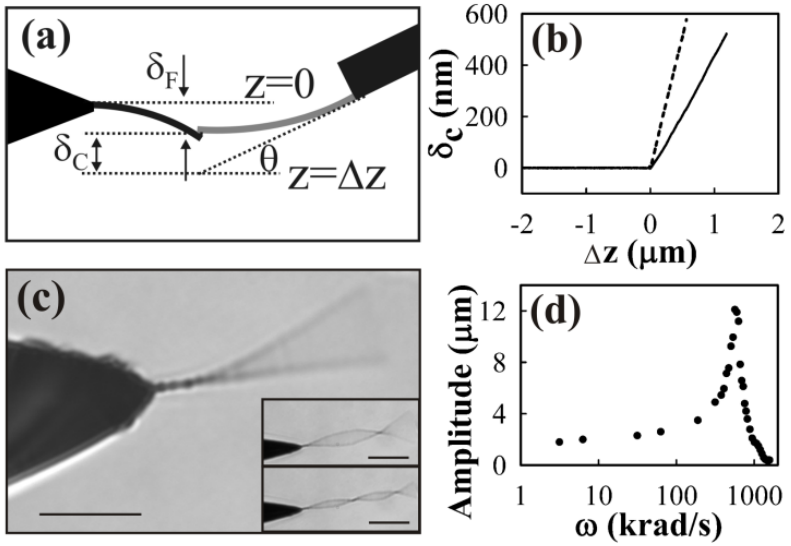

Figure 5.2. (a) Schematic of AFM-based set-up for measuring the spring constant of a PEDOT fiber. (b) AFM cantilever deflection magnitude δ_C versus vertical position of AFM head Δz for pressure against a rigid surface (dashed profile) and a PEDOT fiber (solid profile). (c) Optical micrograph of a PEDOT fiber resonating at its fundamental frequency. Scale bar = 15 μm. Inset: optical images of a PEDOT fiber resonating in its first (upper) and second (lower) harmonic modes. Scale bar = 15 μm. (d) Amplitude versus driving frequency plot for the PEDOT fiber in panel (c).

We have also determined the spring constants of the PEDOT cantilevers by the resonance-frequency method, which is technically simpler than the AFM method [33]. To measure the resonance frequency of a PEDOT fiber, we position this single PEDOT cantilever ~10 μm from an Au counter-electrode. A ± 20 V square wave voltage-signal of frequency *f* and a +20 V DC offset are applied to the PEDOT cantilever while the Au electrode is grounded [34]; polarization forces drive transverse oscillation of the PEDOT fiber at this frequency. A bright field image of a cantilever resonating in its fundamental mode is shown in figure 5.2(c). Images of the vibrating fiber are collected as *f* is increased in 5 kHz steps. A representative amplitude vs angular frequency plot is depicted in figure 5.2(d), where the angular frequency ω is defined as $\omega = 2\pi f$. The frequency at which the amplitude reaches its first maximum locates the fundamental resonance frequency ω_0 [565 krad s^{-1} in figure 5.2(d)]. Amplitude maxima at frequencies of half the observed resonance frequency were not observed, and the vibrational amplitude was directly proportional to the voltage-amplitude, confirming that the reported ω_0-values are fundamental frequencies [33]. The resonances of the tungsten filament are well-below those of the PEDOT cantilever and, hence, do not complicate these measurements. The spring constant k_{res} of a radially uniform and solid cantilevered rod of length *L* depends on ω_0 as

$$k_{res} = 0.08\frac{\pi\rho_m{}^2 L^5}{E}\omega_0{}^4. \qquad (2)$$

ρ_m is the mass density of the fiber material (PEDOT) and *E* its Young's modulus. (2) was derived by using the expression for ω_0 of a radially uniform rod $\omega_0 = 1.75\sqrt{E\rho^{-1}}rL^{-2}$ to eliminate *r* in the expression for the spring constant *k* of a uniform rod $k = \frac{3\pi E r^4}{4L^3}$ [35]. As explained below, (2)

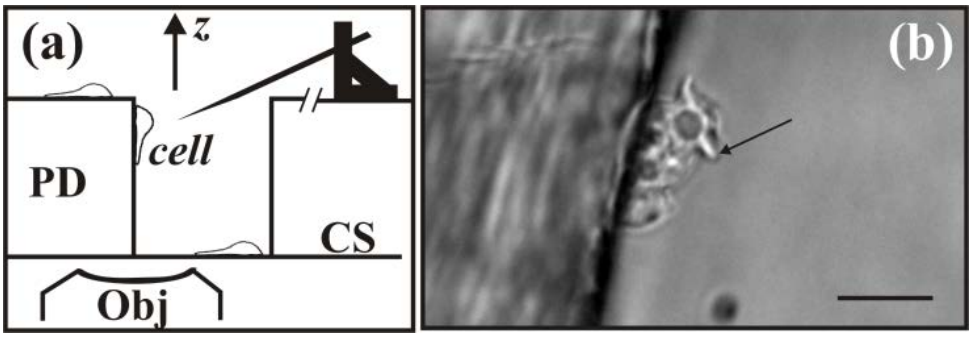

Figure 5.3. (a) Schematic (not to scale) of the side-view imaging set-up depicting the Petri dish (PD), cover-slip (CS), and microscope objective (Obj). (b) Side-view micrograph of a *D. Discoideum* cell extending apical pseudopods. The apical pseudopod indicated by the arrow is 2.5 μm long and ~400 nm wide. Scale bar = 10 μm.

was used to predict the spring constants of the PEDOT fibers.

Type KAx3 *D. discoideum* cells [36], grown at 24 ^{o}C, were removed from HL-5 culturing medium by drawing 1000 μL of the cell-medium suspension from a Petri dish and centrifuging the aliquot for ~10 s at 1.34×10^3 g. The supernatant was discarded and the cells were washed two times with 12mM phosphate buffer and shaken before suspending the cells a final time in phosphate buffer and starving them for 4-6 hours. 50 μL volumes of cell suspension and phosphate buffer were deposited in the side-view imaging chamber described below. A waiting time of ~20 minutes, following cell deposition, was required for the cells to settle and begin migrating on the surfaces of the chamber.

To facilitate investigation of apical pseudopods, which are important for amoeboid migration through 3D matrices, cells were visualized *in profile* so that the size, shape and cellular location of the pseudopod-fiber contact could be clearly observed. This mode requires that the imaging plane of the microscope be perpendicular to the substrate on which the cell

crawls. Our set-up for realizing this perspective, which differs from that reported elsewhere [37], is diagrammed in figure 5.3(a). Briefly, a hole was bored in the base of a Petri dish (Fisherbrand) using a 7/32" drill bit at 990 rpm; these parameters minimized lip and sidewall roughness (~3 μm). A cover-slip was cemented to the underside of the dish to seal the hole. *D. discoideum* cells were cultured and introduced to the chamber at cell surface densities of ~10^3 mm^{-2}. The dish was mounted on the stage of an inverted microscope (Leica IRB) for optical imaging, primarily with a 63× water immersion objective of 0.90 numerical aperture. Side-view imaging of the cells was accomplished by focusing the microscope on those migrating on the sidewalls of the hole. A typical side-view image of a *D. discoideum* cell is shown in figure 5.3(b). The arrow points to an apical pseudopod.

5.3. Results

We have directly measured the spring constants of 15 different PEDOT fibers by using an AFM as described above. The measured k_C, $\delta_C / \Delta z$, L, and ΔL values were substituted into (1) to obtain the corresponding k_F determinations. Each fiber was characterized 3 times. The average of the three k_F determinations is denoted $\bar{k}_F$. All quantities required to make these spring constant determinations are reported in Table 5.1 (fibers 1-15).

Figure 5.2(c) shows a PEDOT fiber (23 in Table 5.1) resonating in its fundamental mode at 90 kHz. (It also resonates in its harmonic modes, as the insets show, demonstrating its strong elastic character). Figure 5.2(d) is the amplitude versus frequency plot for the fiber of panel (c), indicating a fundamental resonance frequency ω_0 of 565×10^3 rad s^{-1}. By substituting this ω_0 value into (2), we obtain a prediction of its spring constant k_{res} of 7.0×10^{-4} N m^{-1}. In calculating

Table 5.1: Parameters for the Spring Constant Measurements.

Fiber	L (μm)	$\frac{\delta_C}{\Delta z}$	ΔL (μm)	k_C (nN/μm)	k_F (nN/μm)	$\overline{k_F}$ (nN/μm)	ω_0 (krad/s)	r_{res} (nm)	k_{res} (nN/μm)
1	7.22	0.28	0.5	58	18.9	18.0	7850	202	21.0
2	14.58	0.34	6.56	58	5.3	5.1	2292.2	241	5.1
3	15.08	0.22	6.56	61	3.2	3.1	2009.6	226	3.6
4	9.66	0.41	2.2	61	20.2	19.0	5149.6	238	16.7
5	10.66	0.45	3.9	64	13.6	13.8	4207.6	237	12.2
6	8.80	0.41	3.06	60	12.1	12.1	5338	204	12.1
7	8.74	0.47	2.18	60	23.2	23.2	6091.6	230	19.8
8	12.39	0.3	4.8	61	6.2	6.1	2888.8	219	5.7
9	7.94	0.55	3	65.9	20.1	21.6	6908	216	20.3
10	10.36	0.5	3.06	60.8	22.1	21.4	5024	267	21.5
11	9.19	0.34	2.18	60.8	14.3	14.0	5149.6	215	13.0
12	9.72	0.54	3.93	65.3	16.7	16.7	4961.2	232	14.8
13	9.36	0.49	3.5	65.3	15.6	16.3	5275.2	229	15.7
14	10.83	0.37	4.37	62.8	8	8.2	3705.2	215	7.9
15	8.44	0.36	2.6	61	11.7	11.0	5212.4	184	8.9
16	12.84	-	-	-	-	-	2449.2	200	3.6
17	17.0	-	-	-	-	-	1382	198	1.5
18	20.0	-	-	-	-	-	1118	221	1.4
19	23.0	-	-	-	-	-	942	247	1.4
20	24.0	-	-	-	-	-	816	232	1.0
21	28.41	-	-	-	-	-	439.6	176	0.2
22	34.0	-	-	-	-	-	377	216	0.3
23	30.0	-	-	-	-	-	565	252	0.7
24	41.0	-	-	-	-	-	220	183	0.07
25	16.73	-	-	-	-	-	1758.4	244	3.5

this result, we took the PEDOT Young's modulus E to be 2.0 GPa, the average of two recent determinations (1.8 GPa [38] and 2.26 GPa [39]), and the mass density ρ_m to be 1500 kg m^{-3} [40]. By using (2) we implicitly assume that a radially non-uniform PEDOT fiber of length L *both* resonates *and* bends like a hypothetical PEDOT fiber of a constant radius (and length L). This relation is not generally true of structurally non-uniform fibers. Therefore, in figure 5.4(a) we have assessed the extent to which the resonance-based determinations are accurate by plotting

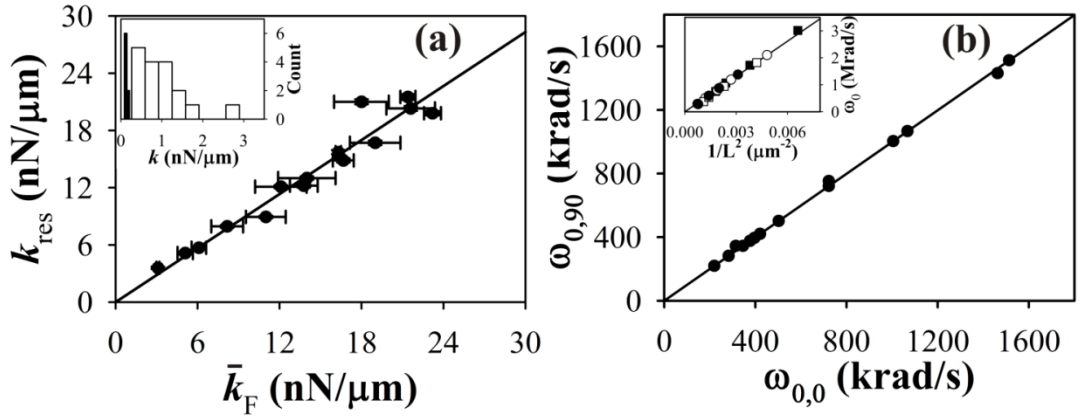

Figure 5.4. (a) Plot of resonance-based spring constant determinations k_{res} versus those measured by AFM $\overline{k_F}$ (filled circles). The solid line (constrained to pass through the origin) is the best fit to the points. The horizontal error bars denote the standard deviation of the mean associated with the $\bar{k}_F$ determinations; the vertical error bars, which are nearly too small to see, denote the propagated uncertainty in measuring ω and L. *Inset*: Distributions of the spring constants of fibers grown at 10.0 kHz to a length of 23.8 ± 0.8 μm (unfilled vertical bars) and at 20.0 kHz to a length of 23.4 ± 1.9 μm (filled vertical bars). (b) Plot of the fundamental resonance frequencies of PEDOT fibers $\omega_{0,0}$ against those measured when the fibers were axially rotated by 90° $\omega_{0,90}$. The solid line through the data points (filled circles) has a slope of unity. *Inset*: Plot of ω_0 for single fibers that were shortened (by breaking their tips) three times versus the inverse square of their lengths $1/L^2$. The solid line is a best fit through the data points. The four data-sets (circles, squares, unfilled circles, and unfilled squares) correspond to four different fibers.

the measured k_{res} values for 15 fibers against their measured $\bar{k}_F$ values. All parameters required to attain these k_{res} values are listed in Table 5.1 (Fibers 1-15). These data are best-fit by a line having a near unity slope of 0.95. It is clear that the k_{res}-values predict the spring constants of the PEDOT cantilevers with reasonable accuracy; moreover, in the small k range (~4 nN μm^{-1}) used in the cellular force application, the agreement is excellent. Hence, the resonance frequency calibration method, though approximate, is sufficiently accurate to justify forgoing the somewhat

laborious AFM method. Fibers 16-24 in Table 5.1, several of which were too compliant for the AFM method, were characterized using the resonance frequency method.

The inset to figure 5.4(a) depicts two spring constant distributions corresponding to two sets of fibers grown with different frequencies of the alternating voltage to approximately the same lengths. As described elsewhere [30], the frequency of the alternating voltage sets the average radii of the fibers, with higher frequencies producing thinner fibers. One distribution (unfilled vertical bars) describes 14 fibers grown using a frequency of 10.0 kHz to a length of 23.8 ± 0.8 μm (unfilled vertical bars). The average spring constant for these fibers is 0.8 ± 0.6 nN/μm. The other distribution (filled vertical bars) describes 8 fibers grown using a frequency of 20.0 kHz to a length of 23.4 ± 1.9 μm. The average spring constant of these fibers is 0.08 $\pm$ 0.04 nN/μm. Hence, the spring constants of the fibers may be controlled across reasonably narrow ranges by controlling the frequency of the alternating voltage during growth, as well as the length of the fiber.

To assess the degree to which the structural non-uniformity of the fibers causes anisotropy in their spring constants, we have measured the ω_0-values in planes-of-bending that differ by 90^o of axial rotation. These resonance frequency values are denoted $\omega_{0,0}$ and $\omega_{0,90}$. Figure 5.4(b) plots the measured $\omega_{0,90}$-value against the corresponding $\omega_{0,0}$-value for 12 different fibers. These data are well-fit by a line of unity slope, indicating that the $\omega_{0,0}$ and $\omega_{0,90}$ values for a given fiber are equal. Another concern is that the fibers grow unevenly such that their tips have different average thicknesses than their bases. The inset to figure 5.4(b) plots ω_0 for single fibers that were shortened (by breaking off their tips) three times versus the inverse square of

their lengths $1/L^2$. The different symbols represent the data-sets for the four fibers that were examined in this manner. These data lie along a single line, as indicated by the best-fit (solid line).

Figures 5.5(a)-(f) constitute a series of side-view images of a *D. discoideum* cell migrating on the vertical side-wall. An apical pseudopod adheres to the cantilever in panel (a), deflects it by exerting a pulling force on it in panels (b)-(d), and releases it in panel (e). A video of this event, shown at ~6 × the actual rate is available as supporting information. These images depict an apical pseudopod-cantilever deflection event, where the cantilever represents a secondary substrate. The measured deflection $\delta_F(L)$ of the fiber is extracted from these images by finding the distance between the tip of the deflected and undeflected fiber. (Drift of the microscope stage occurred at a rate of 0.09 μm/min and, therefore, does not compromise the $\delta_F(L)$ determinations). The shape of the pseudopod evolves throughout this event.

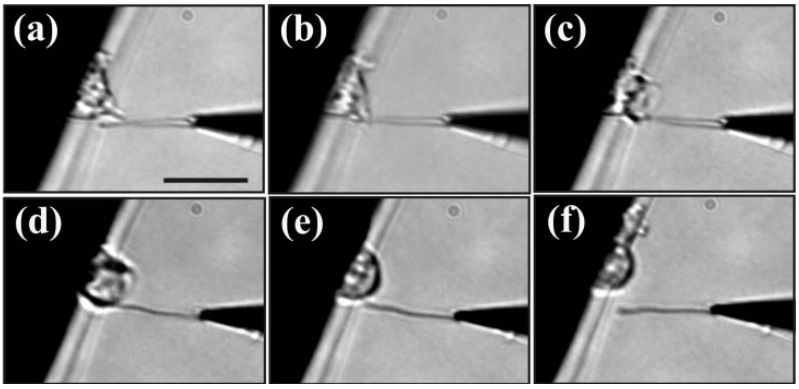

Figure 5.5. A series of optical micrographs of cantilevered PEDOT fiber (a) in its neutral position after contact initiation by the pseudopod; (b)-(d) while being deflected upwards by the cell at times 22 s, 68 s, 98 s, and 100 s respectively; and (f) at time 118 s when the fiber is back in its neutral position after release by the cell. The scale bar in panel (a) denotes 15 μm.

Figure 5.6(a) shows the fiber-end deflection-values $\delta_F(L)$ (unfilled circles) corresponding to the apical pseudopod deflection event of figure 5.5(a)-(f). This fiber—wire 25 in Table 1—was found to have a spring constant k_{res} of 3.5 ± 0.3 nN/μm. Conversion of the δ_F-values to forces f via Hooke's law ($f = \delta_F k_{res}$) yields the filled circles in figure 5.6(a). These data show that f reaches 8.5 nN without breaking contact. A total of 41 apical pseudopod-fiber deflection events were observed in this study. Figure 5.6(b) depicts the distribution of the terminal forces for these events. *Terminal force* refers to the force applied to the fiber the instant before it recoiled to its neutral position. The average terminal force was 3.1 ± 2.7 nN. Figure 5.6(c) depicts the distribution of the durations of these events. The average contact duration was 23.4 ± 18.5 s.

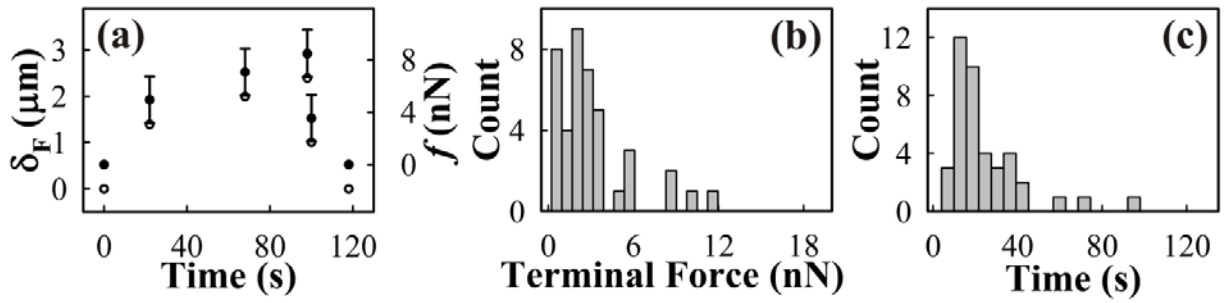

Figure 5.6. (a) Apical pseudopod induced deflection (unfilled circles) and force (filled circles) measured during the event depicted in figure 5. The error bars reflect the propagated uncertainties of δ_F and k_{res}. (b) Distribution of the terminal forces obtained from 41 pseudopod-fiber deflection events. (c) Distribution of contact durations obtained from the same set of 41 events.

5.4. Discussion

This study presents methodology for fabricating cantilevered cellular force sensors composed of PEDOT fibers grown from maneuverable substrates. The diameter and length of a fiber are user-controlled during the growth process and, consequently, the spring constants of the fibers may be controlled across reasonably narrow ranges as shown in the inset to figure 5.4(a). These force sensors are calibrated either by measuring the fibers' spring constants directly via AFM or, more conveniently, by finding their resonance frequencies for transverse vibration. The near-unity slope of figure 5.4(a) implies that the resonance frequency calibration method [*i.e.* equation (2)], though approximate, is sufficiently accurate to forego the more laborious AFM method. In applying (2) to the PEDOT fibers, we assume that the fiber bends like a hypothetical uniform fiber having a particular radius and vibrates like a uniform fiber of the same radius. However, the PEDOT fibers are radially non-uniform [inset of figure 5.1(c)]. For structurally non-uniform cantilevers, this assumption is not strictly true. The spring constant and the resonance frequencies of a cantilever are derived from different forms of Newton's 2nd Law: for the former, there is no net torque on the fiber; for the latter the net torque varies periodically with time. Hence, it is somewhat fortuitous that the resonance-based spring constant determinations were found to be accurate [figure 5.4(a)]. The theoretical analysis required to quantify the limits of this approximation lie beyond the scope of this work. However, because the resonance-method is in wide use in the calibration of micro- and nano-cantilevers, we feel that elucidation of the limits of this assumption is needed, and we will present such an analysis in forthcoming work.

Because the fibers are radially non-uniform and somewhat axially asymmetric, concern over the anisotropy of their spring constants arises. Figure 5.4(b) shows that the resonance

frequency values in planes-of-bending that differ by 90^o of axial rotation are essentially equal for a given fiber. Because ω_0 predicts k_F to a reasonable degree of accuracy (discussed above), this finding implies that the spring constants in orthogonal bending planes are essentially the same; thus, we do not observe a significant degree of bending anisotropy. A related concern is that the fibers grow unevenly, causing their foremost tips to have different average radii than their bases. A radially uniform fiber has a resonance frequency of $\omega_0 = 1.75\sqrt{E\rho^{-1}}rL^{-2}$. Hence, the inset to figure 5.4(b) shows that the PEDOT fibers resonate like radially uniform fibers as shortening the fibers does not change the slope ($1.75\sqrt{E\rho^{-1}}r$) of their ω_0 versus L^{-2} plots. These data also provide further confirmation that fibers grown under the same controlled conditions have similar structures, as each of the four data-sets shown in this plot has the same slope. Hence, these findings presented in figures 5.4(a) and (b) establish a basis for calibrating these fibers via the comparatively straight-forward resonance method.

Typical lengths of the PEDOT fibers are ~20 μm, which provides sufficient reach to cleanly interface the tip of a fiber with a subcellular target on a cell without forming unintentional secondary contacts to the cell. To demonstrate this capability, we have resolved the dynamical forces that arise at individual adhesive contacts between the tips of apical pseudopods and the PEDOT cantilevers. Most prior work on pseudopod dynamics has regarded motility on planar substrates such as Petri dishes and microscope slides. However, apical pseudopod dynamics are required of *D. discoideum* in nature where the local topography of forest floors—crevices and debris—necessitates off-plane motion of a cell as it transfers from one surface to another. By employing the dynamical force sensors, the present study found the average terminal force exerted during the apical pseudopod-secondary substrate adhesive

contacts to be 3.1 ± 2.7 nN and the average duration of these contacts to be 23.4 ± 18.5 s. This period compares well to the 19.4 ± 8.2 s lifetimes of the adhesive contacts made by actin foci to *basal* substrates [41], suggesting that the adhesive structures at the apical pseudopod-tips may be actin foci. However, no external forces were applied to the actin-foci in this prior study (although internal forces could have been present) [41]. This detail is significant because the application of a force against a bond accelerates the dissociation rate of the bond [42]. Hence, when a pulling force is applied against an actin focus, it is expected to decay more rapidly than the 19.4 s average lifetime in the unforced case. On the other hand, apical contacts can survive for 23.4 s under few nano-Newton external forces [figures 5.6(a) and (b)]. This comparative robustness is expected to increase the probability that apical contacts survive while the pre-existing basal contacts (actin foci) decay, as required for inter-substrate (basal-to-apical) transfer. Further investigation into this mechanism will be undertaken in a future study.

5.5. Conclusion

This study has presented an innovative methodology for the electrochemical fabrication of cellular force sensors composed of cantilevered PEDOT fibers. Calibration of the force sensors is straight-forward via measurement of the transverse resonance frequencies of the fibers. By employing these fibers to characterize the dynamics of apical pseudopod-substrate adhesive contacts of *D. discoideum* cells, we have shown that these cantilevers are effective, high aspect ratio cellular force probes that may be positioned independently around the cell and can interface with sub-micron targets without forming unintentional secondary contacts to the cell. These capabilities will permit further statistical characterization of the durations and magnitudes of the forces exerted at individual apical and lateral pseudopod substrate contacts, as a means of

elucidating the physical basis of pseudopod-substrate adhesion. We also note that the dimensions and maneuverability of the PEDOT force probes will likely permit characterization of the dynamics at other interesting adhesive entities such as the setae and spatulae of gecko feet [43] and the micro-bristles of beetle tarsi [44], which have dimensions comparable to *D. discoideum* pseudopods.

5.6 Acknowledgements

This work was partially supported by National Science Foundation grants PHY-0646966 (BNF) and DMR-0603144 (BML). We thank Professor Robert Szoszkiewicz for helpful suggestions regarding cantilever calibration.

5.7 References

1. P. Friedl, S. Borgmann and E. B. Broecker, *J. Leukoc. Biol.*, 2001, **70**, 491-509.
2. A. Muller, B. Homey, H. Soto, N. F. Ge, D. Catron, M. E. Buchanan, T. McClanahan, E. Murphy, W. Yuan, S. N. Wagner, J. L. Barrera, A. Mohar, E. Verastegui and A. Zlotnik, *Nature*, 2001, **410**, 50-56.
3. T. P. Stossel, *Blood*, 1994, **84**, 367-379.
4. S. Yumura and T. Kitanishi-Yumura, *Cell Struct. Funct.*, 1990, **15**, 355-364.
5. X. S. Ren, W. B. Kiosses, D. J. Sieg, C. A. Otey, D. D. Schlaepfer and M. A. Schwartz, *J. Cell .Sci.*, 2000, **113**, 3673-3678.
6. C. G. Galbraith and M. P. Sheetz, *Proc. Natl. Acad. Sci.*, 1997, **94**, 9114-9118.
7. N. Walter, C. Selhuber, H. Kessler and J. P. Spatz, *Nano Lett.*, 2006, **6**, 398-402.
8. V. Vogel and M. Sheetz, *Nature Reviews: Molecular Cell Biology* 2006, **7**, 265-275.
9. P. N. Devreotes and S. H. Zigmond, *Annual Review of Cell Biology*, 1988, **4**, 649-686.
10. M. Bailly, J. S. Condeelis and J. E. Segall, *Microsc. Res. Technol.*, 1998, **43**, 433-443.
11. T. P. Stossel, J. H. Hartwig, P. A. Janmey and D. J. Kwiatkowski, *Biochem. Soc. Symp.*, 1999, **65**, 267-280.
12. P. Friedl, F. Entschladen, C. Conrad, B. Niggermann and K. S. Zanker, *Eur. J. Immunol.*, 1998, **28**, 2331-2343.
13. P. Friedl and B. Weigelin, *Nature Immunology*, 2008, **9**, 960-969.
14. A. K. Harris, D. Stopak and P. Wild, *Science*, 1980, **208**, 177-179.
15. U. S. Schwartz, N. Q. Balaban, D. Riveline, A. Bershadsky, B. Geiger and S. A. Safran, *Biophys. J.*, 2002, **83**, 1380-1394.

16. G. Pfister, C. M. Stroh, H. Perschinka, M. Kind, M. Knoflach, P. Hinterdorfer and G. Wick, *Journal of Cell Science*, 2005, **118**, 1587-1594.
17. J. Helenius, C.-P. Heisenberg, H. E. Gaub and D. J. Muller, *Journal of Cell Science*, 2008, **121**, 1785-1791.
18. Z. Sun, L. A. Martinez-Lemus, A. Trache, J. P. Trzeciakowski, G. E. Davis, U. Pohl and G. A. Meininger, *Am. J. Physiol.*, 2005, **289**, H5226-H2535.
19. A. Trache, J. P. Trzeciakowski, L. Gardiner, Z. Sun, M. Muthuchamy, M. Guo, S. Y. Yuan and G. A. Meininger, *Biophys. J.*, 2005, **89**, 2888-2898.
20. J. Friedrichs, J. Helenius and D. J. Mueller, *Proteomics*, 2010, **10**, 1455-1462.
21. S. Hoffmann, B. H. Hosseini, M. Hecker, I. Louban, N. Bulbuc, N. Garbi, G. H. Wabnitz, Y. Samstag, J. P. Spatz and G. J. Haemmerling, *Immunology Letters*, 2011, **136**, 13-20.
22. S. C. Hoffmann, G. H. Wabnitz, Y. Samstag, G. Moldenhauer and T. Ludwig, *International Journal of Cancer*, 2011, **128**, 2096-2104.
23. E. Evans, K. Ritchie and R. Merkel, *Biophys. J.*, 1995, **68**, 2580-2587.
24. R. I. Litvinov, H. Shuman, J. S. Bennett and J. W. Weisel, *Biophys. J.*, 2002, **84**, 1252-1262.
25. G. Paneru, P. S. Thapa, S. P. McBride, D. M. Nichols, B. M. Law and B. N. Flanders, *Appl. Phys. Lett.*, 2011, **99**, 093702.
26. Y. Qiao, J. Chen, X. Guo, D.cantrell, R. Ruoff and J. Troy, *Nanotechnology*, 2005, **16**, 1598-1602.
27. P. S. Thapa, D. J. Yu, J. P. Wicksted, J. A. Hadwiger, J. N. Barisci, R. Baughman and B. N. Flanders, *Appl. Phys. Lett.*, 2009, **94**, 033104.
28. P. S. Thapa, B. J. Ackerson, D. R. Grischkowsky and B. N. Flanders, *Nanotechnology*, 2009, **20**, 235307.
29. B. N. Flanders, *Mod. Phys. Lett. B*, 2012, **26**, 1130001.
30. B. Ozturk, I. Talukdar and B. N. Flanders, *Nanotechnology*, 2007, **18**, 365302.
31. S. Yang and T. Saif, *Rev. Sci. Instrum.*, 2005, **76**, 044301.
32. R. S. Gates and M. G. Reitsma, *Rev. Sci. Instrum.*, 2007, **78**, 086101.
33. R. Gao, Z. L. Wang, Z. Bai, W. A. deHeer, L. Dai and M. Gao, *Phys. Rev. Lett.*, 2000, **85**, 622-625.
34. J. Zhou, C. S. Lao, P. Gao, W. Mai, W. L. Hughes, S. Z. Deng, N. S. Xu and Z. L. Wang, *Sol. State. Comm.*, 2006, **139**, 222-226.
35. L. D. Landau and E. M. Lifshitz, *Theory of Elasticity*, Butterworth-Heinemann, Oxford, 2000.
36. D. J. Watts and J. M. Ashworth, *The Biochemical Journal.* , 1970, **119**, 171-174.
37. O. Chaudhuri, S. Parekh, W. Lam and D. Fletcher, *Nature Methods*, 2009, **6**, 383-387.
38. H. Okuzaki and M. Ishihara, *Macromol. Rapid Commun.*, 2003, **24**, 261-264.
39. D. Tahk, H. H. Lee and D. Y. Khang, *Macromolecules*, 2009, **42**, 7079-7083.
40. L. Nu, C. Kvarnström, K. Fröberg and A. Ivaska, *Synthetic Metals*, 2001, **122**, 425-429.
41. K. S. K. Uchida and S. Yumura, *J. Cell .Sci.*, 2004, **117**, 1443-1455.
42. P. Hänggi, P. Talkner and M. Borkovec, *Rev. Mod. Phys.*, 1990, **62**, 251-342.
43. G. Huber, H. Mantz, R. Spolenak, K. Mecke, K. Jacobs, S. N. Gorb and E. Arzt, *Proc. Natl. Acad. Sci.*, 2005, **102**, 16293-16296.
44. T. Eisner and D. J. Aneshansley, *Proc. Natl. Acad. Sci.*, 2000, **97**, 6568-6573.

Chapter 6 - Complete reconfiguration of dendritic gold

(Published in *Nanoscale* 2014, **6**, 833-841. The original manuscript is presented in Appendix C.)

Abstract

The present work extends the *directed electrochemical nanowire assembly* (DENA) methodology, which is a technique for growing single crystalline metallic nanowires and nano-dendrites from simple salt solutions, to enable the complete dissolution of the metallic dendrites following their growth. The experimental parameters that control this process are the frequency and the duty cycle of the alternating voltage signal that initiates electrochemical dendritic growth. Cyclic voltammetric and Raman measurements imply that the reconfiguration of dendritic gold occurs by way of the same interfacial reduction and oxidation mechanisms as bulk gold. We present a model that illustrates how the experimental parameters (frequency and duty cycle) induce reconfiguration by controlling the rates at which reduction, oxidation, and $Au^{III}Cl_4^-$ diffusion take place. This capability is significant because in making dendritic solidification a reconfigurable process, we have established an innovative means of applying fully reconfigurable metallic nano-structures to substrates; in turn, this capability could potentially enable the smart modulation of the adhesive, anti-corrosive, or optical properties of the substrate.

6.1. Introduction

A large number of materials that are capable of high dynamic range structural reconfiguration have been developed in the past few years.[1] Materials with this capability could potentially be used to confer hydrophobic, lipophobic, and anti-corrosive character to substrates in a *regenerative* manner. Structural reconfiguration is also important for man-made *smart* materials

that adapt advantageously to environmental changes. Cuttlefish-skin[2] and photosynthetic corals[3] are naturally occurring, oft-cited examples of such materials. As such, reconfigurability-by-design is an important strategy in modern materials science.

The synthesis of specialized building blocks is a widely used strategy for developing reconfigurable materials. Regan and co-workers have synthesized modular peptides that assemble in solution into smart gels. These gels, having pore-sizes sufficient to trap 26 kDa proteins, undergo complete, salinity-dependent dissolution (*i.e.* cargo-release) and reformation.[4] Pine and co-workers have designed quasi-monopolar magnets that self-assemble into aggregates with reproducible configurations. These assemblies can be fully disassembled or re-assembled by controlling the external magnetic field or the salinity of the surrounding solution.[5] The basic strategy of these approaches is to produce a specialized building block that switches its character in response to a changing external field, inducing reconfiguration of the assemblies. However, in naturally occurring environments such as oceans or rivers, one would not attempt to concentrate the waters with synthetic building blocks. Instead, it would be advantageous to control the assembly and disassembly processes of more generic building blocks, such as the components of the salts that are already extant. One could then envision producing nanostructured coatings on the surfaces of, say, underwater metrological apparatus in order to provide corrosion, reflectivity, or adhesion control that could be regenerated as needed.[6-8]

As a step towards this end, the present work extends the *directed electrochemical nanowire assembly* (DENA) methodology[9] to enable the on-command growth and dissolution of arrays of metallic dendrites on conducting surfaces that are immersed in salty solutions. DENA

is a type of dendritic solidification,[10-14] a widely occurring process that produces crystals having the distinctive *dendritic* shape observed at the hexagonal points of snowflakes.[15] In general, dendritic solidification occurs when the growth rate of a crystal limited by the diffusion of the building blocks, usually atoms or molecules, through a *bulk* medium to the solidification front.[16, 17] Spatio-temporal fluctuations in building block deposition rate create sharp protrusions on the solidification front. With further growth, the Mullins-Sekerka instability tends to enhance the growth rate and reduce the tip-radius, while the Gibbs-Thomson effect tends to retard the growth rate and fatten the tip.[18] The result is a dendrite that grows steadily with a fixed tip size.[14] Growth is in the direction of maximum surface tension; side-branches, induced by fluctuations in the deposition rate, grow in crystallographic directions that are commensurate with the main branch.[13, 19] In addition to bulk diffusion, DENA[20-22] also depends on the electrochemical oxidation and reduction of metal atoms at the crystal-solution *interface*. Therefore, in order to understand how the dendritic reconfiguration process occurs, both the interfacial chemical steps and the bulk diffusive process must be taken into account.

We focus on gold dendrites in this study because the electrochemistry of bulk gold is well-characterized.[23] The chemical steps underlying the dissolution of gold in chloride-rich, aqueous solutions are shown in reaction scheme (1):[23]

$$Au^{0}(s) + Cl^{-} \leftrightarrow Au^{I}Cl_{Ad} + e^{-} \qquad 1(a)$$

$$xAu^{I}Cl_{Ad} + 3xCl^{-} \leftrightarrow xAu^{III}Cl_{4}^{-}(aq) + 2xe^{-} \qquad 1(b)$$

$$(1-x)Au^{I}Cl_{Ad} + (1-x)Cl^{-} \leftrightarrow (1-x)Au^{I}Cl_{2}^{-}(aq) \qquad 1(c)$$

where the superscripts denote the oxidation states of *Au*, and *x* is the fraction of Au^{I} moiety that is oxidized to $Au^{III}Cl_4^-$. Essentially, this mechanism says that the electro-dissolution of bulk gold occurs when an Au^0 atom from the solid matrix coordinates with a Cl^- atom from the solution to

form the adsorbate $Au^{I}Cl_{Ad}$. The solid Au^{0} atom is oxidized to Au^{I} in this step [1(a)]. Subsequent chloride binding and oxidation yields the dissolved products $Au^{III}Cl_4^-$ (*aq*) [1(b)] and $Au^{I}Cl_2^-$ (*aq*) [1(c)]. The chemical steps underlying the deposition of $Au^{(0)}$ are shown in reaction scheme (2) as follows:[23]

$$Au^{III}Cl_4^-(aq) + 3e^- \leftrightarrow Au^0 + 4Cl^- \qquad 2(a)$$

$$Au^{I}Cl_2^-(aq) + e^- \leftrightarrow Au^0 + 2Cl^- \qquad 2(b)$$

These reactions imply that the electro-deposition of gold occurs when a solvated $Au^{III}Cl_4^-$ species [2(a)] or $Au^{I}Cl^-$ species [2(b)] arrives at the electrode which then reduces the Au^{III} or Au^{I} moieties to $Au^{(0)}$.

A key question regards the extent to which these processes that occur with bulk gold under DC biases accurately describe the interfacial chemistry of dendritic gold under the AC voltages that the DENA method employs. This information allows us to take the next step of developing a theoretical model for how these interfacial chemical mechanisms act in conjunction with the diffusion of $Au^{III}Cl_4^-$ through the bulk solution to enable dendritic reconfiguration. This theory indicates that our methodology functions by attaining independent control over the joining and leaving rates of atoms to the crystal, thus providing a basis for applying fully reconfigurable metallic nano-structures to substrates. Because this methodology relies on the aqueous electrochemistry of simple salts—not just gold chloride—this approach could potentially be applied in oceanic environments. As such, it has the potential to provide sustainable routes to coatings for corrosion, reflectivity, and adhesion control at immersed surfaces.

6.2. Experimental Design

Figure 6.1(a) depicts the set-up for controlling the dendritic growth of gold via the DENA technique. This method, which produces individual nanowires and nano-dendrites by

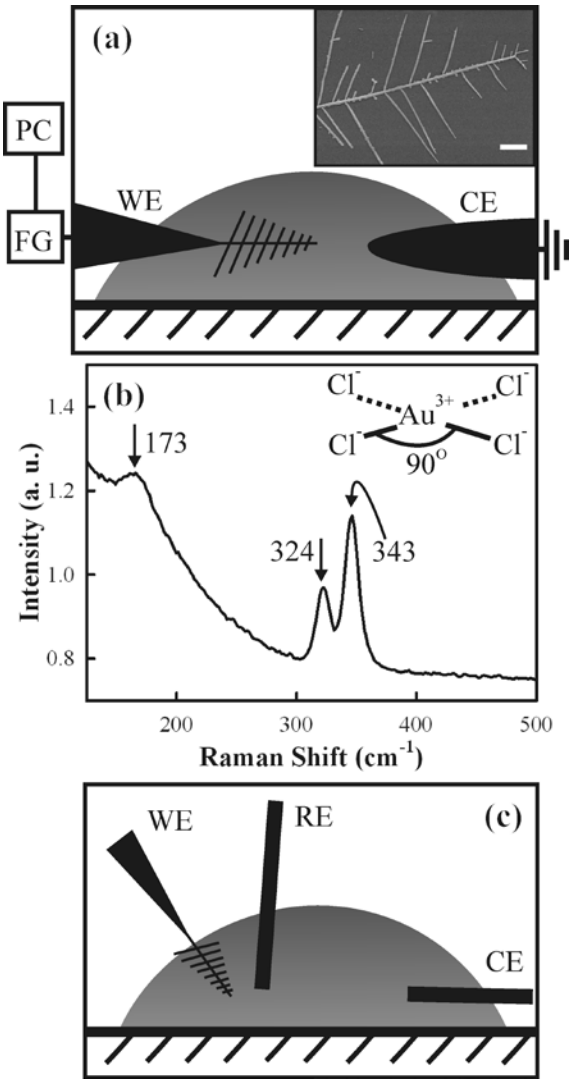

Figure 6.1. (a) Schematic depicting the side-view of the experimental set-up for the growth of gold dendrites. FG designates a function generator that is controlled by a personal computer PC via Labview. Inset: SEM image of a gold dendrite. Scale bar = 2 μm. (b) Raman spectrum of 20.0 mM $HAuCl_4$ solution. Inset: Structure of $Au^{III}Cl_4^-$ ions. (c) Schematic depicting the 3-electrode set-up used to measure cyclic voltammagrams of gold dendrites. WE, RE, and CE designate the working electrode, reference electrode, and counter electrode, respectively.

electrochemical dendritic solidification, is described elsewhere.[9, 21] The set-up consists of an electrode pair immersed in aqueous $HAuCl_4$ solution. The counter-electrode (CE) is composed of platinum wire (Kurt J. Lesker, 0.5 mm diameter). The working electrode (WE), which has a sharper tip, is composed of a piece of tungsten filament, the tip of which is electro-etched to a ~1 μm radius-of-curvature.[24, 25] The tungsten filament (SmallParts, 0.2 mm diameter) is mounted in a 3D stage and positioned ~1 μm above a microscope slide that is mounted on an inverted microscope (Leica, IRB). The inter-electrode spacing is adjusted to ~ 30 μm. A 20 μl aliquot of solution composed of de-ionized (18 MΩ) water and 20.0 mM $HAuCl_4$ (Sigma Aldrich) is deposited across the inter-electrode gap. Figure 6.1(b) shows the Raman spectrum of this solution. The features at 173 cm^{-1}, 324 cm^{-1} and 343 cm^{-1} agree well with the known B_{1g} (bend), B_{2g} (asymmetric stretch), and A_{1g} (symmetric stretch) vibrational modes of $Au^{III}Cl_4^-$ (*aq*), respectively,[26] implying that gold exists predominantly as $Au^{III}Cl_4^-$ in the bulk solution. A function generator (Hewlett Packard, 8116A) was used to apply a square wave voltage signal (± 4.0 V, 20.0 MHz) to the working electrode while grounding the counter- electrode to induce growth of the dendrite at the sharper working electrode. Growth occurs within a range of frequencies, from 10.0MHz to 50.0 MHz A typical gold dendrite is shown in the scanning electron micrograph in the inset of Figure 6.1(a). The individual branches, which are thought to originate at random sites along sides of a dendrite due to fluctuations in the diffusion-limited $AuCl_4^-$ deposition rate,[19] have ~60 nm diameters and ~60° branching angles. We have shown elsewhere that the electron diffraction patterns collected from such dendrites quantitatively match the known diffraction patterns of bulk gold, indicating that these dendrites are composed of gold.[21] The applied potential serves to select the growth direction in the lab frame by

controlling the direction of $AuCl_4^-$ from solution.[27] The crystallographic growth axis, however, is intrinsic to the crystal (*i.e.* in the direction of maximum surface tension).

Figure 6.1(c) is a schematic depicting the 3-electrode arrangement that we employed to measure cyclic voltammagrams of individual gold dendrites and also of bulk gold samples. After growing a dendrite from the tip of the working electrode, the $HAuCl_4$ solution was gently withdrawn and replaced with 0.1 M *KCl*. The working electrode was pulled out of the solution via a translational stage until only the dendrite remained in the solution; hence, the dendrite alone served as the working electrode. This arrangement ensures that only the electrochemistry of the gold dendrite and not that of the tungsten electrode will contribute to the cyclic voltammagram. Care must be taken that the air-water surface tension does not separate the dendrite from its substrate. To attain an I-ΔV profile, a voltage supply steps the potential difference ΔV of the working electrode forward by 25.0 mV relative to an Ag/AgCl reference electrode at a rate of 25.0 mV s^{-1}. ΔV is maintained potentiostatically via a Pt counter-electrode during each 1.0 s increment. The design of the homebuilt potentiostat is described elsewhere.[28] In a typical cyclic scan, the cross-cell current I that flows into the working-electrode was recorded by stepping ΔV forward in time from 0.0 V to 0.9 V and then back to 0.0 V. In plotting the current, we use the IUPAC convention that a positive (negative) current corresponds to negative (positive) charge flowing into (out of) the working electrode. The plot of I versus ΔV constitutes a cyclic voltammagram. To measure cyclic voltammagrams of bulk gold samples, the same set-up was used except that a segment of 0.5 mm diameter gold wire (Kurt J. Lesker, 99.99% pure) was substituted for the dendrite.

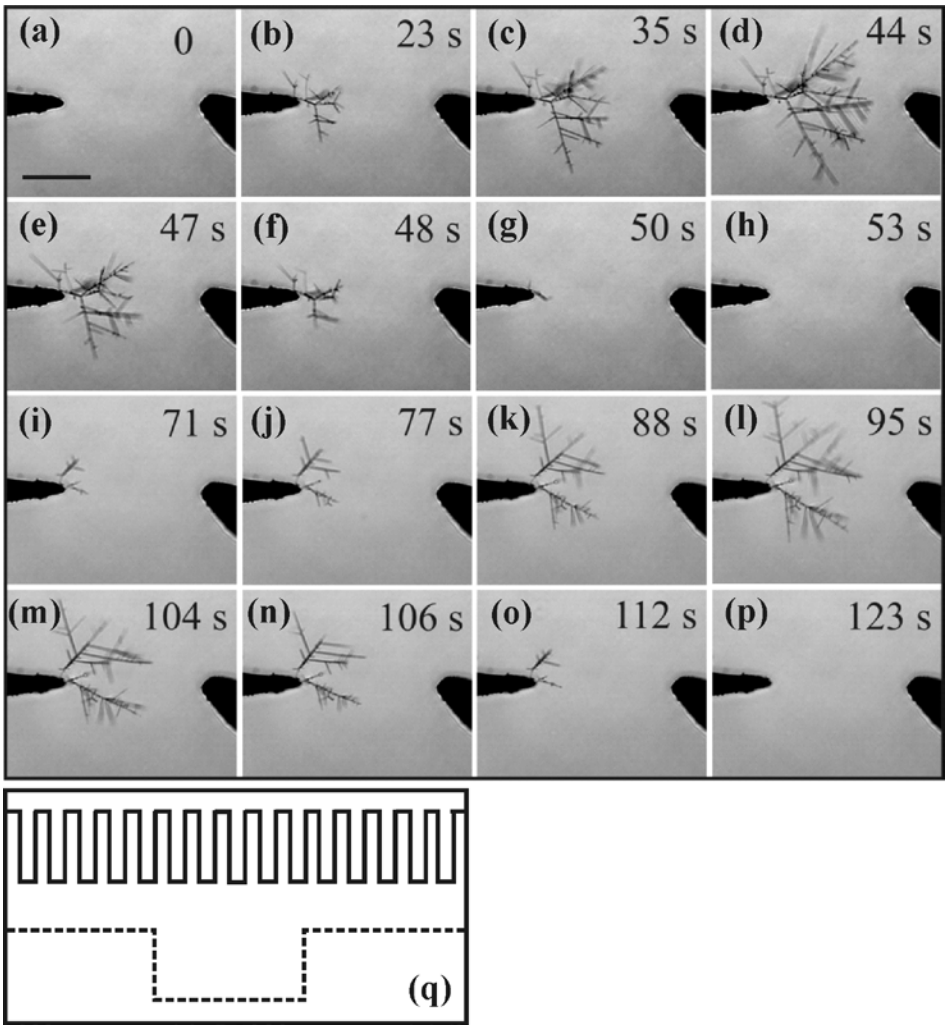

Figure 6.2. (a)-(p) Optical images showing growth and dissolution of gold dendrites by twice cycling the frequency of voltage signal (4.0 V amplitude, 50% duty cycle) between 34.0 MHz and 1.0 MHz. Scale bar = 50 μm. Panels (a)-(d) and (i)-(l) designate the growth stages. Panels (e)-(h) and (m)-(p) designate the dissolution stages. (q) Schematic depicting the square-wave signal used to grow (solid line) and dissolve (dashed line) the dendrites.

Full reconfiguration of the dendrite (*i.e.* growth followed by dissolution) is induced by variation of either the frequency or the duty cycle of the voltage signal. When the frequency *f* of the voltage signal is used to induce reconfiguration, the amplitude is held constant (usually at 4.0 V), the duty cycle is fixed at 50.0 %, and the frequency is lowered from a high value of greater

than 9.0 MHz to a low value of less than 3.0 MHz. An example of frequency-induced dendritic reconfiguration is depicted in Figure 6.2. When the duty cycle is used to induce reconfiguration, both the amplitude and the frequency of the voltage signal are held constant. A duty cycle of n means that the duration of the positive half cycle of the voltage signal is n % of its period f^{-1}. By increasing the duty cycle from less than 50.0 % to greater than 50.0 %, reconfiguration (*i.e.* growth followed by dissolution) is induced.

A Raman microscope (iHR550 Horriba-Jobin Yvon spectrometer fiber coupled to a BX-41 Olympus upright microscope) was used to interrogate single gold dendrites immersed in 0.1 M *KCl* aqueous solution. The microscope was equipped with a 0.8 NA 50 × objective and a 633.2 nm *HeNe* laser (Melles Griot), providing a diffraction-limited laser spot size of ~970 nm. To interrogate a dendrite during electrochemical growth or dissolution, the dendrite-laden tungsten filament and a platinum counter-electrode were mounted on the stage of the Raman microscope and immersed in a drop of the *KCl* solution. An alternating voltage signal was applied to the dendrite, which served as the working electrode in this cell. The platinum electrode, which was grounded, served as the counter-electrode in this cell.

6.3. Theory

To describe how both the interfacial and bulk diffusive sub-processes participate in the dendritic reconfiguration process, we propose the following theoretical model. We assume that Schemes (1) and (2) correctly describe the *interfacial* reduction and oxidation processes that occur when the alternating voltage signal reconfigures a dendritic crystal. This assumption will be verified below. To begin, we model the diffusion of $Au^{III}Cl_4^-$

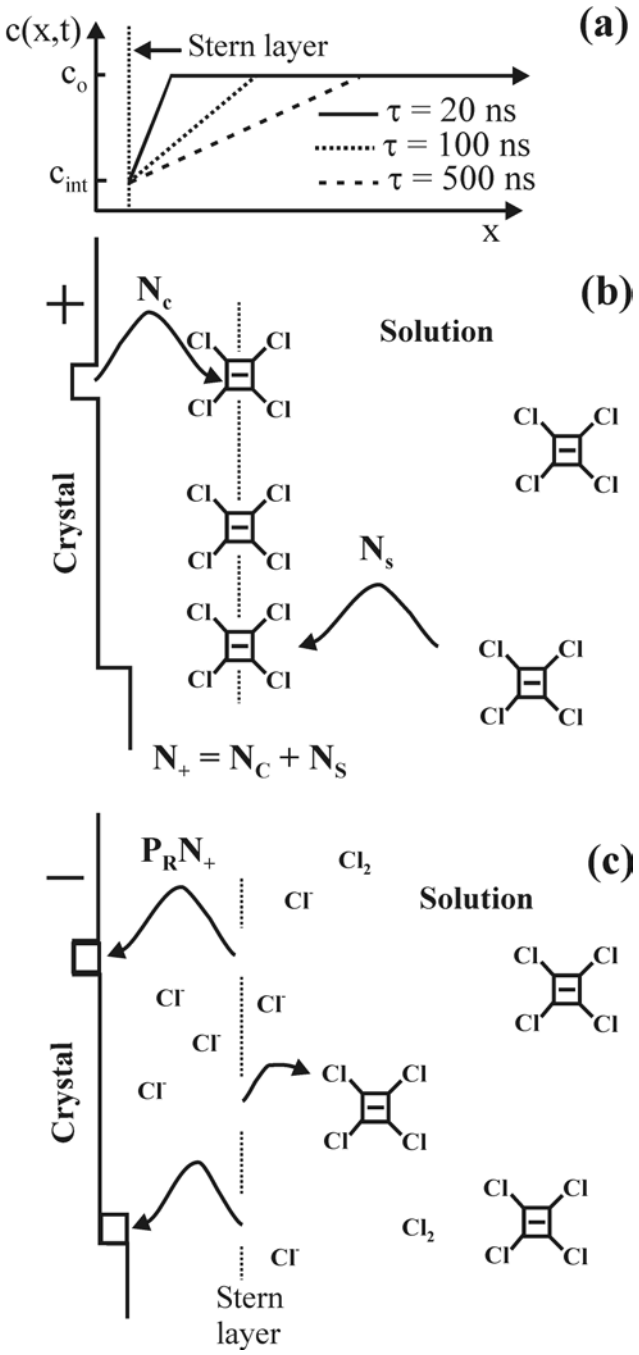

Figure 6.3. (a) Concentration profiles of metallic ions in solution near the crystalline interface after increasing periods of positive bias. (b) Schematic of the spatial distribution of $Au^{III}Cl_4^-$ ions during a positive half cycle. (c) Schematic of the distribution of $Au^{III}Cl_4^-$ ions during the subsequent negative half cycle.

ions (which are the main source of gold that will crystallize) through the bulk solution to the crystal-solution interface. For simplicity, we regard the crystal-solution interface as flat and of constant area A with the gold concentration varying only in the x-direction. Dendritic growth is a diffusion-limited process. The diffusive flux j_D of $Au^{III}Cl_4^-$ toward the interface is:

$$j_D(x,t) = -D\nabla c(x,t) \tag{1}$$

where D is the $Au^{III}Cl_4^-$ diffusion coefficient and $c(x,t)$ is the $Au^{III}Cl_4^-$ concentration at position x in the solution and at time t.

In the DENA process, an alternating square wave voltage is applied to the solidification front. During each positive half cycle, the concentration of metallic ions in solution evolves in time near the solidification front as governed by the diffusion equation and shown elsewhere.[29] We forego explicit solution of the time dependent diffusion equation here and, for simplicity, approximate the concentration profiles during a positive half cycle with the bi-linear functions shown in Figure 6.3(a). During a positive half cycle, $Au^{III}Cl_4^-$ diffuses to the solidification front, giving rise to a depletion zone in the bulk. Essentially, the profiles flatten as time increases and the solution near the interface becomes more heavily depleted of $Au^{III}Cl_4^-$. These profiles in Figure 6.3(a) imply concentration gradients near the interface of the form:

$$\begin{aligned} \nabla c(x,t) &\approx \frac{\Delta c}{\Delta x(t)} \\ &\approx \frac{\Delta c}{\sqrt{2Dt}} \end{aligned} \tag{2}$$

where $\Delta c = c_0 - c_{int}$ [see Figure 6.3(a)]. In the second equality, Δx was equated to the diffusive root mean square displacement.[30]

When the electrode is positively biased, it is hard for the Au^{III} in the ions to be reduced, so the approaching ions build up Stern and Helmholtz layers adjacent to the electrode. Figure 6.3(b) sketches this effect where only the Stern layer is shown, for clarity. Let N_S be the number of $Au^{III}Cl_4^-$ that join the Stern layer via diffusion from the solution during the positive half cycle:

$$\begin{aligned} N_S &= \int_0^\tau j_D(x,t)A dt \\ &= A\Delta c\sqrt{2D\tau} \end{aligned} \tag{3}$$

where τ is the duration of a positive half cycle, and equations (1) and (2) were used to arrive at the second equality.

The positive electrode is able to oxidize $Au^{(0)}$ atoms in the crystal in accordance with Scheme (1). As sketched in Figure 6.3(b), these gold chloride ions also join the Stern and Helmholtz layers near the interface. We take the oxidative flux j_O of $Au^{III}Cl_4^-$ to the interfacial Stern layer to be essentially constant during the positive half cycle, as this flux should not depend (much) on the $Au^{III}Cl_4^-$ concentration in solution (which does change during this period).[31] Therefore, the number N_C of Au^0 that were oxidized during the positive half cycle is simply:

$$N_C = j_0 A\tau \tag{4}$$

Using equations (3) and (4), the total number of ions N_+ that join the Stern Layer during a positive half cycle of duration τ is given by the sum of N_S and N_C:

$$N_+ = A\Delta c\sqrt{2D\tau} + j_O A\tau. \tag{5}$$

Immediately after the voltage switches negative [see Figure 6.3(c)], these N_+ gold chloride ions ($Au^{III}Cl_4^-$) still occupy the Stern layer, but have probability P_R of being reduced

from Au^{III} to Au^{0} via Scheme 2. P_R is significant when the electrode is negative, while the oxidation probability is greatly diminished. The number of Au^{III} that are reduced during this step is $P_R N_+$. When τ is adjusted to the critical value τ_C at which $P_R N_+$ equals $j_O A \tau_C$, the number of Au^{0} that were oxidized during the positive half cycle, the system is in a steady state—there is neither crystallization nor dissolution:

$$P_R\left(\sqrt{2D\tau_C}\Delta c + j_0\tau_C\right) = j_0\tau_C \tag{6}$$

This condition implies an inherent time-scale τ_C for the positive half cycle duration that demarcates the growth and dissolution modes:

$$\tau_C = \frac{2D\Delta c^2}{j_O^2}\frac{P_R^2}{\left(1-P_R\right)^2} \tag{7}$$

The frequency f of the alternating voltage signal (assuming a 50% duty cycle) is $(2\tau)^{-1}$, so the predicted critical frequency f_C above which growth occurs is

$$f_C = \frac{j_0^2}{4D\Delta c^2}\frac{\left(1-P_R\right)^2}{P_R{}^2}. \tag{8}$$

Below this value, dissolution is predicted to occur whereas for frequencies larger than f_C, crystallization is expected.

6.4. Results

The complete structural reconfiguration of a small number of gold dendrites positioned at the tip of a sharp tungsten filament is illustrated in Figures 6.2(a)-(p). This series of images was collected during a continuous *123 s* period when the frequency of the voltage-signal was cycled (two times) between 34.0 MHz and 1.0 MHz. The amplitude and duty cycle were fixed at 4.0 V and 50 %, respectively. The 34.0 MHz signal was initiated at t = 0 s. Panels (a)-(d) depict the

growth of a gold dendrite over the next *44 s*. At $t = 45$ *s*, the frequency was abruptly reduced to 1.0 MHz. Panels (e)-(h) depict the *dissolution* of the gold dendrite over the subsequent *8 s*. Panels (i)-(p) illustrate the next growth-dissolution cycle. We have observed 87 continuous growth-dissolution cycles by using a Labview control-program to cycle the function generator between high and low frequencies (not shown). This process can be automated and repeated a significant number of times. Figure 6.2(q) depicts the square-wave voltage functions used to grow (solid) and dissolve (dashed) the dendrites. Essentially, the growth of gold dendrites is induced by voltage signals of frequency > 10.0 MHz; dissolution is induced by voltage signals of frequency < 3.0 MHz. Neither behavior is observed for frequencies between 3.0 MHz and 10.0 MHz.

Figure 6.4(a) depicts a cyclic voltammagram of a bulk gold sample. As the potential of the bulk gold working electrode ΔV is stepped in the positive direction, the current I into the working electrode grows slightly positive (consistent with electrons flowing into the working electrode) and increases in magnitude with a small slope until $\Delta V \sim 0.80$ V. Beyond this point, the current magnitude increases rapidly in the positive direction as ΔV is stepped further towards 0.90 V. As established elsewhere,[32] this positive current corresponds to the dissolution of solid $Au^{(0)}$ as it is oxidized to $Au^{III}Cl_4^-$ (aq) and $Au^{I}Cl_2^-$ (aq). As ΔV is scanned in the reverse direction, the magnitude of I drops rapidly and flattens out such that little current is measured between 0.8 V and 0.6 V. At ~ 0.6 V, a negative current becomes evident, peaking at 0.55 V. This negative current corresponds to the deposition of $Au^{(0)}$ on the working electrode as $Au^{III}Cl_4^-$ (aq) and possibly also $Au^{I}Cl_2^-$ (aq) are reduced to $Au^{(0)}$.

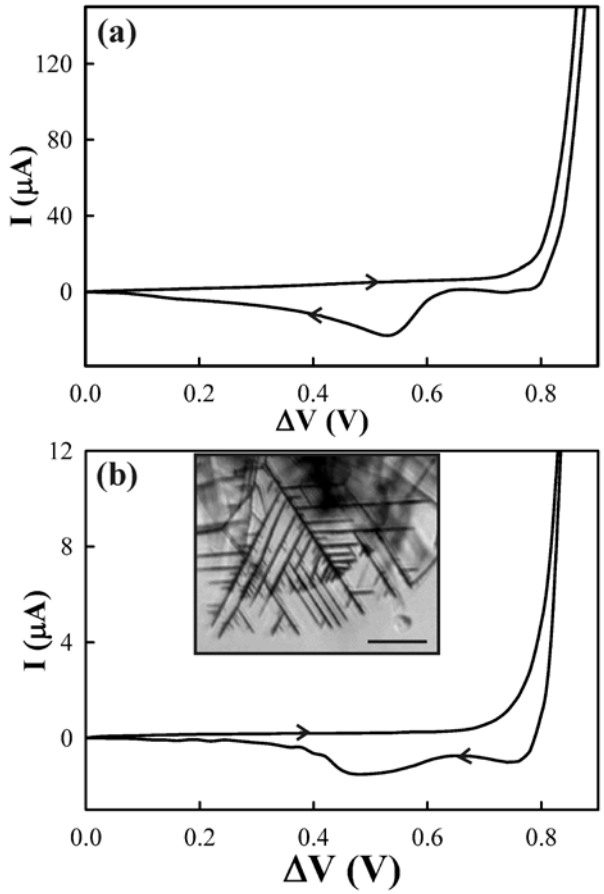

Figure 6.4. (a) Cyclic voltammagrams obtained in 0.1 M KCl with a *bulk* gold working electrode. (b) Cyclic voltammagrams obtained in 0.1 M KCl with a *dendritic* gold working electrode. Scan rate = 25 mVs^{-1}. Inset: Optical image of a gold dendrite. Scale bar = 30 μm. (Sign Convention: a positive (negative) current corresponds to negative (positive) charge flowing into (out of) the working electrode).

Figure 6.4(b) depicts a representative cyclic voltammagram of the gold dendrites shown in the inset. The voltammagram of the dendrite exhibits a forward scan showing a positive current at $\Delta V \sim 0.75$ V that rapidly increases with further voltage-increase; furthermore, this voltammagram exhibits a reverse scan showing a negative current peak at 0.53 V. The voltammagram of bulk gold in figure 6.4(a) shows these same features. This level of agreement

implies that dendritic gold undergoes the same redox chemistry under DC voltages as bulk gold. That is, the positive current at voltages above 0.80 V corresponds to the dissolution of Au from the working electrode (*i.e.* the dendrite), as summarized by Scheme (1); the negative feature at 0.53 V corresponds to the deposition of gold onto the working electrode via the reduction of $Au^{III}Cl_4^-$ (*aq*) and possibly $Au^{I}Cl_2^-$ (*aq*) ions, as summarized by Scheme (2).

It is possible that the redox-chemistry of gold differs when it is induced by MHz-level voltage signals instead of DC voltage signals. Hence, we have employed a Raman microscope to interrogate the surface of single gold dendrites while they are dissolving under alternating voltages. Figure 6.5(a) shows Raman spectra that were collected from a ~0.80 μm^2 region of a gold dendrite that was immersed in 0.1 M KCl solution. When no voltage was applied to the dendrite, a featureless spectrum was obtained (solid line). However, the application of a dissolution-inducing 500 kHz voltage-signal (4.0 V amplitude, 50 % duty cycle) yielded the spectrum with a single peak at 235 cm^{-1} (dotted line). A voltage-signal having a larger, 6.0 V amplitude (but the same frequency and duty cycle) yielded the spectrum with a single peak at 250 cm^{-1} (dashed line); hence, the larger substrate bias induces a 15 cm^{-1} blue-shift of this spectral feature. It is known that the vibrational mode of the adsorbed species $AuCl_{Ad}$ is located between 230 cm^{-1} and 265 cm^{-1} and that it blue-shifts with increasing positive substrate bias.[33, 34] This effect occurs because the applied voltage stiffens the *Au-Cl* bond that forms when a chloride atom binds to a surface gold atom. Substrate bias will not affect a randomly oriented *AuCl* moiety in solution. This information indicates that the 235-250 cm^{-1} feature corresponds to the surface-enhanced Raman detection of $AuCl_{Ad}$ and that the alternating voltage causes the

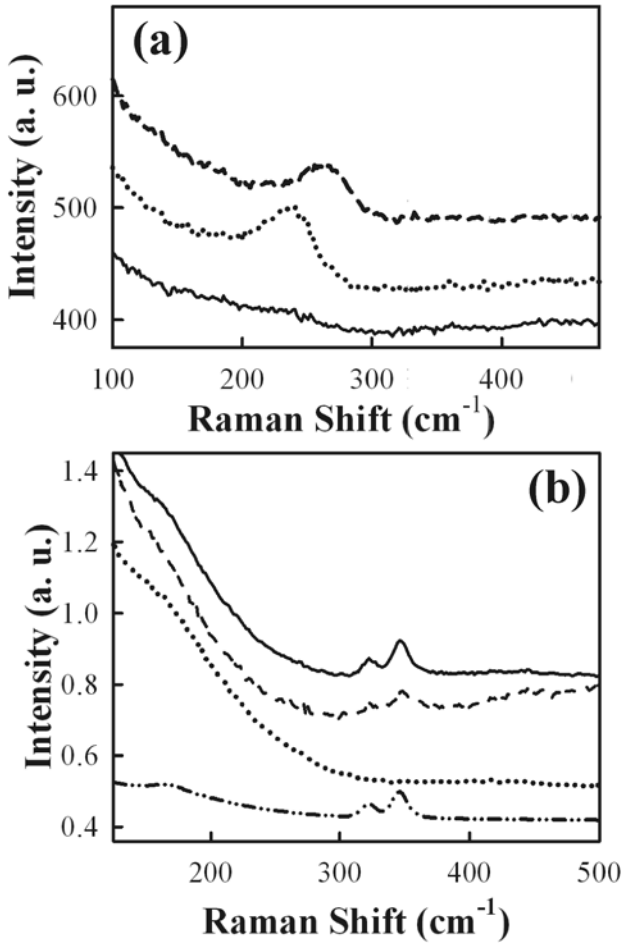

Figure 6.5. (a) Raman spectrum from the surface of gold dendrite in *KCl* solution with the application of no voltage (solid line), 4.0 V, 500 kHz signal (dotted line), and 6.0 V, 500 kHz signal (dashed line). (b) Raman spectrum of 0.1 M KCl solution while dissolving bulk gold by a 4.0 V, 500 kHz signal (solid line); Raman spectrum of 0.1 M KCl solution with application of no voltage to the bulk gold (dotted line); Raman spectrum for gold-chloride complexes obtained from the surface of residue that was formed by evaporating the post-dissolution solution (dashed line); and Raman spectrum of 20.0 mM $HAuCl_4$ solution (dot-dot-dashed line).

formation $AuCl_{Ad}$ on dendritic gold in accordance with step 1(a) of the bulk dissolution mechanism.

Figure 6.5(b) shows Raman spectra that were collected while the microscope was focused ~10 μm to the side of a bulk gold sample. The surrounding solution was 0.1 M *KCl*, which initially contained no detectable level of $Au^{III}Cl_4^-$. When no voltage was applied to the gold, a featureless spectrum was obtained (dotted profile). However, when a 500 kHz voltage-signal (4.0 V amplitude, 50 % duty cycle) was applied, a spectrum with weak shoulder at 173 ± 10 cm^{-1} and peaks at 324 ± 5 cm^{-1} cm^{-1} and 343 ± 5 cm^{-1} was collected (solid profile). These features agree well with the B_{1g} (bend), B_{2g} (asymmetric stretch), and A_{1g} (symmetric stretch) vibrational modes of $Au^{III}Cl_4^-$ (*aq*), respectively, whose spectrum is shown in Figure 6.1(b). The solid profile closely resembles this spectrum. This finding implies that the application of the 500 kHz voltage signal to the gold sample produces $Au^{III}Cl_4^-$ (*aq*) in the region surrounding the sample. Hence, the alternating voltage dissolves gold in accordance with step 1(c) of the established dissolution mechanism. Attempts to observe $Au^{III}Cl_4^-$ (*aq*) near dissolving nano-dendrites were not successful, most likely due to the much smaller quantity of $Au^{III}Cl_4^-$ that dendritic samples produce relative to bulk samples.

The *duty cycle* of the voltage signal was also found to provide control over the reconfiguration process. Figures 6.6(a)-(h) depict one growth-dissolution cycle of this behavior as induced by switching the duty cycle of the voltage signal (4.0 V, 6.0 MHz) from 47 % to 53 % once during the *288 s* observation period. A 6.0 MHz signal was chosen because neither growth nor dissolution is observed when a 6.0 MHz signal with a 50.0 % duty cycle is used, allowing

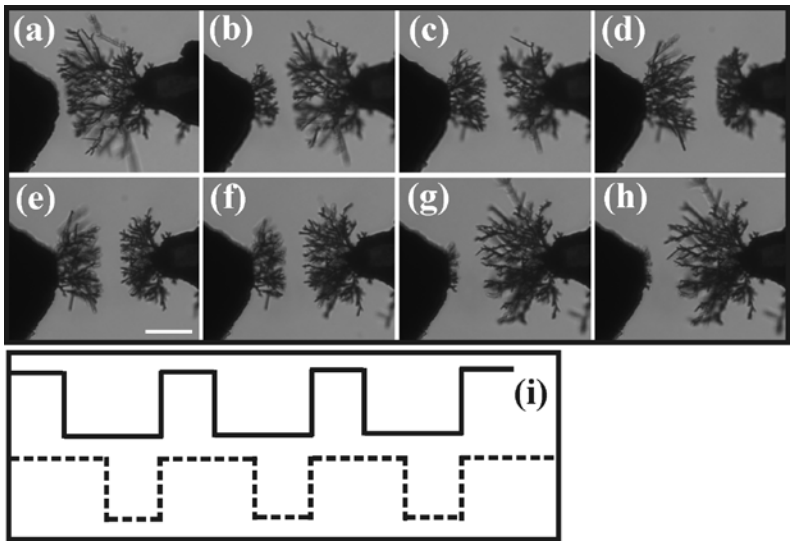

Figure 6.6. Optical micrographs showing growth and dissolution of gold dendrites by cycling the duty cycle of the voltage signal (4.0 V, 6.0 MHz) between 47% and 53%. Panels (a)-(d) depict the dissolution of dendrites at right electrode (biased electrode) as induced by 53% duty cycle. Panels (e)-(h) depict the growth of dendrites at right electrode as induced by the 47% duty cycle. Scale bar = 40 μm.

any deviation from null behavior to be attributed to the duty cycle. The 53.0 % signal was applied to the right electrode at *t = 0 s*. Panels (a)-(d) depict the *dissolution* of the gold dendrites on that electrode over the next *153 s*. At *t = 154 s*, the duty cycle at the right electrode was abruptly reduced to 47.0 %. Panels (e)-(h) depict the *growth* of gold dendrites at the right electrode over the subsequent *134 s*. Because the duty cycle at the left electrode is the complement of that at the right electrode, growth (dissolution) at the left electrode occurs simultaneously with dissolution (growth) at the right electrode. Figure 6.6(i) depicts the square-wave voltage functions used to grow (solid) and dissolve (dashed) the dendrites.

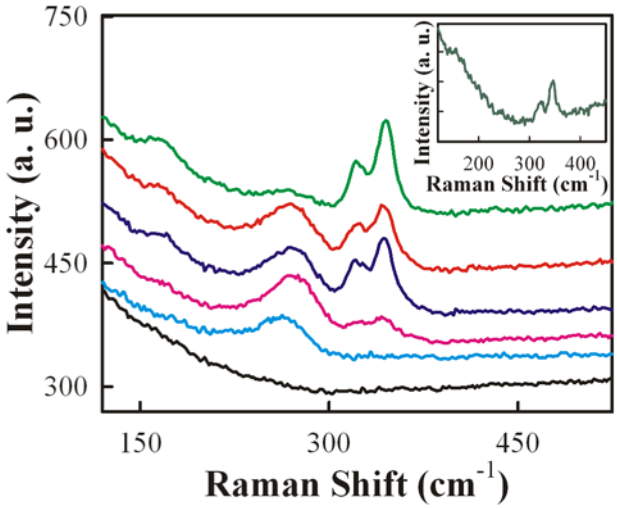

Figure 6.7. Raman spectra from gold surface in 0.1 M KCl solution at 4.0 V, 500 kHz amplitude square signal with 45% duty cycle (black, lowest profile), 50% duty cycle (cyan), 55% duty cycle (pink), 60% duty cycle (blue), 65% duty cycle (red), and 70% duty cycle (green, highest profile). Inset: Raman spectrum of residual solution (dark green) obtained after the duty cycle experiment of 5(a). Indeed, the set of peaks at 173 cm^{-1}, 324 cm^{-1} and 345 cm^{-1} indicate the presence of $AuCl_4^-$.

Figure 6.7(a) shows a series of duty-cycle dependent Raman spectra that were collected while the microscope was focused on the interface between a bulk gold wire and a 0.1 M *KCl* solution. The spectrum collected shortly (~ 5 s) after applying a 45 % voltage signal (500 kHz voltage, 4.0 V amplitude) to the working electrode is featureless (black curve). There is little change on stepping the duty cycle up to 50 % (cyan). However, a peak centered at 265 cm^{-1} appears when the duty cycle is increased to 55 % (pink profile). As discussed above, this feature likely denotes the adsorbate $AuCl_{Ad}$. Also apparent are weak shoulders at 173 cm^{-1}, 324 cm^{-1} and 345 cm^{-1} that denote $Au^{III}Cl_4^-$ (*aq*). As the duty cycle is increased further to 60 %, 65 % and 70 %, the $AuCl_{Ad}$ feature at 265 cm^{-1} diminishes in intensity while the $Au^{III}Cl_4^-$ peaks (at 173 cm^{-1}, 324 cm^{-1} and 345 cm^{-1}) increase in intensity. These trends suggests that increasing the duty

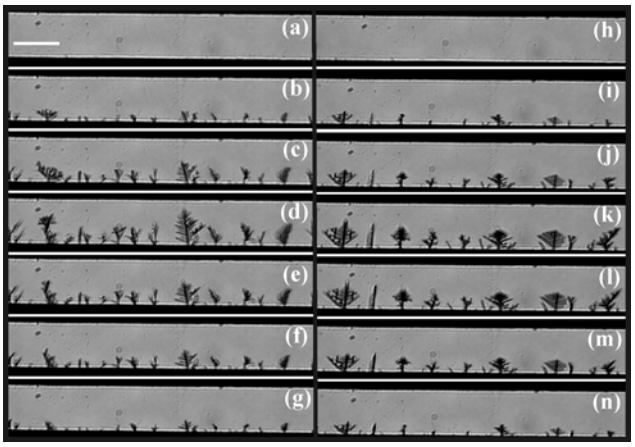

Figure 6.8. Optical micrographs showing growth and dissolution (two cycles) of 1D array of gold dendrites on lithographic substrates that were obtained by twice cycling the frequency between 34.0 MHz and 1.4 MHz. Scale bar = 20 μm. Panels (a)-(d) and (h)-(k) depict the growth stage and panels (e)-(g) and (l)-(n) depict the dissolution stage of the dendrites.

cycle induces the dissolution of solid gold by first reducing Au^0 to the intermediate Au^ICl_{Ad}, in accordance with step 1(a) of scheme 1. Further increase in the duty cycle causes the gold atom in this species to be reduced to the solvated species $Au^{III}Cl_4^-$ (*aq*), in accordance with step 1(b) of scheme (1). The spectrum in the inset was collected from the solution after performing this study, at which point, the solution was faintly yellow, consistent with the presence of $Au^{III}Cl_4^-$ (*aq*).

It is also possible to produce and reconfigure entire arrays of dendrites that coat electrode surfaces. Figure 6.8 is a series of images depicting the simultaneous reconfiguration of a dozen roughly evenly spaced dendrites that are positioned along a straight 1D lithographic electrode. The horizontal field-of-view in each image is 100 μm. Panels (a)-(d) illustrate the growth of these dendrites over a *12 s* period, as induced by a voltage-signal (8.0 V, 34 MHz, 50 % duty cycle) applied to the (lower) working electrode while grounding the (upper) counter-electrode.

Panels (e)-(h) depict the complete dissolution of these dendrites over the following 7 s, as induced by reducing the frequency to 1.4 MHz. Panels (i)-(n) illustrate the subsequent reconfiguration cycle. While the shapes of the individual dendrites differ, their growth and dissolution rates are essentially uniform: at a given time (*i.e.* panel), the dendrites have common heights. This 1D forest of dendrites extends along the entire 0.225 mm length of the immersed electrode (not shown).

6.5. Discussion

Causing dissolution of a crystal is the key step that makes dendritic crystallization a reconfigurable process. This paper shows that changes in the MHz-level frequencies of voltages that are applied to the dendrites induce their dissolution. To better understand how this process occurs, we have characterized the redox chemistry of the crystal-solution interface during dissolution. Close similarity between the cyclic voltammagrams of bulk and dendritic gold [Figures 6.4(a) and (b), respectively] imply that both materials grow and dissolve *under DC voltages* via the same chemical steps (Schemes 1 and 2). To interrogate the reconfiguration chemistry *under alternating voltages*, we have employed Raman microscopy. These studies have established that the adsorbate $AuCl_{Ad}$ forms on the dendrite-surface when < 3.0 MHz voltage signals, which induce dissolution, are applied to the dendrite [Figure 6.5(a)]. This finding is in agreement with step 1(a) of the bulk dissolution mechanism (Scheme 1). We have also observed a Raman signal indicating that $Au^{III}Cl_4^-$ (*aq*) is produced when this voltage is applied to the gold samples. This finding is in accordance with step 1(c) of the bulk dissolution mechanism. Structural reconfiguration of dendritic gold is also induced by changes in the duty cycle of the voltage-signals that are applied to the dendrites. As discussed above, increasing

(decreasing) the duty cycle to values greater (less) than 50.0 % causes the dendrite to dissolve (grow) [Figure 6.6(a)-(h)]. Raman analysis indicates that scheme (1) accurately describes how dissolution occurs when duty cycles > 50.0 % are applied [Figure 6.7]. Taken together, these observations indicate that the same dissolution mechanism that occurs under DC voltages (and which is well understood) provides an accurate description of the dissolution portion of the dendrite reconfiguration mechanism.

This analysis provides confidence that Schemes (1) and (2) accurately describe the *interfacial* atom-joining and atom-leaving processes that occurs during dendritic reconfiguration and, thereby, validates our use of these schemes in the theoretical formulation presented above. This theory predicts a critical frequency f_C [equation (8)] for the alternating voltage, above which there is growth and below which there is dissolution. We use the following values in equation (8) in order to compute the critical frequency. An estimate for the diffusivity D is calculated via application of the Stokes-Einstein relation to an $Au^{III}Cl_4^-$ ion of radius $a \sim 4.5 \times 10^{-10}$ m in aqueous solution of viscosity 1×10^{-3} kg m^{-1} s^{-1} having thermal energy $k_BT \sim 4.1 \times 10^{-21}$ J: $D \sim k_BT/(6\pi\eta a) = 4.8 \times 10^{-10}$ m s^{-2}; if we assume that the interfacial concentration of $Au^{III}Cl_4^-$ is ~½ the bulk concentration of 20 mM, then $\Delta c \sim 10$ mM $= 0.5 \times 10^{25}$ m^{-3}. An estimate for oxidative flux j_O is obtained through the observation that a typical gold dendrite of number density $\rho \sim 6 \times 10^{28}$ m^{-3} dissolves at a rate of $v_D \sim 5$ μm s^{-1}; thus $j_O \sim \rho v_D = 3.0 \times 10^{23}$ m^{-2} s^{-1}. The reduction probability during the negative half cycle (P_R) must lie between 0 and 1. Here, we assume a value of $P_R \sim 0.5$. This number seems reasonable as P_R is expected to be significant due to the availability of electrons on the negative dendrite (with which to reduce $Au^{III}Cl_4^-$), but should not be as high as unity due to electrostatic repulsion between the electrode and $Au^{III}Cl_4^-$. Substitution

of these values into (8) yields f_C ~ 1.8 MHz. Experimentally, we observe the critical frequency to be ~ 3.0 MHz, so prediction and observation are in reasonable agreement. Qualitative agreement is all that should be expected of this theory, given its approximate treatment of the diffusion equation. Nevertheless, this approach addresses the effects of both the interfacial chemistry and the bulk diffusion of $Au^{III}Cl_4^-$ to illustrate how imbalance between the interfacial and diffusive rates causes either growth or dissolution of dendritic crystals.

This theory also provides an explanation for why variation of the duty cycle induces reconfiguration. Increasing the duty cycle lengthens the duration that the dendrite is positively biased relative to its duration of negative bias. According to the theory, such a change will enhance the extent of dissolution during a complete voltage cycle and reduce the extent of reduction (*i.e.* deposition); hence, dendrites are expected to dissolve under duty cycles > 50.0 %, as observed. Conversely, reducing the duty cycle shortens the duration that the dendrite is positively biased. This change will retard the extent of dissolution during a compete cycle and enhance the extent of deposition. Hence, dendrites are expected to grow when the duty cycle is less than 50.0 %, as observed.

As an extension of the basic reconfiguration-process that *individual* dendrites exhibit, we have demonstrated the reconfiguration of *macroscopic arrays* of dendrites. Figure 6.8 illustrates the on-command growth and dissolution of 1D forests of dendrites that extend along the entire (0.25 mm) length of an immersed electrode. In future work, we envision extending this capability to produce regenerative 2D dendritic arrays.

6.6. Conclusions

This work presents an electrochemical method for inducing the complete structural reconfiguration of metallic nano-dendrites. Essentially, we cause a dendrite, or an array of dendrites, to grow, dissolve, and grow again in an on-command and repeatable manner. Our observations strongly suggest that the alternating voltages used in the DENA technique cause gold nano-dendrites to grow and dissolve by the same reduction and oxidation mechanisms that bulk gold samples exhibit under DC voltages. A simple theoretical model that accounts for both of these interfacial chemical processes as well as the bulk diffusion of $Au^{III}Cl_4^-$ through the solution succeeds, at least on a semi-quantitative-level, in describing how the dendritic reconfiguration mechanism works. Essentially, the frequency and the duty cycle of the alternating voltage signal control the imbalance between interfacial and diffusive processes to cause either growth or dissolution of dendritic crystals.

A goal for the near future will be to produce fully reconfigurable 2D dendritic arrays. We expect this to be readily achievable as an example of a 2D dendritic array has already been reported.[35] Such a step would provide an innovative way to coat surfaces with nano-structured dendrites in a reconfigurable manner. DENA provides control over both the overall size and the branch-diameter[29] of a dendrite, thereby providing both micro- and nanoscale control; hence, 2D arrays of such structures hold promise as surface modifications that provide reconfigurable or self-healing wettability and adhesion control of the Baxter-Cassie type.[36, 37] As a reasonably wide range of metals undergoes dendritic solidification—not just gold, new strategies for anodic protection of metallic surfaces immersed in corrosive environments, such as seawater, become possible. One example is the deposition of 2D forests of Mg or Zn dendrites onto immersed

surfaces in order to serve as rechargeable sacrificial anodes that would be inexpensive and widely available. Finally, given that the plasmonic resonances of the nano-dendrites will alter the color and specular reflectance of a surface that is coated with such an array, variation of the optical properties of the surface may also be achieved.

6.7. Acknowledgements

This work was partially supported by National Science Foundation grants PHY-0646966, ECCS-0601362, EAR-0722410. We thank Professor Larry Weaver for countless offerings of insightful theoretical assistance.

6.8. References

1. L. Wang, L. Xu, H. Kuang, C. Xu and N. A. Kotov, *Acc. Chem. Res.*, 2012, **45**, 1916-1926.
2. R. Hanlon, *Curr. Biol.*, 2007, **17**, R400-R404.
3. B. Brown and S. Gibb, *Journal of Experimental Marine Biology and Ecology*, 2002, **277**, 129-144.
4. T. Z. Grove, C. O. Osuji, J. D. Forster, E. R. Dufresne and L. Regan, *J. Am. Chem. Soc.*, 2010, **132**, 14024-14026.
5. S. Sacanna, L. Rossi and D. J. Pine, *J. Am. Chem. Soc.*, 2012, **134**, 6112-6115.
6. W. H. Hilbertz, *IEEE J. Oceanic Engineering*, 1979, **OE-4**, 94-113.
7. A. Neville and A. P. Morizot, *J. Crystal Growth*, 2002, **243**, 490-502.
8. M. H. Lee, K. M. Moon, J. D. Kim, K. Jun and K. H. Kim, *Trans. Nonferrous met. Soc. China*, 2009, **19**, s110-s113.
9. B. N. Flanders, *Mod. Phys. Lett. B*, 2012, **26**, 1130001.
10. G. E. Nash and M. E. Glicksman, *Acta Metall.*, 1974, **22**, 1291.
11. S. C. Huang and M. E. Glicksman, *Acta Metall.*, 1981, **29**, 701-715.
12. S. C. Huang and M. E. Glicksman, *Acta Metall.*, 1981, **29**, 717-734.
13. J. S. Langer, *Rev. Mod. Phys.*, 1980, **52**, 1-28.
14. D. A. Kessler, J. Koplik and H. Levine, *Adv. Phys.*, 1988, **37**, 255-339.
15. K. Libbrecht, *Field Guide to Snowflakes*, Voyageur Press, St. Paul, 2006.
16. G. P. Ivantsov, *Dokl. Akad. Nauk USSR*, 1947, **58**, 567.
17. Y. Saito, *Statistical Physics of Crystal Growth*, World Scientific, River Edge, 1996.
18. W. W. Mullins and R. F. Sekerka, *J. Appl. Phys.*, 1964, **35**, 444-451.

19. Y. Saito, G. Goldbeck-Wood and H. Müller-Krumbhaar, *Phys. Rev. Lett.*, 1987, **58**, 1541-1543.
20. I. Talukdar, B. Ozturk, T. D. Mishima and B. N. Flanders, *Appl. Phys. Lett.*, 2006, **88**, 221907.
21. B. Ozturk, T. Mishima, D. R. Grischkowsky and B. N. Flanders, *Nanotechnology*, 2007, **18**, 175707.
22. J. K. Kawasaki and C. B. Arnold, *Nano Lett.*, 2011, **11**, 781-785.
23. M. A. Diaz, G. H. Kelsall and N. J. Welham, *Journal of Electroanalytical Chemistry*, 1993, **361**, 25-38.
24. Y. Qiao, J. Chen, X. Guo, D.cantrell, R. Ruoff and J. Troy, *Nanotechnology*, 2005, **16**, 1598-1602.
25. G. Paneru, P. S. Thapa, S. P. Mcbride, A. Ramm, B. M. Law and B. N. Flanders, *Nanotechnology*, 2012, **23**, 455105.
26. B. H. Loo, *J. Phys. Chem.*, 1982, **86**, 433-437.
27. P. S. Thapa, B. J. Ackerson, D. R. Grischkowsky and B. N. Flanders, *Nanotechnology*, 2009, **20**, 235307.
28. A. J. Bard and L. R. Faulkner, *Electrochemical Methods: Fundamentals and Applications*, John Wiley & Sons, New York, 1980.
29. B. Ozturk, I. Talukdar and B. N. Flanders, *Nanotechnology*, 2007, **18**, 365302.
30. N. Ibl, *Surface Tech.*, 1980, **10**, 81-104.
31. S. K. Ma, *Statistical Mechanics*, World Scientific, Philadelphia, 1985.
32. J. Herrera-Gallego, C. E. Castellano, A. J. Calandra and A. J. Arvia, 1976.
33. B. M. Abraham, K. Miyano, J. B. Ketterson and S. Q. Xu, *Phys. Rev. Lett.*, 1983, **51**, 1975-1978.
34. P. Gao and M. J. Weaver, *J. Phys. Chem.*, 1986, **90**, 4057-4063.
35. K. M. Watling and G. A. Hope, in *International Conference on Nanoscience and Nanotechnology*, IEEE, Brisbane, Austrailia, 2006, pp. 198-201.
36. K. Liu, X. Yao and L. Jiang, *Chem. Soc. Rev.*, 2010, **39**, 3240-3255.
37. A. B. D. Cassie and S. Baxter, *Trans. Faraday Soc.*, 1944, 40, 546-551.

Chapter 7 - Conclusions and future directions

7.1. Conclusions

We have presented a systematic study of nano-fabrication of cellular force sensors for probing sub-cellular targets at the single cellular level and of surface coatings for corrosion and bio-fouling control. The primary nano-fabrication approach is a technique called *directed nanowire assembly* (DENA). The cellular force sensors are composed of PEDOT fibers. PEDOT was chosen due to its biocompatibility. The length and the diameter of a fiber are user controlled during the growth process, and consequently, its spring constant lies in a range that is comparable to the stiffness of the cell. These fibers were calibrated directly by atomic force microscopy (AFM) and by measuring their transverse resonance frequencies by resonance vibration method. The spring constants of the fibers measured via resonance vibration method are in agreement with those measured directly via AFM. In comparison to the AFM method, the calibration of fibers via resonance vibration method is less laborious and cost efficient. Furthermore, the determination of spring constant of a fiber by AFM method requires that the spring constant of the AFM cantilever be comparable to that of the fiber. To the best of our knowledge, the softest commercially available AFM cantilevers have spring constant ~ 6 nN/μm (Olympus, BL-RC-150VB). So, AFM method would not be convenient to calibrate a PEDOT fiber that has spring constant equal to 0.07 nN/μm [see fiber 24 in Table 4.1 of chapter 4] as measured by resonance vibration method.

The *D. discoideum* cells were chosen for our study because of the availability of such cells with different mutant strains. Researchers have developed mutant strains of *D. discoideum* cells that lack all except one of the adhesion molecules involved in cell-substrate adhesion.

Availability of such mutant cells would simplify the composition of the actin foci and as a result this would allow the quantification of potential energy surface for a single type of adhesive molecule. Also, the migration mechanism of a number of higher eukaryotes like neutrophils, T-cells, lymphocytes, and metastatic breast tumor cells is similar to early developmental *D. discoideum* cells. Thus, understanding adhesion and migration mechanism of *D. discoideum* cells is a logical step towards understanding and controlling migration in higher eukaryotes.

The PEDOT fibers fabricated at the tips of movable electrode are capable of probing the sub-cellular target of a cell without forming unintentional secondary contacts to the cell. These fibers were employed to measure the strength and lifetime of individual adhesive contacts of *D. discoideum* cells. The average terminal force between the apical pseudopod and fiber was found to be 3.1 ± 2.7 nN, and average lifetime of the contact was found to be 23.4 ± 18.5 s.

We have also demonstrated methodology for inducing the complete dissolution of an array of metallic dendrites following their growth. The experimental parameters that control this process are the frequency or duty cycle of the applied voltage signal. Cyclic voltammetric and Raman measurements suggest that the alternating voltages used in the DENA technique cause gold nano-dendrites to grow and dissolve by the same reduction and oxidation mechanisms that bulk gold samples exhibit under DC voltages. We have presented a simple theoretical model that explains how both bulk diffusion as well as interfacial chemical processes of metallic salts through the solution controls the dendritic reconfiguration mechanism. This theory also predicts that the frequency and the duty cycle of the alternating voltage signal controls the imbalance between interfacial and diffusive processes to cause either growth or dissolution of dendrites.

7.2. Future directions

7.2.1. Planned cellular adhesion measurements

In chapter 2, we have presented a theoretical model for the rupture of adhesion clusters in actin foci by pulling force. This theory explains how the contact ruptures in an outside-in manner. After an initial period during which the applied force ruptures the large number of outer bonds in the contact, this force becomes concentrated on the relatively few remaining inner bonds, at which point the contact ruptures rapidly. In addition to the density of receptors-substrate bond Γ and the cell-medium surface tension γ, this theory requires knowledge of two parameters that describes the potential energy surface for a single R-S bond: the molecular distance z_β that the receptor needs to move to break the bond, and the unstressed off-rate k_0. In future work, we will employ our innovative force sensors to determine z_β and k_0 for the R-S bonds in actin foci. Our undertaking to achieve this goal is based on the analysis of receptor-ligand physics via *dynamic force spectroscopy*.[1] By employing a sensitive force probe to pull on individual receptor-ligand pairs with a linearly increasing applied force, the technique measures k_0 and z_β of the potential energy surface for a single receptor-ligand bond.[2] The most frequent rupture force f^* depends on the loading rate m as follows:[2]

$$f^* = -f_\beta \ln k_0 f_\beta + f_\beta \ln m \qquad (1)$$

Hence, f^* vs ln$m$ plot will exhibit a linear regime of slope f_β (where $z_\beta = kT/f_\beta$). The y-intercept determines k_0.

Dynamic force spectroscopy has also been applied to *multiple* parallel bonds.[3-5] For this, the relationship between the rupture force F^* (applied to whole cluster), k_0 and f_β is not as simple

as (1) although the rupture force F^* still varies linearly with the log of the loading rate ln$m$.[4, 5] Experimentally, the single molecule and cluster approaches are conceptually similar: measurement of distributions of rupture forces and distributions of contact times. However, in order to extract k_0 and z_β, one needs a complete theoretical model for how the cluster de-adheres. Though challenging, this procedure is still tractable and will be done in a future effort.

As a step towards our future goal, we have measured the preliminary rupture force distributions at single adhesive contact sites of *D. discoideum* cells. Figure 7.2 shows the distribution of rupture force for average loading rates of 2.0 nNs^{-1} (patterned vertical bars) and 4.0 nNs^{-1} (non-patterned vertical bars), constructed from 62 and 32 events, respectively. This graph shows that on increasing the loading rate from 2.0 nNs^{-1} to 4.0 nNs^{-1}, the strength of most frequent rupture force F^* increases from 2.29 nN to 5.50 nN and the distributions broaden across this loading rate range. These preliminary observations are consistent with prior observations of multiple parallel bonds that dissociates stochastically under a shared linear force.[4-6] In future work, we will measure a statistically significant ensemble of F^* values for a given loading rate, and repeat this procedure for several loading rates.

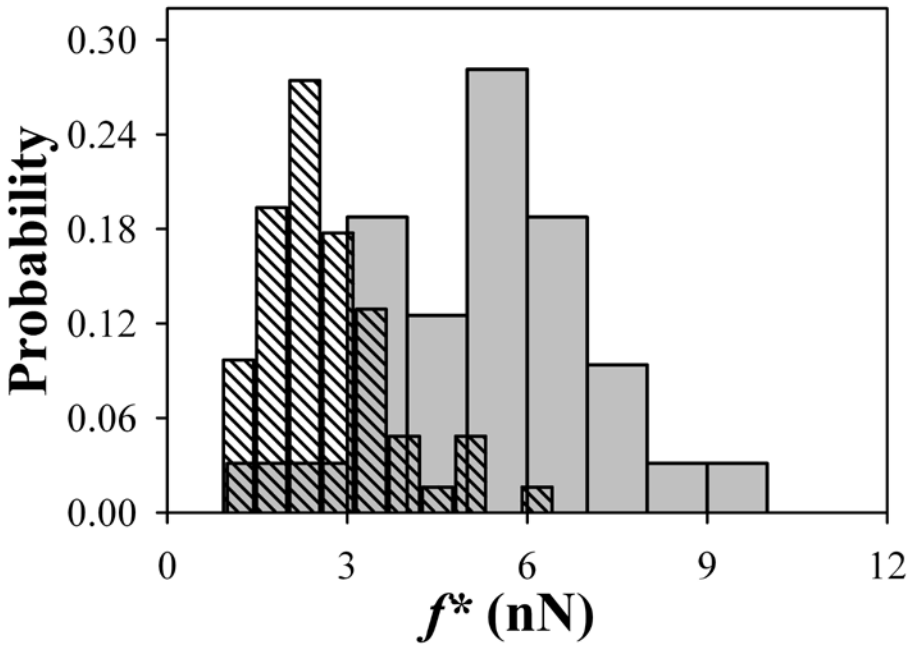

Figure 7.1. Rupture force distributions for loading rates of 2.0 nN/s (patterned bars) and 4.0 nN/s (non-patterned bars).

The cell medium surface tension γ is determined as follows: In roughly 10% of cases when we back-translate the fiber to apply force to an actin focus, we cause the cell to tether. A tether is a tube of cellular membrane that is pulled out of the main region of the cell (Figure 7.2). One forms when the membrane is locally detached from the cytoskeleton and the pulling force exceeds the resistance posed by the bending modulus κ and the surface tension γ of the membrane. The critical tethering force is $F_C = 2\pi(2\kappa\gamma)^{1/2}$.[7] Over 25 events, we have observed a mean critical force of 2.2 ± 0.4 nN. Sackmann and co-workers have measured the bending modulus of wild-type D. discoideum to be 390 kT.[8] Hence, we obtain a determination of $\gamma \sim 43$

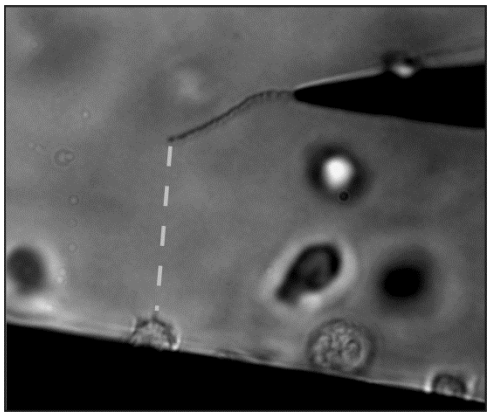

Figure 7.2. Cellular tethering. The tether, which has weak contrast due to its sub-50 nm diameter, is indicated by the dashed line. Scale bar = 10 mm.

mN m^{-1} for the cell-medium surface tension. In future work, we will use our force transducer to measure a statistically significant numbers of critical tethering forces to accurately determine the cell-medium surface tension.

7.2.2. Hypothesis to be tested

The adhesion energy of wild-type *D. discoideum* cells (on glass) is ~ 20 μJ m^{-2}.[8] The actin foci of *D. discoideum* express a variety of cell-substrate adhesion molecules. These molecules include *sibA-E*,[9, 10] *sadA*.[11-13] Recent evidence suggests that this adhesion energy is primarily due to *sadA*-substrate and to lesser extents *sibA*- and *sibC*-substrate attractions. If this hypothesis is true, then generic *sadA*-substrate attractions must be strong enough to produce a sizeable fraction of the adhesion energy observed in wild type cells: ~20 μJ m^{-2}. This appears to be feasible. The 9-pass structure of *sadA* in a cell membrane, reported elsewhere,[12] is sketched in Figure 7.3 (a). As this figure illustrates, we estimate that roughly half the length of a

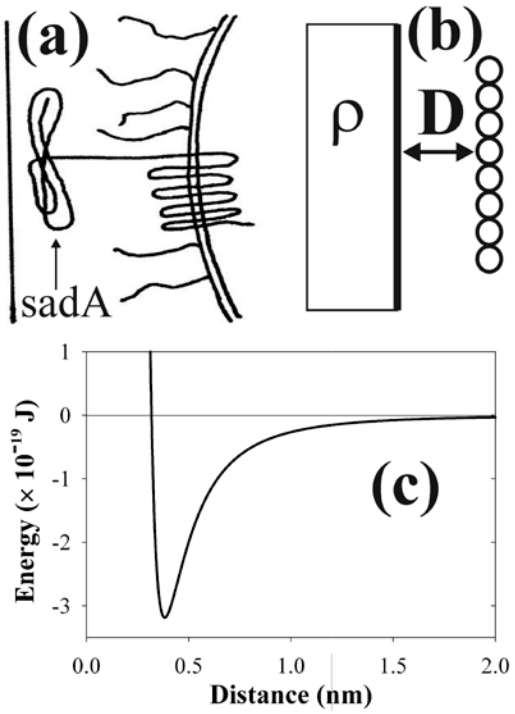

Figure 7.3. (a) Sketch of *sadA* in the cell membrane and adjacent ot the substrate. (b) Geometry for van der Waals attraction between the amino acid chain a distance D from a substrate of density ρ. (c) van der Waals potential well between amino acid chain and glass surface.

sadA molecule (total length= 952 amino acids) extends far enough beyond the glycocalyx to contact an adjacent substrate. Thus, the amino acid chain can interact with the substrate via van der Waals attraction [as depicted in Figure 7.3(b)]. We estimate the corresponding potential energy between a chain of 465 amino acids and a flat surface to be:

$$U = -(465\,\text{amino acids})\frac{\pi C \rho_{glass}}{6D^3} + \frac{0.28\times 10^{-103}\ \text{Jm}^9}{D^9}, \qquad (2)$$

where C is $5\times10^{-78}\ \text{J m}^6$ (typical for hydrocarbons)[14] and the density of glass is $\rho_{glass} = 2.2\times10^{28}\ \text{m}^{-3}$. This function is plotted in Figure 7.3(c). Notably, the well-depth ε is $3.1\times10^{-19}\ \text{J}$. This finding implies two things. First, such contacts would take a very long time to spontaneously rupture, so a cell would have to internally pull on the adhesions with its actin

skeleton (as cells are known to do) in order to accelerate their decay and release the substrate. Second, the adhesion of a cluster of receptors relates in a simple manner to the R-S potential energy well [Figure 7.1(d)]: $G_{Ad} = \Gamma\varepsilon$, where Γ is the R-S density and ε is the well-depth. Assuming a relatively modest receptor-density of 16 μm^{-2} yields adhesion energy of *Gad* ~ 5 $\mu J\ m^{-2}$. Indeed, this value is a sizeable fraction of 20 $\mu J\ m^{-2}$. This analysis demonstrates that *generic* receptor substrate interactions may indeed be strong enough to reproduce the observable adhesive properties. Hence, it is at least feasible that actin foci adhesion occurs via the receptor-substrates interaction. Therefore, this hypothesis needs further investigation. In future work, we will use our force transducer to perform dynamic force spectroscopy on *D. discoideum* cells with *sibA*$^-$, *sibC*$^-$ double-null mutant which lacks the adhesion proteins *sibA* and *sibC* but has *sadA*.

7.3. References

1. R. Merkel, P. Nassoy, A. Leung, K. Ritchie and E. Evans, *Nature*, 1999, **397**, 50-53.
2. E. Evans, *Faraday Discuss.*, 1998, **111**, 1-16.
3. T. Sulchek, R. W. Friddle and A. Noy, *Biophys. J.*, 2006, **90**, 4686-4691.
4. K. Prechtel, A. R. Bausch, V. Marchi-Artzner, M. Kantlehner, H. Kessler and R. Merkel, *Physical Review Letters*, 2002, **89**, 028101.
5. J. W. Swan, M. M. Shindel and E. M. Furst, *Physical Review Letters*, 2012, **109**, 198302.
6. T. Erdmann, S. Pierrat, P. Nassoy and U. S. Schwarz, *Epl*, 2008, **81**, 6.
7. N. Borghi, O. Rossier and F. Brochard-Wyart, *Europhysics Letters*, 2003, **64**, 837.
8. R. Simson, E. Wallraff, J. Faix, J. Niewohner, G. Gerisch and E. Sackmann, *Biophysical Journal*, 1998, **74**, 514-522.
9. S. Cornillon, L. Gebbie, M. Benghezal, P. Nair, S. Keller, B. Wehrle-Haller, S. J. Charette, F. Bruckert, F. Letourneur and P. Cosson, *EMBO Reports*, 2006, **7**, 617-621.
10. S. Cornillon, R. Froquet and P. Cosson, *Eukaryotic Cell*, 2008, **7**, 1600-1605.
11. A. S. Kowal and R. L. Chisholm, *Eukaryotic Cell*, 2011, **10**, 662-671.
12. P. Fey, S. Stephens, M. A. Titus and R. L. Chisholm, *J. Cell. Biol.*, 2002, **159**, 1109-1119.
13. N. P. Barry and M. S. Bretscher, *Proc. Natl. Acad. Sci.*, 2010, **107**, 11376-11380.
14. J. Israelachvili, *Intermolecular & Surface Forces*, Academic Press, London, 1992.

Appendix A - Forces at individual pseudopod-filament adhesive contacts

Forces at individual pseudopod-filament adhesive contacts

Govind Paneru,[1] Prem S. Thapa,[1] Sean P. McBride,[1] David Moore-Nichols,[2] Bruce M. Law,[1] and Bret N. Flanders[1,a)]
[1]*Department of Physics, Kansas State University, Manhattan, Kansas 66506-2601, USA*
[2]*Imaging and Analytical Microscopy Lab, University of Kansas, Lawrence, Kansas 66045, USA*

(Received 1 June 2011; accepted 28 July 2011; published online 2 September 2011)

On-chip cellular force sensors are fabricated from cantilever poly(3,4-ethylene dioxythiophene) filaments that visibly deflect under forces exerted at individual pseudopod-filament adhesive contacts. The shape of the deflected filaments and their ~3 nN/μm spring constants are predicted by cantilever rod theory. Pulling forces exerted by *Dictyostelium discoideum* cells at these contacts are observed to reach ~20 nN without breaking the contact. © *2011 American Institute of Physics*. [doi:10.1063/1.3628454]

The forces that cells exert on substrates at adhesive contacts are critical to basic processes such as migration and cell division. Pseudopods are exploratory appendages that crawling cells like *Dictyostelium discoideum*, leukocytes,[1] and breast cancer cells[2] extend to probe the anterior substrate surface. Adhesive contact between the tips of the pseudopods and the substrate occurs frequently. These are the first contacts that the cell makes with the anterior substrate region. In addition to force-application, environmental sensing occurs at these contact sites, influencing whether the cell alters or persists in its direction-of-migration.[3] Despite the importance of pseudopod-substrate adhesive contacts in force transmission and environmental sensing, there has been little characterization of pseudopod-substrate adhesion at the single contact-level.

The most widely used technique for characterizing cellular forces is the deformable substrate method where cell-induced wrinkling or marker-displacement of the elastic substrate is observed.[4] A key advantage of this approach is that the substrate displacements occur in the imaging plane of the optical microscope, permitting direct visualization of the process. However, the forces at the discrete adhesive contact sites are not directly measured but are instead extracted by a non-trivial modeling effort that correlates the measured substrate displacement-field with the inferred force field and with the discrete sites.[5] Off-substrate forces may be directly measured with an atomic force microscope (AFM) with exquisite precision[6]; however, visualization during such measurements, which are usually made in a plane normal to the optical imaging plane, can be a challenge. Methodology for the simultaneous visualization and direct characterization of forces exerted by individual pseudopodia is needed.

To this end, we have fabricated on-chip cantilever poly(3,4-ethylene dioxythiophene) (PEDOT) filaments that visibly deflect under forces exerted at individual pseudopod-filament contacts. PEDOT was chosen for its biocompatibility.[7] A typical 3.2 μm long, ~400 nm wide pseudopod is indicated by the arrow in Figure 1(a). Direct characterization of an individual pseudopod requires a probe of comparable dimension. To produce such filaments, the simple polymerization technique *directed electrochemical nanowire assembly* (DENA) was employed.[8] Briefly, a 3 μl aliquot of aqueous solution containing 0.01 M 3,4-ethylene dioxythiophene and 0.02 M poly(sodium styrene sulfonate) was deposited across the ~30 μm gap between a pair of tapered, lithographic Au electrodes. The filament in Figure 1(b) was produced by applying a ±3.5 V 20 kHz square wave voltage signal across the electrodes to induce filament growth from the right electrode at a rate of ~5 μm/s. The voltage signal was terminated when the filament reached the desired length of ~14 μm. The scanning electron microscopy (SEM) based image in the inset shows its lengthwise-averaged width to be 320 ± 30 nm. Comparison to Figure 1(a) shows filament and pseudopod widths to be comparable, as desired. These filaments are rigidly bonded to the on-chip electrode but not to the glass substrate and, hence, are cantilever structures.

Type KAx3 *D. discoideum* cells were grown at 24 °C in Petri dishes containing HL-5 culturing medium.[9] Prior to transfer to the chips, 1000 μl of the cell-medium suspension was centrifuged for ~10 s at 1.34×10^3 g. The HL-5 supernatant was replaced with 1000 μl of 12 mM phosphate buffer, followed by gentle shaking for 1 min. This process was twice-repeated before suspending the cells in 300 μl of phosphate buffer and starving them for 4-6 h. To prevent evaporation of the cell medium, a 60 μl hybridization chamber (Grace Biolabs) was adhered to the filament-laden chip. Before sealing with a transparent lid, 10 μl volumes of cell suspension and phosphate buffer were deposited in the chamber. Typical cell surface densities were ~10^3 mm^{-2}. A waiting time of ~20 min following cell deposition was required for the cells to settle, to begin migrating, and for a single cell to randomly contact the filament.

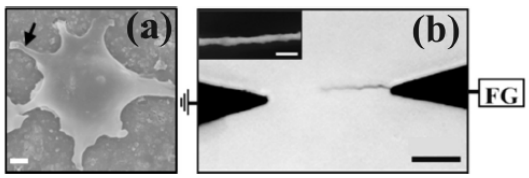

FIG. 1. (a) Scanning electron micrograph of fixed *D. discoideum* cell with extending pseudopods. Scale bar = 1 μm. (b) Optical micrograph of PEDOT filament grown by the DENA technique. FG ≡ function generator. Scale bar = 10 μm. Inset: a scanning electron micrograph of a filament. Scale bar = 1 μm.

a)Electronic mail: bret.flanders@phys.ksu.edu.

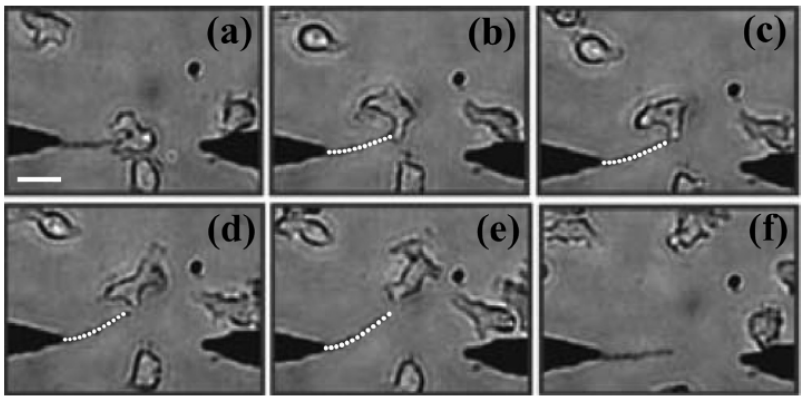

FIG. 2. Series of optical micrographs of a cantilever PEDOT filament (a) in its neutral position 7 s after contact initiation by the pseudopod. Scale bar = 10 μm; (b)-(e) while being deflected upwards by the cell at times 37 s, 46 s, 54 s, and 65 s, respectively; and (f) at time 105 s when the filament is back in its neutral position after release by the cell (where a video of this event is shown at 3 × the actual rate). The white dotted curves on panels (b)-(e) represent the deflected filament shapes predicted by cantilever rod theory (enhanced online) [URL: http://dx.doi.org/10.1063/1.3628454.1].

Figures 2(a)–2(f) constitute a series of bright-field images (collected on a microscope of 0.75 numerical aperture) of four *D. discoideum* cells migrating randomly on a glass slide. One of these cells contacts the cantilever filament in Figure 2(a). This cell deflects the filament by exerting pulling force on it in Figures 2(b)–2(e), and releases it in Figure 2(f) (see online video of this event, shown at 3 × the actual rate). The shape of the pseudopod evolves throughout this event. We have observed $\sim 10^2$ such events. Clearly, these filaments are flexible enough to deflect visibly upon contact by a foraging cell (yet stiff enough to resist visible thermal motion). In the small deflection approximation, the shape of a cantilever rod of length L and radius r that is bent by a force F_A applied to its free end is described by[10]

$$\delta_F(x) = \frac{F_A}{6EI} x^2 (3L - x), \tag{1}$$

where $I = \pi r^4/4$ is the area moment of inertia of the solid cylindrical rod, E is Young's modulus of the rod-material, and x denotes position along the rod length with respect to the fixed end. This function was fitted to the deflected filament profiles in panels (b)–(e), as designated by the white dashed curves overlaid upon these micrographs. As discussed below, no adjustable parameters were used in achieving these fits.

Figure 3(a) shows a scanning electron micrograph of a *D. discoideum* cell that was fixed shortly (5 s) after establishing pseudopod-filament contact.[11] An enlarged view of the contact region is shown in Figure 3(b). The surface of the pseudopod-tip is butted against the left side of the filament. The pseudopod does not encompass the filament. The two other pseudopod-filament contacts that were characterized also exhibited butt-joint contact-structure. Deflection by a *pulling*-force (as illustrated in Figures 2(b)–2(e)) that is applied at a simple butt-joint implies *adhesive* contact between the joined pseudopod and filament surfaces. As with better characterized adhesive contacts like focal adhesions[12] and actin foci,[13] adhesion is likely due to numerous transmembrane cellular adhesion molecules (of undetermined type) that bind the substrate surface.

Knowledge of the radius, Young's modulus, and length of a solid, cylindrical cantilever rod permits calculation of its theoretical spring constant k_{Th} in the small deflection approximation: $k_{Th} = 3EI/L^3$.[10] To assess how well this simple equation predicts the spring constants of PEDOT filaments, we have used an AFM to directly measure the k_F values of several filaments and compared these values to the corresponding k_{Th} values. The AFM (MFP-3D, Asylum Research) was calibrated by pressing its cantilever (NP-0, Veeco) against a hard glass surface to quantify the cantilever deflection-photodiode voltage relationship. The spring constant k_C of this cantilever was determined by the thermal method.[14] Hooke's law then gives the magnitude of the elastic force exerted by the cantilever F_C for deflection δ_C: $F_C = k_C \delta_C$. To measure the spring constant of a PEDOT filament k_F, the AFM cantilever was pressed against an individual filament by lowering the AFM head by distance Δz, as depicted in Figure 4(a).[15] This measurement deflects the filament by distance δ_F and yields a δ_C vs Δz profile (solid line in Figure 4(b)). The opposing forces exerted by the filament F_F and cantilever F_C are equal in magnitude (Newton's 3rd law); hence, $k_F \delta_F = k_C \delta_C$, where δ_F is the (unknown) filament displacement and $F_F = k_F \delta_F$. Δz is related to δ_C and δ_F by $\Delta z = \delta_C + \delta_F$, giving $k_F = k_C(\Delta z/\delta_C - 1)^{-1}$.

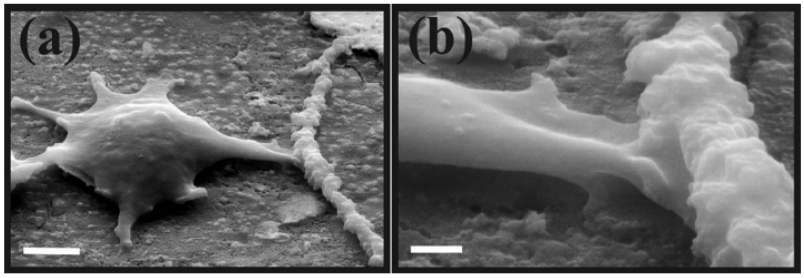

FIG. 3. (a) Scanning electron micrograph of fixed cell with a pseudopod in direct contact with PEDOT filament. Scale bar = 2 μm. (b) Enlarged view of contact region. Scale bar = 500 nm.

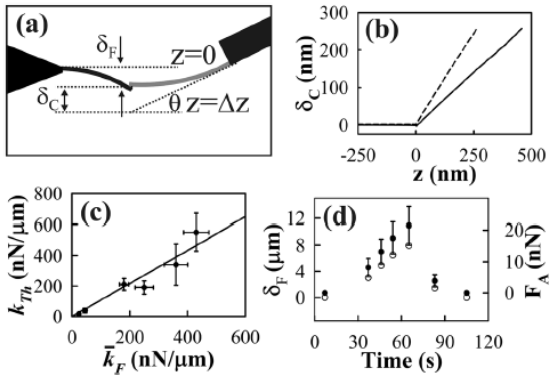

FIG. 4. (a) Schematic of AFM-based determination of the filament spring constant. The gray curve denotes the AFM cantilever while the black curve denotes the filament. (b) AFM cantilever deflection magnitude δ_C versus vertical position of AFM head z for pressure against a rigid surface (dashed profile) and a PEDOT filament (solid profile). (c) Plot of the theoretical spring constants of PEDOT filaments versus their measured spring constants. The solid line is the best linear fit to the points. (d) Cell enforced deflection (unfilled circles) and force (filled circles) measured during the event depicted in Figure 2.

The effects of AFM cantilever tilt by angle θ (11° for all cases in this study) and off-end loading of the filament are accounted for by corrective factors, yielding[16]

$$k_F = k_C(\Delta z/\delta_C - 1)^{-1}\left(\frac{L-\Delta L}{L}\right)^3 \cos^{-2}\theta. \qquad (2)$$

ΔL is the distance from the filament tip to the loading point as measured via an internal optical microscope in the AFM. The spring constants of six different PEDOT filaments k_F were obtained by substituting into Eq. (2) the corresponding k_C, L, ΔL, and $\delta_C/\Delta z$ values given in Table I. Each filament was characterized three times with each of three different cantilevers whose spring constants varied significantly. The averages of these nine determinations for each of the six filaments are reported in column $\bar{k}_F$.

To calculate the k_{Th} values, we approximate the PEDOT filament shapes as cylinders having radii equal to the lengthwise averaged radii of the filaments. These SEM determined values are reported with their standard deviations in Table I. Also, we have taken $E = 2.0$ GPa, the average of two recent determinations (1.8 GPa (Ref. 17) and 2.26 GPa (Ref. 18)) of the PEDOT Young's modulus. Figure 4(c) plots k_{Th} vs $\bar{k}_F$. The horizontal error bars denote the standard error associated with the $\bar{k}_F$ determinations; the vertical error bars result from propagation of radial standard deviations and ± 0.03 μm length nonuniformities in the k_{Th} calculations. The solid line, the best-fit to these points (constrained to pass through the origin), has a near-unity slope of 1.08. Hence, the correlation between k_{Th} and $\bar{k}_F$ is strong, indicating that cantilever rod theory provides reasonable predictions of the filament spring constants. While it lies beyond the scope of this letter to do so here, the PEDOT filaments have lengthwise radial variations of 10%–20%, so the success of $k_{Th} = 3EI/L^3$ deserves further examination.

Figure 4(d) shows the filament deflection-values (unfilled circles) corresponding to frames 2(a)–2(f) (except for the point at 83 s whose image is not shown in Figure 2).

TABLE I. Measured properties of six PEDOT filaments and their associated spring constants (in units of nN/μm).

r (μm)	L (μm)	ΔL (μm)	$\frac{\delta_c}{\Delta z}$	k_c	k_{Th}	k_F	$\bar{k}_F$
0.72 ± 0.08	13.24	1.3	0.59	450	550	490	430
0.64 ± 0.06	15.55	2.2	0.49	270	210	170	180
0.52 ± 0.06	12.18	1.8	0.77	110	190	240	250
0.61 ± 0.12	12.38	0.5	0.57	310	340	380	360
0.28 ± 0.06	12.04	2.2	0.42	58	16	20	24
0.29 ± 0.06	9.50	0.5	0.90	55	39	40	45

SEM analysis of this filament revealed a 220 nm lengthwise averaged radius and 16.0 μm length. Hence, as demonstrated above, cantilever rod theory ($k_F = 3EI/L^3$) indicates a spring constant k_F of 2.7 ± 0.7 nN/μm; the sizable uncertainty is expected given the highly nonlinear functionality of k_F. Conversion of these δ_F-values to F_A-values via Hooke's law ($F_A = \delta_F k_F$) yields the filled circles in Figure 4(d). (The error bars reflect the propagated uncertainties of δ_F and k_F.) As these data and Figure 2(e) show, F_A reaches 21 nN without breaking contact. The measured force values of 8, 13, 18, and 21 nN reported in Figure 4(d) (along with $I = 1.8 \times 10^{-27}$ m^4 and $E = 2.0$ GPa) were used to calculate the parameters $F_A/6EI$ in Eq. (1) to fully determine the shape functions (white dotted lines) shown in Figures 2(b)–2(e), respectively. The close agreement with the measured shapes confirms the usefulness of cantilever rod theory for predicting the elastic properties of these PEDOT filaments. In future studies, we will employ this methodology for the simultaneous visualization and measurement of forces exerted at single pseudopod-filament contacts to articulate the factors that dictate adhesion strength and duration.

This work was partially supported by National Science Foundation grants PHY-0646966 (B.N.F.) and DMR-0603144 (B.M.L.).

[1]P. Friedl, S. Borgmann, and E. B. Brocker, J. Leukoc. Biol. **70**, 491 (2001).
[2]A. Muller, B. Homey, H. Soto, N. F. Ge, D. Catron, M. E. Buchanan, T. McClanahan, E. Murphy, W. Yuan, S. N. Wagner, J. L. Barrera, A. Mohar, E. Verastegui, and A. Zlotnik, Nature **410**(6824), 50 (2001).
[3]N. Andrew and R. H. Insall, Nat. Cell Biol. **9**(2), 193 (2007).
[4]A. K. Harris, D. Stopak, and P. Wild, Science **208**, 177 (1980).
[5]U. S. Schwartz, N. Q. Balaban, D. Riveline, A. Bershadsky, B. Geiger, and S. A. Safran, Biophys. J. **83**, 1380 (2002).
[6]G. Pfister, C. M. Stroh, H. Perschinka, M. Kind, M. Knoflach, P. Hinterdorfer, and G. Wick, J. Cell Sci. **118**(8), 1587 (2005).
[7]S. M. Richardson-Burns, J. L. Hendricks, and D. C. Martin, J. Neural Eng. **4**, L6 (2007).
[8]P. S. Thapa, B. J. Ackerson, D. R. Grischkowsky, and B. N. Flanders, Nanotechnology **20**, 235307 (2009).
[9]D. J. Watts and J. M. Ashworth, Biochem. J. **119**, 171 (1970).
[10]L. D. Landau and E. M. Lifshitz, *Theory of Elasticity* (Butterworth-Heinemann, Oxford, 2000).
[11]J. A. Araujo, F. C. Téran, R. A. Oliveira, E. A. A. Nour, M. A. P. Montenegro, J. R. Campos, and R. F. Vazoller, J. Electron Microsc. **52**(4), 429 (2003).
[12]B. Geiger, J. P. Spatz, and A. D. Bershadsky, Nat. Rev. Mol. Cell Biol. **10**, 21 (2009).
[13]K. S. K. Uchida and S. Yumura, J. Cell Sci. **117**, 1443 (2004).
[14]J. L. Hutter and J. Bechhoefer, Rev. Sci. Instrum. **64**, 1868 (1993).
[15]S. Yang and T. Saif, Rev. Sci. Instrum. **76**, 044301 (2005).
[16]R. S. Gates and M. G. Reitsma, Rev. Sci. Instrum. **78**, 086101 (2007).
[17]H. Okuzaki and M. Ishihara, Macromol. Rapid Commun. **24**, 261 (2003).
[18]D. Tahk, H. H. Lee, and D. Y. Khang, Macromolecules **42**, 7079 (2009).

Appendix B - Long reach cantilevers for sub-cellular force measurements

IOP PUBLISHING NANOTECHNOLOGY
Nanotechnology 23 (2012) 455105 (8pp) doi:10.1088/0957-4484/23/45/455105

Long reach cantilevers for sub-cellular force measurements

Govind Paneru[1], Prem S Thapa[2], Sean P McBride[1,3], Adam Ramm[1], Bruce M Law[1] and Bret N Flanders[1,4]

[1] Department of Physics, Kansas State University, Manhattan, KS 66506-2601, USA
[2] Imaging and Analytical Microscopy Lab, University of Kansas, Lawrence, KS 66045, USA

E-mail: bret.flanders@phys.ksu.edu

Received 9 June 2012, in final form 6 August 2012
Published 19 October 2012
Online at stacks.iop.org/Nano/23/455105

Abstract
Maneuverable, high aspect ratio poly(3,4-ethylene dioxythiophene) (PEDOT) fibers are fabricated for use as cellular force probes that can interface with individual pseudopod adhesive contact sites without forming unintentional secondary contacts to the cell. The straight fibers have lengths between 5 and 40 μm and spring constants in the 0.07–23.2 nN μm^{-1} range. The spring constants of these fibers were measured directly using an atomic force microscope (AFM). These AFM measurements corroborate determinations based on the transverse vibrational resonance frequencies of the fibers, which is a more convenient method. These fibers are employed to characterize the time dependent forces exerted at adhesive contacts between apical pseudopods of highly migratory *D. discoideum* cells and the PEDOT fibers, finding an average terminal force of 3.1 ± 2.7 nN and lifetime of 23.4 ± 18.5 s to be associated with these contacts.

S Online supplementary data available from stacks.iop.org/Nano/23/455105/mmedia

1. Introduction

Pseudopod-facilitated motility is a critical aspect of the amoeboid migration exhibited by *D. discoideum*, neutrophils, T lymphocytes [1], and other highly migratory cells [2]. These cells crawl at rates as high as ∼30 μm min^{-1} to forage for micro-organisms and antigens in their local environments [3]. To achieve such high speeds, the cells must adhere to and release the supporting substrates quickly. Pre-aggregative (i.e. migratory) *D. discoideum*, for example, were recently reported to form adhesive contacts (called actin foci) that form and decay on ∼20 s time scales [4]. The short-lived nature of these contacts differs significantly from the ∼20 min lifetimes of the focal adhesion complexes used by slow-migrating cells such as keratinocytes and fibroblasts [5]. In contrast to focal adhesion complexes, which have been intensively studied at the single complex level for over a decade [6–8], comparatively little is known about the adhesive structures and dynamics of highly migratory cells.

The amoeboid paradigm of cellular movement [9, 10] essentially consists of reception of stimuli (e.g. a signaling molecule at a cell surface receptor) followed by the localized protrusion of exploratory appendages, such as pseudopods, from the cell. A typical pseudopod (figure 1(a)) is a few microns in length and has a sub-micron tip size. A cell may protrude many pseudopods at a given time. Commonly, the pseudopod will adhere its foremost tip to the local substrate [9–11]. Contraction of the actin cytoskeleton along the pseudopod axis (by molecular motors) pulls the cell towards the adhesive contact. The molecular-level mechanisms by which pseudopods adhere to substrates for both *D. discoideum* and amoeboid leukocytes are not known [12, 13]. However, these are the first contacts that the cell makes with the anterior substrate, and the traction forces exerted against the substrate at these sites dictate the cell's instantaneous direction of migration. Hence, they are a key aspect of amoeboid motility. Characterization of the dynamical forces exerted at these contacts would constitute a key step towards resolving the potential energy surface associated with the adhesion and, ultimately, controlling the transient adhesive contact mechanism in highly migratory cells.

[3] Present address: James Franck Institute and Department of Physics, The University of Chicago, Chicago, IL 60637, USA.
[4] Author to whom any correspondence should be addressed.

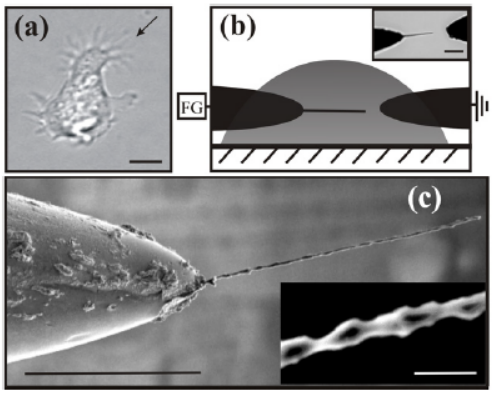

Figure 1. (a) Optical micrograph of a *D. Discoideum* cell extending pseudopods. A pseudopod is indicated by the arrow. Scale bar = 5 μm. (b) Schematic depicting the side-view of the experimental setup for PEDOT fiber growth. FG designates a function generator. Inset: optical micrograph depicting the bottom view of the setup. Scale bar = 10 μm. (c) SEM image of a PEDOT fiber grown from an etched tungsten tip. Scale bar = 20 μm. Inset: enlarged view of the fiber. Scale bar 1 μm.

A variety of methods are used to characterize the forces that cells exert at their adhesive substrate contacts. The deformable substrate technique measures cell-induced wrinkling or marker displacement within an elastic substrate [14]. This approach does not directly measure the forces exerted at the individual contacts, but rather extracts them by modeling the deformation-map induced by the whole cell. This can be a non-trivial undertaking [15]. Approaches that utilize atomic force microscopy (AFM) provide excellent resolution of the dynamical forces exerted between cells and substrates [16]. Single-cell force spectroscopy [17] entails the attachment of a living cell to an AFM cantilever that is then lowered into contact with a substrate. The substrate is typically functionalized with a ligand of interest (e.g. fibronectin) [18, 19]. The force on the AFM cantilever is then measured as the cantilever–cell unit is retracted from the substrate. This method has shed light on a wide range of ligand–receptor adhesive interactions [20–22], as have the conceptually similar biomembrane force probe [23] and laser trap [24] methods. A challenge for such cell-as-probe techniques lies in minimizing the contact area to a single, cell-initiated adhesive contact: that between a pseudopod tip and a substrate, for example.

What is needed is a long, thin probe that can interface with targeted sites, such as the adhesive contacts of pseudopods, without forming unintentional secondary contacts to the cell. Therefore, this study presents a methodology for fabricating and calibrating high aspect ratio PEDOT fibers for use as cellular force probes. These cantilevers are an improvement over on-chip PEDOT force sensors reported recently [25] because these cantilevers are considerably easier to calibrate, and they may be maneuvered independently around a cell, permitting both lateral and apical (topside) targets on the cellular surface to be probed. This capability enables interrogation of the off-plane, pseudopod-facilitated motility that occurs in nature when amoeboid cells migrate through 3D matrices.

2. Experimental methods

Direct characterization of a ~400 nm wide pseudopod (see figure 1(a)) requires a probe of comparable dimension. The probe should also have a sufficiently high aspect ratio to allow it to cleanly reach a targeted site without forming unintentional, secondary contacts with the cell. To meet these requirements, we have fabricated cantilevered force sensors composed of poly(3,4-ethylene dioxythiophene) (PEDOT) fibers grown from the tips of etched tungsten wire. The bottom 5 mm of a vertically oriented tungsten filament (0.019 in diameter, SmallParts) which was biased at +4 V was electro-etched by repeated dipping over a ~4 min period into a 10 M $NaNO_2$ 6 M KOH solution that was electrically grounded, as described elsewhere [26]. This procedure yields conical tips with radii of curvature of ~1μm or less. Reproducibility was optimized by using a sewing machine to cycle the filament in and out of solution at a rate of ~10 s^{-1}. We used the simple polymerization technique directed electrochemical nanowire assembly (DENA) to grow the PEDOT fiber from the tip of the tungsten filament [27–29]. Briefly, the tungsten filament was first evaporatively coated with ~200 nm of Au to promote strong attachment of the polymer. After mounting the coated filament in a 3D stage and positioning it ~1 μm above a microscope slide, a 20 μl aliquot of aqueous solution containing 0.01 M 3,4-ethylene dioxythiophene and 0.02 M poly(sodium styrene sulfonate) was deposited across the ~30 μm gap between the wire tip and an Au counter-electrode that was similarly mounted. Figure 1(b) is a schematic diagram of this arrangement. A square wave voltage signal (±3.5 V, 10.0 kHz) was applied to the electrodes to induce PEDOT nano-fiber growth via electrochemical polymerization [30]. As explained elsewhere, the voltage–frequency sets the average radii of the fibers during growth [30], but spatiotemporal fluctuations in the polymerization rate of the amorphous PEDOT material give rise to radial variation (~50%) about the mean radius [28, 29]. The voltage signal is terminated after a few seconds when the PEDOT nano-fiber reaches the desired length. Translation of the microscope stage pulls the solution-drop away from the nano-fiber, straightening it due to the tension at the air–filament–solution contact line. The nano-fibers retain their straightened geometries upon re-immersion in aqueous solution. A scanning electron micrograph of a typical straightened nano-fiber is shown in figure 1(c).

We have used an atomic force microscope (AFM, model MFP-3D, Asylum Research) to directly measure the spring constants k_F of the PEDOT fibers, as detailed elsewhere [25]. Briefly, this was done by lowering a calibrated AFM cantilever (CSC12/tipless, MikroMasch) of spring constant k_C by distance Δz against an individual fiber in order to deflect it by distance δ_C, as illustrated in figure 2(a) and plotted in figure 2(b) [31]. When the opposing forces exerted by the fiber and the cantilever are equal

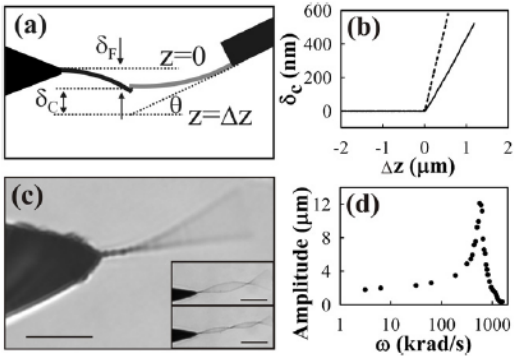

Figure 2. (a) Schematic of AFM-based setup for measuring the spring constant of a PEDOT fiber. (b) AFM cantilever deflection magnitude δ_C versus vertical position of AFM head Δz for pressure against a rigid surface (dashed profile) and a PEDOT fiber (solid profile). (c) Optical micrograph of a PEDOT fiber resonating at its fundamental frequency. Scale bar = 15 μm. Inset: optical images of a PEDOT fiber resonating in its first (upper) and second (lower) harmonic modes. Scale bar = 15 μm. (d) Amplitude versus driving frequency plot for the PEDOT fiber in panel (c).

in magnitude, the following expression relates the spring constant of the fiber to the measured quantities [32, 25]:

$$k_F = k_C\,(\Delta z/\delta_C - 1)^{-1}\left(\frac{L-\Delta L}{L}\right)^3 \cos^{-2}\theta. \qquad (1)$$

δ_C is the deflection of the cantilever and L is the length of the fiber. The tilt angle θ of the AFM cantilever was 11° for all cases in this study. The position of contact from the end of the fiber ΔL was measured via an internal optical microscope in the AFM.

We have also determined the spring constants of the PEDOT cantilevers by the resonance frequency method, which is technically simpler than the AFM method [33]. To measure the resonance frequency of a PEDOT fiber, we position it ~10 μm from an Au counter-electrode. A ±20 V sinusoidal voltage signal of frequency f and a +20 V dc offset are applied to the PEDOT cantilever while the Au electrode is grounded [34]; polarization forces drive transverse oscillation of the PEDOT fiber at this frequency. A bright field image of a cantilever resonating in its fundamental mode is shown in figure 2(c). Images of the vibrating fiber are collected as f is increased in 5 kHz steps. A representative amplitude versus angular frequency plot is depicted in figure 2(d), where the angular frequency ω is defined as $\omega = 2\pi f$. The frequency at which the amplitude reaches its first maximum locates the fundamental resonance frequency ω_0 (565 krad s^{-1} in figure 2(d)). Amplitude maxima at frequencies of half the observed resonance frequency were not observed, and the vibrational amplitude was directly proportional to the voltage amplitude, confirming that the reported ω_0-values are fundamental frequencies [33]. The resonance frequencies of the tungsten filament are well below those of the PEDOT cantilever and, hence, do not complicate these measurements.

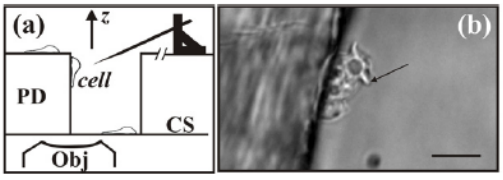

Figure 3. (a) Schematic diagram (not to scale) of the side-view imaging setup depicting the Petri dish (PD), coverslip (CS), and microscope objective (Obj). (b) Side-view micrograph of a *D. Discoideum* cell extending apical pseudopods. The apical pseudopod indicated by the arrow is 2.5 μm long and ~400 nm wide. Scale bar = 10 μm.

The spring constant k_{res} of a radially uniform and solid cantilevered rod of length L depends on ω_0 as

$$k_{res} = 0.08\frac{\pi\rho_m^2 L^5}{E}\omega_0^4. \qquad (2)$$

ρ_m is the mass density of the fiber material (PEDOT) and E its Young modulus. Equation (2) was derived by using the expression for ω_0 of a radially uniform rod $\omega_0 = 1.75\sqrt{E\rho^{-1}}rL^{-2}$ to eliminate r in the expression for the spring constant k of a uniform rod $k = \frac{3\pi Er^4}{4L^3}$ [35]. As explained below, equation (2) was used to predict the spring constants of the PEDOT fibers.

Type KAx3 *D. discoideum* cells [36], grown at 24 °C, were removed from HL-5 culturing medium by drawing 1000 μl of the cell–medium suspension from a Petri dish and centrifuging the aliquot for ~10 s at 1.34 × 10^3 g. The supernatant was discarded and the cells were washed twice with 12 mM phosphate buffer and shaken before suspending the cells a final time in phosphate buffer and starving them for 4–6 h. 50 μl volumes of cell suspension and phosphate buffer were deposited in the side-view imaging chamber described below. A waiting time of ~20 min, following cell deposition, was required for the cells to settle and begin migrating on the surfaces of the chamber.

To facilitate investigation of apical pseudopods, which are important for amoeboid migration through 3D matrices, cells were visualized in profile so that the size, shape and cellular location of the pseudopod–fiber contact could be clearly observed. This mode requires that the imaging plane of the microscope be perpendicular to the substrate on which the cell crawls. Our setup for realizing this perspective, which differs from that reported elsewhere [37], is diagrammed in figure 3(a). Briefly, a hole was bored in the base of a Petri dish (Fisherbrand) using a 7/32″ drill bit at 990 rpm; these parameters minimized lip and sidewall roughness (~3 μm). A coverslip was cemented to the underside of the dish to seal the hole. *D. discoideum* cells were cultured and introduced to the chamber at cell surface densities of ~10^3 mm^{-2}. The dish was mounted on the stage of an inverted microscope (Leica IRB) for optical imaging, primarily with a 63× water immersion objective of 0.90 numerical aperture. Side-view imaging of the cells was accomplished by focusing the microscope on those migrating on the sidewalls of the hole.

Table 1. Parameters for the spring constant measurements.

Fiber	L (μm)	$\frac{\delta_C}{\Delta z}$	ΔL (μm)	k_C (nN μm^{-1})	k_F (nN μm^{-1})	$\overline{k_F}$ (nN μm^{-1})	ω_0 (krad s^{-1})	r_{res} (nm)	k_{res} (nN μm^{-1})
1	7.22	0.28	0.5	58	18.9	18.0	7850	202	21.0
2	14.58	0.34	6.56	58	5.3	5.1	2292.2	241	5.1
3	15.08	0.22	6.56	61	3.2	3.1	2009.6	226	3.6
4	9.66	0.41	2.2	61	20.2	19.0	5149.6	238	16.7
5	10.66	0.45	3.9	64	13.6	13.8	4207.6	237	12.2
6	8.80	0.41	3.06	60	12.1	12.1	5338	204	12.1
7	8.74	0.47	2.18	60	23.2	23.2	6091.6	230	19.8
8	12.39	0.3	4.8	61	6.2	6.1	2888.8	219	5.7
9	7.94	0.55	3	65.9	20.1	21.6	6908	216	20.3
10	10.36	0.5	3.06	60.8	22.1	21.4	5024	267	21.5
11	9.19	0.34	2.18	60.8	14.3	14.0	5149.6	215	13.0
12	9.72	0.54	3.93	65.3	16.7	16.7	4961.2	232	14.8
13	9.36	0.49	3.5	65.3	15.6	16.3	5275.2	229	15.7
14	10.83	0.37	4.37	62.8	8	8.2	3705.2	215	7.9
15	8.44	0.36	2.6	61	11.7	11.0	5212.4	184	8.9
16	12.84	—	—	—	—	—	2449.2	200	3.6
17	17.0	—	—	—	—	—	1382	198	1.5
18	20.0	—	—	—	—	—	1118	221	1.4
19	23.0	—	—	—	—	—	942	247	1.4
20	24.0	—	—	—	—	—	816	232	1.0
21	28.41	—	—	—	—	—	439.6	176	0.2
22	34.0	—	—	—	—	—	377	216	0.3
23	30.0	—	—	—	—	—	565	252	0.7
24	41.0	—	—	—	—	—	220	183	0.07
25	16.73	—	—	—	—	—	1758.4	244	3.5

A typical side-view image of a *D. discoideum* cell is shown in figure 3(b). The arrow points to an apical pseudopod.

3. Results

We have directly measured the spring constants of 15 different PEDOT fibers by using an AFM as described above. The measured k_C, $\delta_C/\Delta z$, L, and ΔL values were substituted into (1) to obtain the corresponding k_F determinations. Each fiber was characterized three times. The average of the three k_F determinations is denoted $\bar{k}_F$. All quantities required to make these spring constant determinations are reported in table 1 (fibers 1–15).

Figure 2(c) shows a PEDOT fiber (23 in table 1) resonating in its fundamental mode at 90 kHz. (It also resonates in its harmonic modes, as the insets show, demonstrating its strong elastic character.) Figure 2(d) is the amplitude versus frequency plot for the fiber of panel (c), indicating a fundamental resonance frequency ω_0 of 565 $\times$ 10^3 rad s^{-1}. By substituting this ω_0 value into (2), we obtain a prediction of its spring constant k_{res} of 7.0 $\times$ 10^{-4} N m^{-1}. In calculating this result, we took the PEDOT Young modulus E to be 2.0 GPa, the average of two recent determinations (1.8 GPa [38] and 2.26 GPa [39]), and the mass density ρ_m to be 1500 kg m^{-3} [40]. By using (2) we implicitly assume that a radially non-uniform PEDOT fiber of length L both resonates and bends like a hypothetical PEDOT fiber of a constant radius (and length L). This relation is not generally true of structurally non-uniform fibers. Therefore, in figure 4(a) we have assessed the extent to which the resonance-based determinations are accurate by plotting the measured k_{res} values for 15 fibers against their measured $\bar{k}_F$ values. These data are best fitted by a line having a near-unity slope of 0.95. It is clear that the k_{res}-values predict the spring constants of the PEDOT cantilevers with reasonable accuracy; moreover, in the small k range ($\sim$4 nN μm^{-1}) used in the cellular force application, the agreement is excellent. Hence, the resonance frequency calibration method, though approximate, is sufficiently accurate to justify forgoing the somewhat laborious AFM method. Fibers 16–24 in table 1, several of which were too compliant for the AFM method, were characterized using the resonance frequency method.

The inset to figure 4(a) depicts two spring constant distributions corresponding to two sets of fibers grown with different frequencies of the alternating voltage to approximately the same lengths. As described elsewhere [30], the frequency of the alternating voltage sets the average radii of the fibers, with higher frequencies producing thinner fibers. One distribution (unfilled vertical bars) describes 14 fibers grown using a frequency of 10.0 kHz to a length of 23.8 $\pm$ 0.8 μm (unfilled vertical bars). The average spring constant for these fibers is 0.8 $\pm$ 0.6 nN μm^{-1}. The other distribution (filled vertical bars) describes eight fibers grown using a frequency of 20.0 kHz to a length of 23.4 $\pm$ 1.9 μm. The average spring constant of these fibers is 0.08 $\pm$ 0.04 nN μm^{-1}. Hence, the spring constants of the fibers may be controlled across reasonably narrow ranges by controlling the frequency of the alternating voltage during growth, as well as the length of the fiber.

To assess the degree to which the structural non-uniformity of the fibers causes anisotropy in their spring constants, we have measured the ω_0-values in planes of

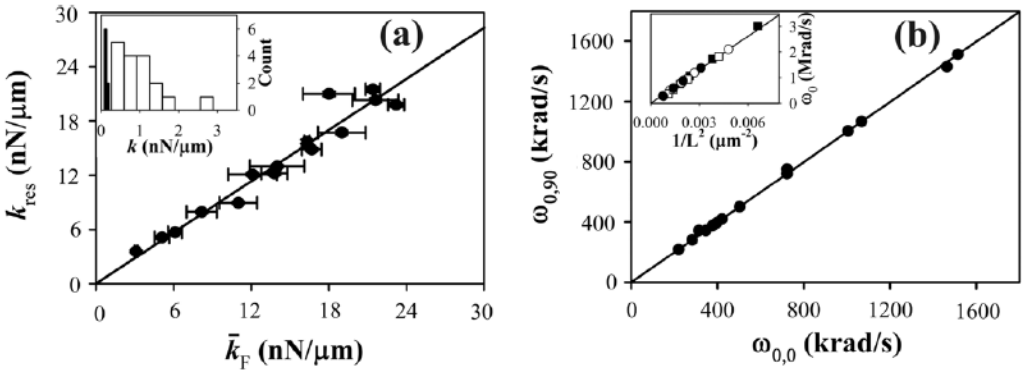

Figure 4. (a) Plot of resonance-based spring constant determinations k_{res} versus those measured by AFM $\overline{k_F}$ (filled circles). The solid line (constrained to pass through the origin) is the best fit to the points. The horizontal error bars denote the standard deviation of the mean associated with the $\bar{k}_F$ determinations; the vertical error bars, which are nearly too small to see, denote the propagated uncertainty in measuring ω and L. Inset: distributions of the spring constants of fibers grown at 10.0 kHz to a length of 23.8 ± 0.8 μm (unfilled vertical bars) and at 20.0 kHz to a length of 23.4 ± 1.9 μm (filled vertical bars). (b) Plot of the fundamental resonance frequencies of PEDOT fibers $\omega_{0,0}$ against those measured when the fibers were axially rotated by 90° $\omega_{0,90}$. The solid line through the data points (filled circles) has a slope of unity. Inset: plot of ω_0 for single fibers that were shortened (by breaking their tips) three times versus the inverse square of their lengths $1/L^2$. The solid line is a best fit through the data points. The four data-sets (circles, squares, unfilled circles, and unfilled squares) correspond to four different fibers.

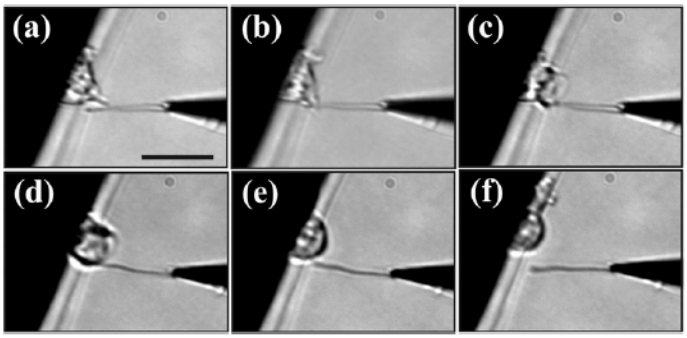

Figure 5. A series of optical micrographs of a cantilevered PEDOT fiber (a) in its neutral position after contact initiation by the pseudopod; (b)–(d) while being deflected upwards by the cell at times 0 s, 22 s, 68 s, 98 s, and 100 s respectively; and (f) at time 118 s when the fiber is back in its neutral position after release by the cell. A video of this event shown at ∼6× the actual rate is available online (AVI type, file size 677 KB, at stacks.iop.org/Nano/23/455105/mmedia). The scale bar in panel (a) denotes 15 μm.

bending that differ by 90° axial rotation. These resonance frequency values are denoted $\omega_{0,0}$ and $\omega_{0,90}$. Figure 4(b) plots the measured $\omega_{0,90}$-value against the corresponding $\omega_{0,0}$-value for 14 different fibers. These data are well fitted by a line of unit slope, indicating that the $\omega_{0,0}$- and $\omega_{0,90}$-values for a given fiber are equal. Another concern is that the fibers grow unevenly such that their tips have different average thicknesses from their bases. The inset to figure 4(b) plots ω_0 for single fibers that were shortened (by breaking off their tips) three times versus the inverse square of their lengths $1/L^2$. The different symbols represent the data-sets for the four fibers that were examined in this manner. These data lie along a single line, as indicated by the best fit (solid line).

Figures 5(a)–(f) constitute a series of side-view images of a *D. discoideum* cell migrating on the vertical sidewall. An apical pseudopod adheres to the cantilever in panel (a), deflects it by exerting a pulling force on it in panels (b)–(d), and releases it in panel (e). A video of this event, shown at ∼6× the actual rate, is available as supporting information (available at stacks.iop.org/Nano/23/455105/mmedia). These images depict an apical pseudopod–cantilever deflection event, where the cantilever represents a secondary substrate. The measured deflection $\delta_F(L)$ of the fiber is extracted from these images by finding the distance between the tips of the deflected and undeflected fibers. (Drift of the microscope stage occurred at a rate of 0.09 μm min^{-1} and, therefore, does not compromise the $\delta_F(L)$ determinations.) The shape of the pseudopod evolves throughout this event.

Figure 6(a) shows the fiber-end deflection values $\delta_F(L)$ (unfilled circles) corresponding to the apical pseudopod

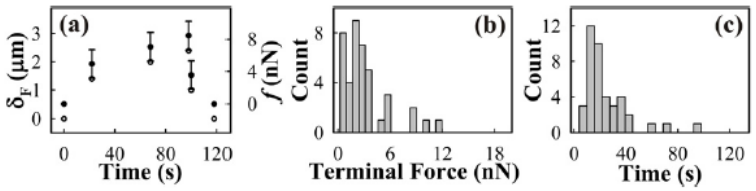

Figure 6. (a) Apical pseudopod induced deflection (unfilled circles) and force (filled circles) measured during the event depicted in figure 5. The error bars reflect the propagated uncertainties of δ_F and k_{res}. (b) Distribution of the terminal forces obtained from 41 pseudopod–fiber deflection events. (c) Distribution of contact durations obtained from the same set of 41 events.

deflection event of figures 5(a)–(f). This fiber—wire 25 in table 1—was found to have a spring constant k_{res} of 3.5 ± 0.3 nN μm^{-1}. Conversion of the δ_F-values to forces f via Hooke's law ($f = \delta_F k_{res}$) yields the filled circles in figure 6(a). These data show that f reaches 8.5 nN without breaking contact. A total of 41 apical pseudopod–fiber deflection events were observed in this study. Figure 6(b) depicts the distribution of the terminal forces for these events. *Terminal force* refers to the force applied to the fiber the instant before it recoiled to its neutral position. The average terminal force was 3.1 ± 2.7 nN. Figure 6(c) depicts the distribution of the durations of these events. The average contact duration was 23.4 ± 18.5 s.

4. Discussion

This study presents methodology for fabricating cantilevered cellular force sensors composed of PEDOT fibers grown from maneuverable substrates. The diameter and length of a fiber are user controlled during the growth process and, consequently, the spring constants of the fibers may be controlled across reasonably narrow ranges as shown in the inset to figure 4(a). These force sensors are calibrated either by measuring the fibers' spring constants directly via AFM or, more conveniently, by finding their resonance frequencies for transverse vibration. The near-unit slope of figure 4(a) implies that the resonance frequency calibration method (i.e. equation (2)), though approximate, is sufficiently accurate to forgo the more laborious AFM method. In applying (2) to the PEDOT fibers, we assume that the fiber bends like a hypothetical uniform fiber having a particular radius and vibrates like a uniform fiber of the same radius. However, the PEDOT fibers are radially non-uniform (inset of figure 1(c)). For structurally non-uniform cantilevers, this assumption is not strictly true. The spring constant and the resonance frequencies of a cantilever are derived from different forms of Newton's second law: for the former, there is no net torque on the fiber; for the latter the net torque varies periodically with time. Hence, it is somewhat fortuitous that the resonance-based spring constant determinations were found to be accurate (figure 4(a)). The theoretical analysis required to quantify the limits of this approximation lies beyond the scope of this work.

Because the fibers are radially non-uniform and somewhat axially asymmetric, concern over the anisotropy of their spring constants arises. Figure 4(b) shows that the resonance frequency values in planes of bending that differ by 90° of axial rotation are essentially equal for a given fiber. Because ω_0 predicts k_F to a reasonable degree of accuracy (discussed above), this finding implies that the spring constants in orthogonal bending planes are essentially the same; thus, we do not observe a significant degree of bending anisotropy. A related concern is that the fibers grow unevenly, causing their foremost tips to have different average radii from their bases. A radially uniform fiber has a resonance frequency of $\omega_0 = 1.75\sqrt{E\rho^{-1}}rL^{-2}$. Hence, the inset to figure 4(b) shows that the PEDOT fibers resonate like radially uniform fibers, as shortening the fibers does not change the slope ($1.75\sqrt{E\rho^{-1}}r$) of their ω_0 versus L^{-2} plots. These data also provide further confirmation that fibers grown under the same controlled conditions have similar structures, as each of the four datasets shown in this plot has the same slope. Hence, the findings presented in figures 4(a) and (b) justify calibrating these fibers via the comparatively straightforward resonance method.

Typical lengths of the PEDOT fibers are ∼20 μm, which provides sufficient reach to cleanly interface the tip of a fiber with a sub-cellular target on a cell without forming unintentional secondary contacts to the cell. To demonstrate this capability, we have resolved the dynamical forces that arise at individual adhesive contacts between the tips of apical pseudopods and the PEDOT cantilevers. Most prior work on pseudopod dynamics has regarded motility on planar substrates such as Petri dishes and microscope slides. However, apical pseudopod dynamics are required of *D. discoideum* in nature where the local topography of forest floors—crevices and debris—necessitates off-plane motion of a cell as it transfers from one surface to another. By employing the dynamical force sensors, the present study found the average terminal force exerted during the apical pseudopod–secondary substrate adhesive contacts to be 3.1 ± 2.7 nN and the average duration of these contacts to be 23.4 ± 18.5 s. This period compares well to the 19.4 ± 8.2 s lifetimes of the adhesive contacts made by actin foci to *basal* substrates [41], suggesting that the adhesive structures at the apical pseudopod tips may be actin foci. However, no external forces were applied to the actin foci in this prior study (although internal forces could have been present) [41]. This detail is significant because the application of a force against a bond accelerates the dissociation rate of the bond [42]. Hence, when a pulling force is applied against an actin focus, it is expected to decay more rapidly than the 19.4 s average

lifetime in the unforced case. On the other hand, apical contacts can survive for 23.4 s under few nanonewton external forces (figures 6(a) and (b)). This comparative robustness is expected to increase the probability that apical contacts survive while the pre-existing basal contacts (actin foci) decay, as required for inter-substrate (basal-to-apical) transfer. Further investigation into this mechanism will be undertaken in a future study.

5. Conclusion

This study has presented an innovative methodology for the electrochemical fabrication of cellular force sensors composed of cantilevered PEDOT fibers. Calibration of the force sensors is straightforward via measurement of the transverse resonance frequencies of the fibers. By employing these fibers to characterize the dynamics of apical pseudopod–substrate adhesive contacts of *D. discoideum* cells, we have shown that these cantilevers are effective, high aspect ratio cellular force probes that may be positioned independently around the cell and can interface with sub-micron targets without forming unintentional secondary contacts to the cell. These capabilities will permit further statistical characterization of the durations and magnitudes of the forces exerted at individual apical and lateral pseudopod–substrate contacts, as a means of elucidating the physical basis of pseudopod–substrate adhesion. We also note that the dimensions and maneuverability of the PEDOT force probes will likely permit characterization of the dynamics at other interesting adhesive entities such as the setae and spatulae of gecko feet [43] and the micro-bristles of beetle tarsi [44], which have dimensions comparable to *D. discoideum* pseudopods.

Acknowledgments

This work was partially supported by National Science Foundation grants PHY-0646966 (BNF) and DMR-0603144 (BML). We thank Robert Szoszkiewicz for helpful suggestions regarding cantilever calibration and Larry Weaver for valuable insight into the mechanics of non-uniform cantilevers.

References

[1] Friedl P, Borgmann S and Broecker E B 2001 Amoeboid leukocyte crawling throgh extracellular matrix: lessons from the *Dictyostelium* paradigm of cell movement *J. Leukoc. Biol.* **70** 491–509
[2] Muller A *et al* 2001 Involvement of chemokine receptors in breast cancer metastasis *Nature* **410** 50–6
[3] Stossel T P 1994 The machinery of blood cell movements *Blood* **84** 367–79
[4] Yumura S and Kitanishi-Yumura T 1990 Fluorescence-mediated visualisation of actin and myosin filaments in the contractile membrane-cytoskeleton complex of *Dictyostelium* discoideum *Cell Struct. Funct.* **15** 355–64
[5] Ren X S, Kiosses W B, Sieg D J, Otey C A, Schlaepfer D D and Schwartz M A 2000 Focal adhesion kinase suppresses Rho activity to promote focal adhesion turnover *J. Cell .Sci.* **113** 3673–8
[6] Galbraith C G and Sheetz M P 1997 A micromachined device provides a new bend on fibroblast traction forces *Proc. Natl Acad. Sci.* **94** 9114–8
[7] Walter N, Selhuber C, Kessler H and Spatz J P 2006 Cellular unbinding forces of initial adhesion processes on nanopatterned surfaces probed with magnetic tweezers *Nano Lett.* **6** 398–402
[8] Vogel V and Sheetz M 2006 Local force and geometry sensing regulate cell functions *Nature Rev. Mol. Cell Biol.* **7** 265–75
[9] Devreotes P N and Zigmond S H 1988 Chemotaxis in eukaryotic cells: a focus on leukocytes and *Dictyostelium* *Ann. Rev. Cell Biol.* **4** 649–86
[10] Bailly M, Condeelis J S and Segall J E 1998 Chemoattractant-induced lamellipod extension *Microsc. Res. Technol.* **43** 433–43
[11] Stossel T P, Hartwig J H, Janmey P A and Kwiatkowski D J 1999 Cell crawling two decades after Abercrombie *Biochem. Soc. Symp.* **65** 267–80
[12] Friedl P, Entschladen F, Conrad C, Niggermann B and Zanker K S 1998 CD4+ T lymphocytes migrating in three-dimensional collagen lattices lack focal adhesions and utilize beta1 integrin-independent strategies for polarization, interaction with collagen fibers and locomotion *Eur. J. Immunol.* **28** 2331–43
[13] Friedl P and Weigelin B 2008 Interstitial leukocyte migration and immune function *Nature Immunol.* **9** 960–9
[14] Harris A K, Stopak D and Wild P 1980 Silicone substrata: a new wrinkle in the study of cell locomotion *Science* **208** 177–9
[15] Schwartz U S, Balaban N Q, Riveline D, Bershadsky A, Geiger B and Safran S A 2002 Calculation of forces at focal adhesions from elastic substrate data: the effect of localized force and the need for regularization *Biophys. J.* **83** 1380–94
[16] Pfister G, Stroh C M, Perschinka H, Kind M, Knoflach M and Hinterdorfer Pand Wick G 2005 Detection of HSP60 on the membrane surface of stressed human endothelial cells by atomic force and confocal microscopy *J. Cell Sci.* **118** 1587–94
[17] Helenius J, Heisenberg C-P, Gaub H E and Muller D J 2008 Single-cell force spectroscopy *J. Cell Sci.* **121** 1785–91
[18] Sun Z, Martinez-Lemus L A, Trache A, Trzeciakowski J P, Davis G E, Pohl U and Meininger G A 2005 Mechanical properties of the interaction betwen fibronectin and alpha5beta1-integrin on vascular smooth muscle cells studied using atomic force microscopy *Am. J. Physiol.* **289** H2526–35
[19] Trache A, Trzeciakowski J P, Gardiner L, Sun Z, Muthuchamy M, Guo M, Yuan S Y and Meininger G A 2005 Histamine effects on endothelial cell fibronectin interaction studied by atomic force microscopy *Biophys. J.* **89** 2888–98
[20] Friedrichs J, Helenius J and Mueller D J 2010 Stimulated single-cell force spectroscopy to quantify cell adhesion receptor crosstalk *Proteomics* **10** 1455–62
[21] Hoffmann S, Hosseini B H, Hecker M, Louban I, Bulbuc N, Garbi N, Wabnitz G H, Samstag Y, Spatz J P and Haemmerling G J 2011 Single cell force spectroscopy of T cells recognizing a myelin-derived peptide on antigen presenting cells *Immunol. Lett.* **136** 13–20
[22] Hoffmann S C, Wabnitz G H, Samstag Y, Moldenhauer G and Ludwig T 2011 Functional analysis of bispecific antibody (EpCAMxCD3)-mediated T-lymphocyte and cancer cell interaction by single-cell force spectroscopy *Int. J. Cancer* **128** 2096–104

[23] Evans E, Ritchie K and Merkel R 1995 Sensitive force technique to probe molucular adhesion and structural linkages at biological interfaces *Biophys. J.* **68** 2580–7
[24] Litvinov R I, Shuman H, Bennett J S and Weisel J W 2002 Binding strength and activation state of single fibrinogen-integrin pairs on living cells *PNAS* **99** 7426–31
[25] Paneru G, Thapa P S, McBride S P, Nichols D M, Law B M and Flanders B N 2011 Forces at individual pseudopod-filament adhesive contacts *Appl. Phys. Lett.* **99** 093702
[26] Qiao Y, Chen J, Guo X, Cantrell D, Ruoff R and Troy J 2005 Fabrication of nanoelectrodes for neurophysiology: cathodic electrophoretic paint insulation and focused ion beam milling *Nanotechnology* **16** 1598–602
[27] Thapa P S, Barisci J N, Yu D J, Wicksted J P, Baughman R and Flanders B N 2009 Directional growth of conducting polypyrrole and polythiophene nanowires *Appl. Phys. Lett.* **94** 033104
[28] Thapa P S, Ackerson B J, Grischkowsky D R and Flanders B N 2009 Directional growth of metallic and polymeric nanowires *Nanotechnology* **20** 235307
[29] Flanders B N 2012 Directed electrochemical nanowire assembly: precise nanostructure assembly via dendritic solidification *Mod. Phys. Lett.* B **26** 1130001
[30] Ozturk B, Talukdar I and Flanders B N 2007 Directed growth of diameter-tunable nanowires *Nanotechnology* **18** 365302
[31] Yang S and Saif T 2005 Micromachined force sensors for the study of cell mechanics *Rev. Sci. Instrum.* **76** 044301
[32] Gates R S and Reitsma M G 2007 Precise atomic force microscope cantilever spring constant calibration using a reference cantilever array *Rev. Sci. Instrum.* **78** 086101
[33] Gao R, Wang Z L, Bai Z, deHeer W A, Dai L and Gao M 2000 Nanomechanics of individual carbon nanotubes from pyrolytically grown arrays *Phys. Rev. Lett.* **85** 622–5
[34] Zhou J, Lao C S, Gao P, Mai W, Hughes W L, Deng S Z, Xu N S and Wang Z L 2006 Nanowire as pico-gram balance at workplace atmosphere *Sol. State. Commun.* **139** 222–6
[35] Landau L D and Lifshitz E M 2000 *Theory of Elasticity* (Oxford: Butterworth–Heinemann)
[36] Watts D J and Ashworth J M 1970 Growth of myxameobae of the cellular slime mould *Dictyostelium* discoideum in axenic culture *Biochem. J.* **119** 171–4
[37] Chaudhuri O, Parekh S, Lam W and Fletcher D 2009 Combined atomic force microscopy and side-view optical imaging for mechanical studies of cells *Nature Methods* **6** 383–7
[38] Okuzaki H and Ishihara M 2003 Spinning and characterization of conducting microfibers *Macromol. Rapid Commun.* **24** 261–4
[39] Tahk D, Lee H H and Khang D Y 2009 Elastic moduli of organic electronic materials by the buckling method *Macromolecules* **42** 7079–83
[40] Nu L, Kvarnström C, Fröberg K and Ivaska A 2001 Electrochemically controlled surface morphology and crystallinity in poly(3.4-ethylenedioxythiophene) films *Synth. Met.* **122** 425–9
[41] Uchida K S K and Yumura S 2004 Dynamics of novel feet of *D. discoideum* during migration *J. Cell Sci.* **117** 1443–55
[42] Hänggi P, Talkner P and Borkovec M 1990 Reaction rate theory: 50 years after Kramers *Rev. Mod. Phys.* **62** 251–342
[43] Huber G, Mantz H, Spolenak R, Mecke K, Jacobs K, Gorb S N and Arzt E 2005 Evidence for capillarity contributions to gecko adhesion from single spatula nanomechanical measurements *Proc. Natl Acad. Sci.* **102** 16293–6
[44] Eisner T and Aneshansley D J 2000 Defense by foot adhesion in a beetle (Hemisphaerota cyanea) *Proc. Natl Acad. Sci.* **97** 6568–73

Appendix C - Complete reconfiguration of dendritic gold

Nanoscale

PAPER

View Article Online
View Journal | View Issue

Complete reconfiguration of dendritic gold†

Cite this: *Nanoscale*, 2014, 6, 833

Govind Paneru and Bret N. Flanders*

Received 16th August 2013
Accepted 4th November 2013

DOI: 10.1039/c3nr04317g

www.rsc.org/nanoscale

The present work extends the directed electrochemical nanowire assembly (DENA) methodology, which is a technique for growing single crystalline metallic nanowires and nano-dendrites from simple salt solutions, to enable the complete dissolution of the metallic dendrites following their growth. The experimental parameters that control this process are the frequency and the duty cycle of the alternating voltage signal that initiates electrochemical dendritic growth. Cyclic voltammetric and Raman measurements imply that the reconfiguration of dendritic gold occurs by way of the same interfacial reduction and oxidation mechanisms as bulk gold. We present a model that illustrates how the experimental parameters (frequency and duty cycle) induce reconfiguration by controlling the rates at which reduction, oxidation, and $Au^{III}Cl_4^-$ diffusion take place. This capability is significant because in making dendritic solidification a reconfigurable process, we have established an innovative means of applying fully reconfigurable metallic nano-structures to substrates; in turn, this capability could potentially enable the smart modulation of the adhesive, anti-corrosive, or optical properties of the substrate.

Introduction

A large number of materials that are capable of high dynamic range structural reconfiguration have been developed in the past few years.[1] Materials with this capability could potentially be used to confer hydrophobic, lipophobic, and anti-corrosive character to substrates in a *regenerative* manner. Structural reconfiguration is also important for man-made *smart* materials that adapt advantageously to environmental changes. Cuttlefish-skin[2] and photosynthetic corals[3] are naturally occurring, oft-cited examples of such materials. As such, reconfigurability-by-design is an important strategy in modern materials science.

The synthesis of specialized building blocks is a widely used strategy for developing reconfigurable materials. Regan and co-workers have synthesized modular peptides that assemble in solution into smart gels. These gels, having pore-sizes sufficient to trap 26 kDa proteins, undergo complete, salinity-dependent dissolution (*i.e.* cargo-release) and reformation.[4] Pine and co-workers have designed quasi-monopolar magnets that self-assemble into aggregates with reproducible configurations. These assemblies can be fully disassembled or re-assembled by controlling the external magnetic field or the salinity of the surrounding solution.[5] The basic strategy of these approaches is to produce a specialized building block that switches its character in response to a changing external field, inducing reconfiguration of the assemblies. However, in naturally occurring environments such as oceans or rivers, one would not attempt to concentrate the waters with synthetic building blocks. Instead, it would be advantageous to control the assembly and disassembly processes of more generic building blocks, such as the components of the salts that are already extant. One could then envision producing nanostructured coatings on the surfaces of, say, underwater metrological apparatus in order to provide corrosion, reflectivity, or adhesion control that could be regenerated as needed.[6–8]

As a step towards this end, the present work extends the directed electrochemical nanowire assembly (DENA) methodology[9] to enable the on-command growth and dissolution of arrays of metallic dendrites on conducting surfaces that are immersed in salty solutions. DENA is a type of dendritic solidification,[10–14] a widely occurring process that produces crystals having the distinctive *dendritic* shape observed at the hexagonal points of snowflakes.[15] In general, dendritic solidification occurs when the growth rate of a crystal is limited by the diffusion of the building blocks, usually atoms or molecules, through a *bulk* medium to the solidification front.[16,17] Spatio-temporal fluctuations in building block deposition rate create sharp protrusions on the solidification front. With further growth, the Mullins–Sekerka instability tends to enhance the growth rate and reduce the tip-radius, while the Gibbs–Thomson effect tends to retard the growth rate and fatten the tip.[18] The result is a dendrite that grows steadily with a fixed tip size.[14] Growth is in the direction of maximum surface tension; side-branches, induced by fluctuations in the deposition rate, grow in crystallographic directions that are commensurate with the main branch.[13,19] In addition to bulk diffusion, DENA[20–22] also depends on the electrochemical oxidation and reduction of

Kansas State University, Department of Physics, Manhattan, KS 66506-2601, USA. E-mail: bret.flanders@phys.ksu.edu; Tel: +1 785 532-1614

† Electronic supplementary information (ESI) available. See DOI: 10.1039/c3nr04317g

metal atoms at the crystal-solution interface. Therefore, in order to understand how the dendritic reconfiguration process occurs, both the interfacial chemical steps and the bulk diffusive process must be taken into account.

We focus on gold dendrites in this study because the electrochemistry of bulk gold is well-characterized.[23] The chemical steps underlying the dissolution of gold in chloride-rich, aqueous solutions are shown in reaction scheme (1):[23]

$$Au^0(s) + Cl^- \leftrightarrow Au^ICl_{Ad} + e^- \quad (1a)$$

$$xAu^ICl_{Ad} + 3xCl^- \leftrightarrow xAu^{III}Cl_4^- (aq.) + 2xe^- \quad (1b)$$

$$(1 - x)Au^ICl_{Ad} + (1 - x)Cl^- \leftrightarrow (1 - x)Au^ICl_2^- (aq.) \quad (1c)$$

where the superscripts denote the oxidation states of Au, and x is the fraction of Au^I moiety that is oxidized to $Au^{III}Cl_4^-$. Essentially, this mechanism says that the electro-dissolution of bulk gold occurs when an Au^0 atom from the solid matrix coordinates with a Cl^- atom from the solution to form the adsorbate Au^ICl_{Ad}. The solid Au^0 atom is oxidized to Au^I in this step [1(a)]. Subsequent chloride binding and oxidation yields the dissolved products $Au^{III}Cl_4^-$ (aq.) [1(b)] and $Au^ICl_2^-$ (aq.) [1(c)]. The chemical steps underlying the deposition of $Au^{(0)}$ are shown in reaction scheme (2) as follows:[23]

$$Au^{III}Cl_4^- (aq.) + 3e^- \leftrightarrow Au^0 + 4Cl^- \quad (2a)$$

$$Au^ICl_2^- (aq.) + e^- \leftrightarrow Au^0 + 2Cl^- \quad (2b)$$

These reactions imply that the electro-deposition of gold occurs when a solvated $Au^{III}Cl_4^-$ species [2(a)] or Au^ICl^- species [2(b)] arrives at the electrode which then reduces the Au^{III} or Au^I moieties to $Au^{(0)}$.

A key question regards the extent to which these processes that occur with bulk gold under DC biases accurately describe the interfacial chemistry of dendritic gold under the AC voltages that the DENA method employs. This information allows us to take the next step of developing a theoretical model for how these interfacial chemical mechanisms act in conjunction with the diffusion of $Au^{III}Cl_4^-$ through the bulk solution to enable dendritic reconfiguration. This theory indicates that our methodology functions by attaining independent control over the joining and leaving rates of atoms to the crystal, thus providing a basis for applying fully reconfigurable metallic nano-structures to substrates. Because this methodology relies on the aqueous electrochemistry of simple salts—not just gold chloride—this approach could potentially be applied in oceanic environments. As such, it has the potential to provide sustainable routes to coatings for corrosion, reflectivity, and adhesion control at immersed surfaces.

Experimental design

Fig. 1(a) depicts the set-up for controlling the dendritic growth of gold *via* the DENA technique. This method, which produces individual nanowires and nano-dendrites by electrochemical dendritic solidification, is described elsewhere.[9,21] The set-up consists of an electrode pair immersed in aqueous $HAuCl_4$ solution. The counter-electrode (CE) is composed of platinum wire (Kurt J. Lesker, 0.5 mm diameter). The working electrode (WE), which has a sharper tip, is composed of a piece of tungsten filament, the tip of which is electro-etched to a ~1 μm radius-of-curvature.[24,25] The tungsten filament (SmallParts, 0.2 mm diameter) is mounted in a 3D stage and positioned ~1 μm above a microscope slide that is mounted on an inverted microscope (Leica, IRB). The inter-electrode spacing is adjusted to ~30 μm. A 20 μl aliquot of solution composed of de-ionized (18 MΩ) water and 20.0 mM $HAuCl_4$ (Sigma Aldrich) is

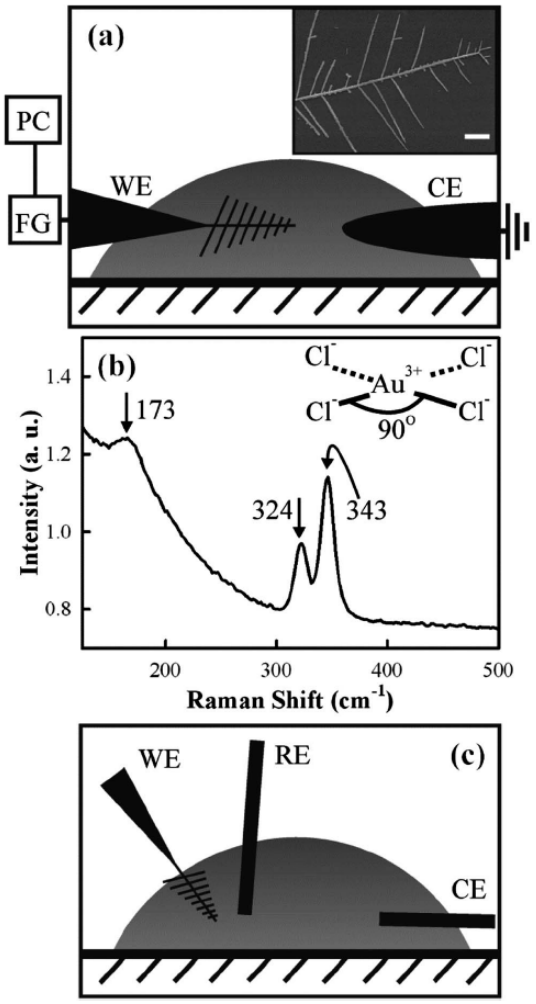

Fig. 1 (a) Schematic depicting the side-view of the experimental set-up for the growth of gold dendrites. FG designates a function generator that is controlled by a personal computer PC *via* Labview. Inset: SEM image of a gold dendrite. Scale bar = 2 μm. (b) Raman spectrum of 20.0 mM $HAuCl_4$ solution. Inset: structure of $Au^{III}Cl_4^-$ ions. (c) Schematic depicting the 3-electrode set-up used to measure cyclic voltammograms of gold dendrites. WE, RE, and CE designate the working electrode, reference electrode, and counter electrode, respectively.

deposited across the inter-electrode gap. Fig. 1(b) shows the Raman spectrum of this solution. The features at 173 cm^{-1}, 324 cm^{-1} and 343 cm^{-1} agree well with the known B_{1g} (bend), B_{2g} (asymmetric stretch), and A_{1g} (symmetric stretch) vibrational modes of $Au^{III}Cl_4^-$ (aq.), respectively,[26] implying that gold exists predominantly as $Au^{III}Cl_4^-$ in the bulk solution. A function generator (Hewlett Packard, 8116A) was used to apply a square wave voltage signal (±4.0 V, 20.0 MHz) to the working electrode while grounding the counter-electrode to induce growth of the dendrite at the sharper working electrode. Growth occurs within a range of frequencies, from 10.0 MHz to 50.0 MHz a typical gold dendrite is shown in the scanning electron micrograph in the inset of Fig. 1(a). The individual branches, which are thought to originate at random sites along sides of a dendrite due to fluctuations in the diffusion-limited $AuCl_4^-$ deposition rate,[19] have ~60 nm diameters and ~60° branching angles. We have shown elsewhere that the electron diffraction patterns collected from such dendrites quantitatively match the known diffraction patterns of bulk gold, indicating that these dendrites are composed of gold.[21] The applied potential serves to select the growth direction in the lab frame by controlling the direction of $AuCl_4^-$ flux from solution.[27] The crystallographic growth axis, however, is intrinsic to the crystal (*i.e.* in the direction of maximum surface tension).

Fig. 1(c) is a schematic depicting the 3-electrode arrangement that we employed to measure cyclic voltammagrams of individual gold dendrites and also of bulk gold samples. After growing a dendrite from the tip of the working electrode, the $HAuCl_4$ solution was gently withdrawn and replaced with 0.1 M KCl. The working electrode was pulled out of the solution *via* a translational stage until only the dendrite remained in the solution; hence, the dendrite alone served as the working electrode. This arrangement ensures that only the electrochemistry of the gold dendrite and not that of the tungsten electrode will contribute to the cyclic voltammagram. Care must be taken that the air–water surface tension does not separate the dendrite from its substrate. To attain an I–ΔV profile, a voltage supply steps the potential difference ΔV of the working electrode forward by 25.0 mV relative to an Ag/AgCl reference electrode at a rate of 25.0 mV s^{-1}. ΔV is maintained potentiostatically *via* a Pt counter-electrode during each 1.0 s increment. The design of the homebuilt potentiostat is described elsewhere.[28] In a typical cyclic scan, the cross-cell current I that flows into the working-electrode was recorded by stepping ΔV forward in time from 0.0 V to 0.9 V and then back to 0.0 V. In plotting the current, we use the IUPAC convention that a positive (negative) current corresponds to negative (positive) charge flowing into (out of) the working electrode. The plot of I *versus* ΔV constitutes a cyclic voltammagram. To measure cyclic voltammagrams of bulk gold samples, the same set-up was used except that a segment of 0.5 mm diameter gold wire (Kurt J. Lesker, 99.99% pure) was substituted for the dendrite.

Full reconfiguration of the dendrite (*i.e.* growth followed by dissolution) is induced by variation of either the frequency or the duty cycle of the voltage signal. When the frequency f of the voltage signal is used to induce reconfiguration, the amplitude is held constant (usually at 4.0 V), the duty cycle is fixed at 50.0%, and the frequency is lowered from a high value of greater than 9.0 MHz to a low value of less than 3.0 MHz. An example of frequency-induced dendritic reconfiguration is depicted in Fig. 2. When the duty cycle is used to induce reconfiguration, both the amplitude and the frequency of the voltage signal are held constant. A duty cycle of n means that the duration of the positive half cycle of the voltage signal is n % of its period f^{-1}. By increasing the duty cycle from less than 50.0% to greater than 50.0%, reconfiguration (*i.e.* growth followed by dissolution) is induced.

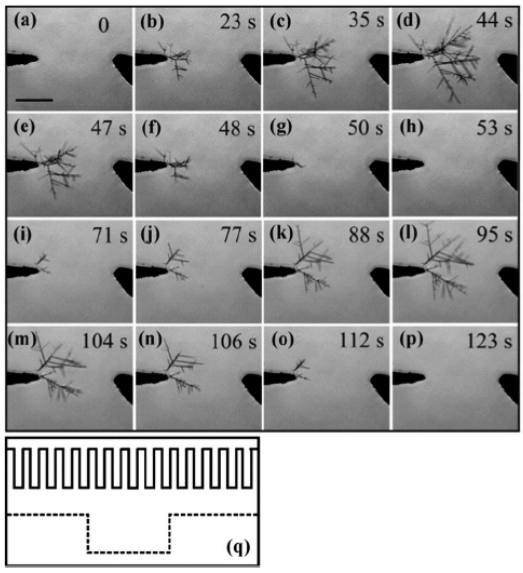

Fig. 2 (a)–(p) Optical images showing growth and dissolution of gold dendrites by twice cycling the frequency of voltage signal (4.0 V amplitude, 50% duty cycle) between 34.0 MHz and 1.0 MHz. Scale bar = 50 μm. Panels (a)–(d) and (i)–(l) designate the growth stages. Panels (e)–(h) and (m)–(p) designate the dissolution stages. (q) Schematic depicting the square-wave signal used to grow (solid line) and dissolve (dashed line) the dendrites.

A Raman microscope (iHR550 Horriba-Jobin Yvon spectrometer fiber coupled to a BX-41 Olympus upright microscope) was used to interrogate single gold dendrites immersed in 0.1 M KCl aqueous solution. The microscope was equipped with a 0.8 NA 50× objective and a 633.2 nm HeNe laser (Melles Griot), providing a diffraction-limited laser spot size of ~970 nm. To interrogate a dendrite during electrochemical growth or dissolution, the dendrite-laden tungsten filament and a platinum counter-electrode were mounted on the stage of the Raman microscope and immersed in a drop of the KCl solution. An alternating voltage signal was applied to the dendrite, which served as the working electrode in this cell. The platinum electrode, which was grounded, served as the counter-electrode in this cell.

Theory

To describe how both the interfacial and bulk diffusive subprocesses participate in the dendritic reconfiguration process, we propose the following theoretical model. We assume that

reaction schemes (1) and (2) correctly describe the *interfacial* reduction and oxidation processes that occur when the alternating voltage signal reconfigures a dendritic crystal. This assumption will be verified below. To begin, we model the diffusion of $Au^{III}Cl_4^-$ ions (which are the main source of gold that will crystallize) through the bulk solution to the crystal-solution interface. For simplicity, we regard the crystal-solution interface as flat and of constant area A with the gold concentration varying only in the x-direction. Dendritic growth is a diffusion-limited process. The diffusive flux j_D of $Au^{III}Cl_4^-$ toward the interface is:

$$j_D(x, t) = -D\nabla c(x, t) \quad (1)$$

where D is the $Au^{III}Cl_4^-$ diffusion coefficient and $c(x, t)$ is the $Au^{III}Cl_4^-$ concentration at position x in the solution and at time t.

In the DENA process, an alternating square wave voltage is applied to solidification front. During each positive half cycle, the concentration of metallic ions in solution evolves in time near the solidification front as governed by the diffusion equation and shown elsewhere.[29] We forego explicit solution of the time dependent diffusion equation here and, for simplicity, approximate the concentration profiles during a positive half cycle with the bi-linear functions shown in Fig. 3(a). During a positive half cycle, $Au^{III}Cl_4^-$ diffuses to the solidification front, giving rise to a depletion zone in the bulk. Essentially, the profiles flatten as time increases and the solution near the interface becomes more heavily depleted of $Au^{III}Cl_4^-$. These profiles in Fig. 3(a) imply concentration gradients near the interface of the form:

$$\nabla c(x, t) \approx \frac{\Delta c}{\Delta x(t)} \approx \frac{\Delta c}{\sqrt{2Dt}} \quad (2)$$

where $\Delta c = c_0 - c_{int}$ [see Fig. 3(a)]. In the second equality, Δx was equated to the diffusive root mean square displacement.[30]

When the electrode is positively biased, it is hard for the Au^{III} in the ions to be reduced, so the approaching ions build up Stern and Helmholtz layers adjacent to the electrode. Fig. 3(b) sketches this effect where only the Stern layer is shown, for clarity. Let N_S be the number of $Au^{III}Cl_4^-$ that join the Stern layer *via* diffusion from the solution during the positive half cycle:

$$N_S = \int_0^\tau j_D(x, t) A \mathrm{d}t = A\Delta c\sqrt{2D\tau} \quad (3)$$

where τ is the duration of a positive half cycle, and eqn (1) and (2) were used to arrive at the second equality.

The positive electrode is able to oxidize $Au^{(0)}$ atoms in the crystal in accordance with reaction scheme (1). As sketched in Fig. 3(b), these gold chloride ions also join the Stern and Helmholtz layers near the interface. We take the oxidative flux j_O of $Au^{III}Cl_4^-$ to the interfacial Stern layer to be essentially constant during the positive half cycle, as this flux should not depend (much) on the $Au^{III}Cl_4^-$ concentration in solution (which does change during this period).[31] Therefore, the number N_C of Au^0 that were oxidized during the positive half cycle is simply:

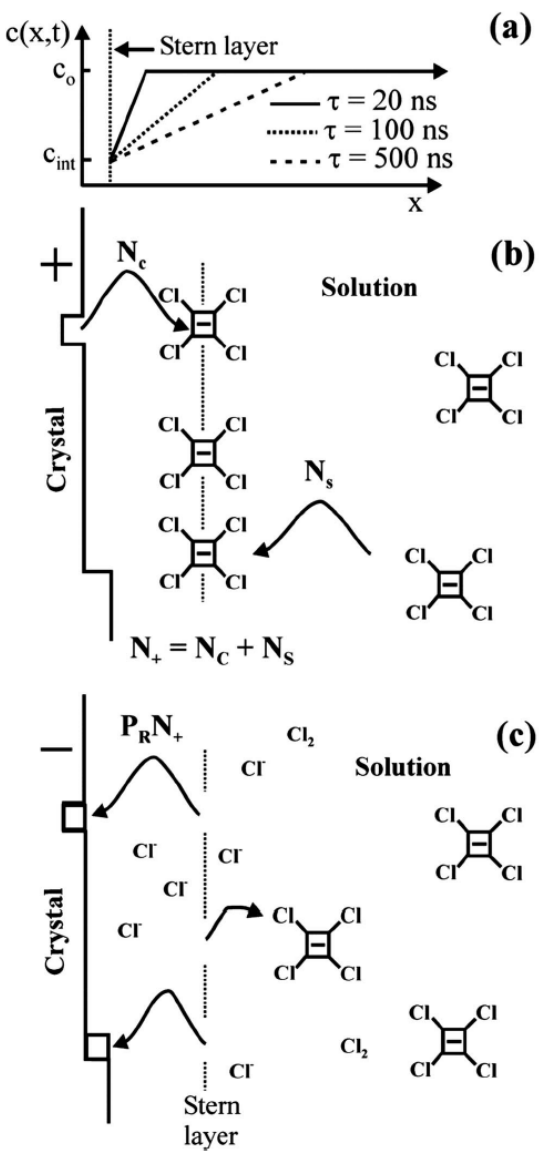

Fig. 3 (a) Concentration profiles of metallic ions in solution near the crystalline interface after increasing periods of positive bias. (b) Schematic of the spatial distribution of $Au^{III}Cl_4^-$ ions during a positive half cycle. (c) Schematic of the distribution of $Au^{III}Cl_4^-$ ions during the subsequent negative half cycle.

$$N_C = j_O A\tau \quad (4)$$

Using eqn (3) and (4), the total number of ions N_+ that join the Stern Layer during a positive half cycle of duration τ is given by the sum of N_S and N_C:

$$N_+ = A\Delta c\sqrt{2D\tau} + j_O A\tau. \quad (5)$$

Immediately after the voltage switches negative [see Fig. 3(c)], these N_+ gold chloride ions ($Au^{III}Cl_4^-$) still occupy the Stern layer, but have probability P_R of being reduced from Au^{III} to Au^0 *via* reaction scheme (2). P_R is significant when the electrode is negative, while the oxidation probability is greatly diminished. The number of Au^{III} that are reduced during this step is $P_R N_+$. When τ is adjusted to the critical value τ_C at which $P_R N_+$ equals $j_O A \tau_C$, the number of Au^0 that were oxidized during the positive half cycle, the system is in a steady state—there is neither crystallization nor dissolution:

$$P_R\left(\sqrt{2D\tau_C}\Delta c + j_O\tau_C\right) = j_O\tau_C \quad (6)$$

This condition implies an inherent time-scale τ_C for the positive half cycle duration that demarcates the growth and dissolution modes:

$$\tau_C = \frac{2D\Delta c^2}{{j_O}^2}\frac{{P_R}^2}{(1-P_R)^2} \quad (7)$$

The frequency f of the alternating voltage signal (assuming a 50% duty cycle) is $(2\tau)^{-1}$, so the predicted critical frequency f_C above which growth occurs is

$$f_C = \frac{{j_O}^2}{4D\Delta c^2}\frac{(1-P_R)^2}{{P_R}^2}. \quad (8)$$

Below this value, dissolution is predicted to occur whereas for frequencies larger than f_C, crystallization is expected.

Results

The complete structural reconfiguration of a small number of gold dendrites positioned at the tip of a sharp tungsten filament is illustrated in Fig. 2(a)–(p). This series of images was collected during a continuous 123 s period when the frequency of the voltage-signal was cycled (two times) between 34.0 MHz and 1.0 MHz. The amplitude and duty cycle were fixed at 4.0 V and 50%, respectively. The 34.0 MHz signal was initiated at $t = 0$ s. Panels (a)–(d) depict the growth of a gold dendrite over the next 44 s. At $t = 45$ s, the frequency was abruptly reduced to 1.0 MHz. Panels (e)–(h) depict the *dissolution* of the gold dendrite over the subsequent 8 s. Panels (i)–(p) illustrate the next growth–dissolution cycle. A real-time movie of this event showing 7 growth–dissolution cycles is available online, and we have observed 87 continuous growth–dissolution cycles by using a Labview control-program to cycle the function generator between high and low frequencies (not shown). This process can be automated and repeated a significant number of times. Fig. 2(q) depicts the square-wave voltage functions used to grow (solid) and dissolve (dashed) the dendrites. Essentially, the growth of gold dendrites is induced by voltage signals of frequency >10.0 MHz; dissolution is induced by voltage signals of frequency <3.0 MHz. Neither behavior is observed for frequencies between 3.0 MHz and 10.0 MHz.

Fig. 4(a) depicts a cyclic voltammagram of a bulk gold sample. As the potential of the bulk gold working electrode ΔV is stepped in the positive direction, the current I into the working electrode grows slightly positive (consistent with electrons flowing into the working electrode) and increases in magnitude with a small slope until $\Delta V \sim 0.80$ V. Beyond this point, the current magnitude increases rapidly in the positive direction as ΔV is stepped further towards 0.90 V. As established elsewhere,[32] this positive current corresponds to the dissolution of solid $Au^{(0)}$ as it is oxidized to $Au^{III}Cl_4^-$ (aq.) and $Au^{I}Cl_2^-$ (aq.). As ΔV is scanned in the reverse direction, the magnitude of I drops rapidly and flattens out such that little current is measured between 0.8 V and 0.6 V. At ~0.6 V, a negative current becomes evident, peaking at 0.55 V. This negative current corresponds to the deposition of $Au^{(0)}$ on the working electrode as $Au^{III}Cl_4^-$ (aq.) and possibly also $Au^{I}Cl_2^-$ (aq.) are reduced to $Au^{(0)}$.

Fig. 4(b) depicts a representative cyclic voltammagram of the gold dendrites shown in the inset. The voltammagram of the dendrite exhibits a forward scan showing a positive current at $\Delta V \sim 0.75$ V that rapidly increases with further voltage-increase; furthermore, this voltammagram exhibits a reverse scan showing a negative current peak at 0.53 V. The voltammagram of bulk gold in Fig. 4(a) shows these same features. This level of agreement implies that dendritic gold undergoes the same redox chemistry under DC voltages as bulk gold. That is, the

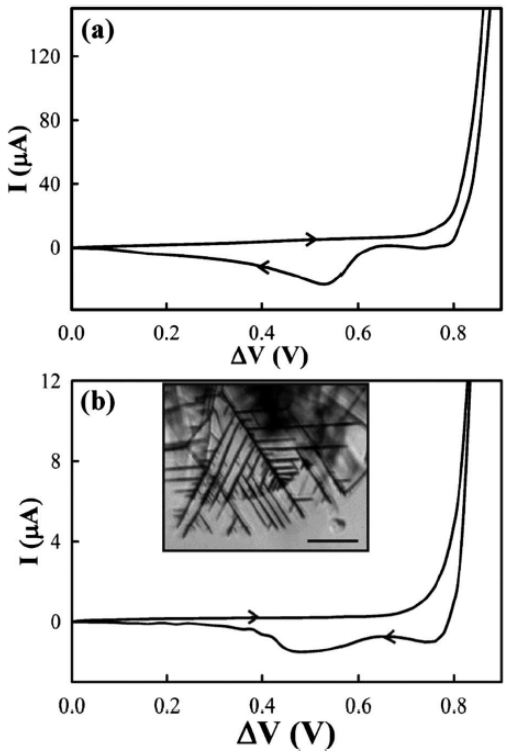

Fig. 4 (a) Cyclic voltammagrams obtained in 0.1 M KCl with a bulk gold working electrode. (b) Cyclic voltammagrams obtained in 0.1 M KCl with a dendritic gold working electrode. Scan rate = 25 mV s^{-1}. Inset: optical image of a gold dendrite. Scale bar = 30 μm (sign convention: a positive (negative) current corresponds to negative (positive) charge flowing into (out of) the working electrode).

positive current at voltages above 0.80 V corresponds to the dissolution of Au from the working electrode (*i.e.* the dendrite), as summarized by reaction scheme (1); the negative feature at 0.53 V corresponds to the deposition of gold onto the working electrode *via* the reduction of $Au^{III}Cl_4^-$ (aq.) and possibly $Au^{I}Cl_2^-$ (aq.) ions, as summarized by reaction scheme (2).

It is possible that the redox-chemistry of gold differs when it is induced by MHz-level voltage signals instead of DC voltage signals. Hence, we have employed a Raman microscope to interrogate the surface of single gold dendrites while they are dissolving under alternating voltages. Fig. 5(a) shows Raman spectra that were collected from a ~0.80 μm^2 region of a gold dendrite that was immersed in 0.1 M KCl solution. When no voltage was applied to the dendrite, a featureless spectrum was obtained (solid line). However, the application of a dissolution-inducing 500 kHz voltage-signal (4.0 V amplitude, 50% duty cycle) yielded the spectrum with a single peak at 235 cm^{-1} (dotted line). A voltage-signal having a larger, 6.0 V amplitude (but the same frequency and duty cycle) yielded the spectrum with a single peak at 250 cm^{-1} (dashed line); hence, the larger substrate bias induces a 15 cm^{-1} blue-shift of this spectral feature. It is known that the vibrational mode of the adsorbed species $AuCl_{Ad}$ is located between 230 cm^{-1} and 265 cm^{-1} and that it blue-shifts with increasing positive substrate bias.[33,34] This effect occurs because the applied voltage stiffens the Au–Cl bond that forms when a chloride atom binds to a surface gold atom. Substrate bias will not affect a randomly oriented AuCl moiety in solution. This information indicates that the 235–250 cm^{-1} feature corresponds to the surface-enhanced Raman detection of $AuCl_{Ad}$ and that the alternating voltage causes the formation $AuCl_{Ad}$ on dendritic gold in accordance with step [1(a)] of the bulk dissolution mechanism.

Fig. 5(b) shows Raman spectra that were collected while the microscope was focused ~10 μm to the side of a bulk gold sample. The surrounding solution was 0.1 M KCl, which initially contained no detectable level of $Au^{III}Cl_4^-$. When no voltage was applied to the gold, a featureless spectrum was obtained (dotted profile). However, when a 500 kHz voltage-signal (4.0 V amplitude, 50% duty cycle) was applied, a spectrum with weak shoulder at 173 ± 10 cm^{-1} and peaks at 324 ± 5 cm^{-1} and 343 ± 5 cm^{-1} was collected (solid profile). These features agree well with the B_{1g} (bend), B_{2g} (asymmetric stretch), and A_{1g} (symmetric stretch) vibrational modes of $Au^{III}Cl_4^-$ (aq.), respectively, whose spectrum is shown in Fig. 1(b). The solid profile closely resembles this spectrum. This finding implies that the application of the 500 kHz voltage signal to the gold sample produces $Au^{III}Cl_4^-$ (aq.) in the region surrounding the sample. Hence, the alternating voltage dissolves gold in accordance with step [1(c)] of the established dissolution mechanism. Attempts to observe $Au^{III}Cl_4^-$ (aq.) near dissolving nano-dendrites were not successful, most likely due to the much smaller quantity of $Au^{III}Cl_4^-$ that dendritic samples produce relative to bulk samples.

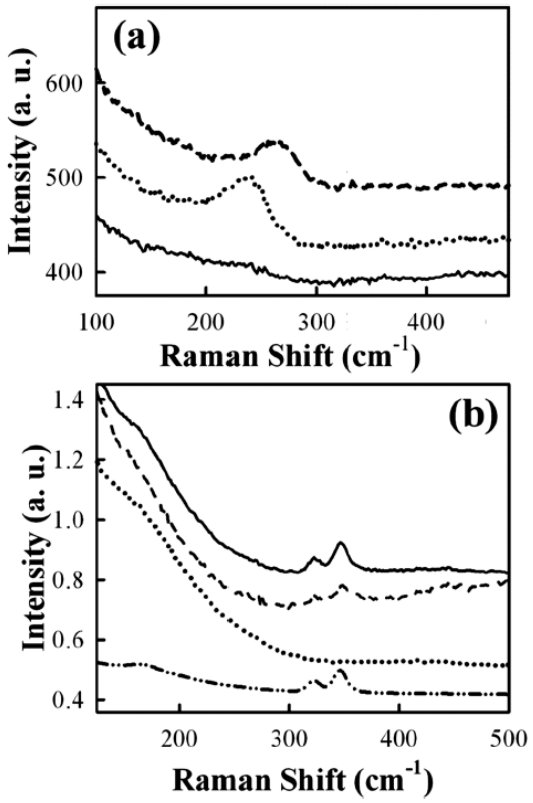

Fig. 5 (a) Raman spectrum from the surface of gold dendrite in KCl solution with the application of no voltage (solid line), 4.0 V, 500 kHz signal (dotted line), and 6.0 V, 500 kHz signal (dashed line). (b) Raman spectrum of 0.1 M KCl solution while dissolving bulk gold by a 4.0 V, 500 kHz signal (solid line); Raman spectrum of 0.1 M KCl solution with application of no voltage to the bulk gold (dotted line); Raman spectrum of gold-chloride complexes obtained from the surface of residue that was formed by evaporating the post-dissolution solution (dashed line); and for comparison, a Raman spectrum of 20.0 mM $HAuCl_4$ solution (dot-dot-dashed line).

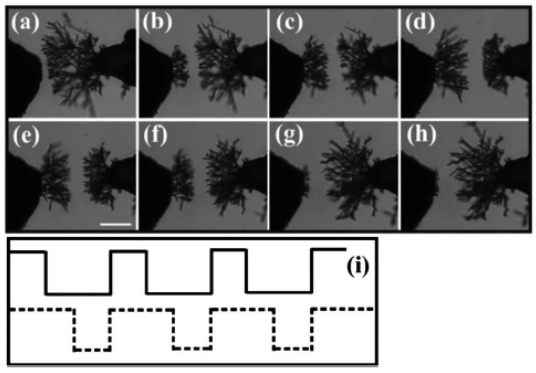

Fig. 6 Optical micrographs showing growth and dissolution of gold dendrites by cycling the duty cycle of the voltage signal (4.0 V, 6.0 MHz) between 47% and 53%. Panels (a)–(d) depict the dissolution of dendrites at right electrode (biased electrode) as induced by 53% duty cycle. Panels (e)–(h) depict the growth of dendrites at right electrode as induced by the 47% duty cycle. Scale bar = 40 μm.

The *duty cycle* of the voltage signal was also found to provide control over the reconfiguration process. Fig. 6(a)–(h) depict one growth–dissolution cycle of this behavior as induced by switching the duty cycle of the voltage signal (4.0 V, 6.0 MHz) from 47% to 53% once during the 288 s observation period. A 6.0 MHz signal was chosen because neither growth nor dissolution is observed when a 6.0 MHz signal with a 50.0% duty cycle is used, allowing any deviation from null behavior to be attributed to the duty cycle. The 53.0% signal was applied to the right electrode at $t = 0$ s. Panels (a)–(d) depict the *dissolution* of the gold dendrites on that electrode over the next 153 s. At $t = 154$ s, the duty cycle at the right electrode was abruptly reduced to 47.0%. Panels (e)–(h) depict the *growth* of gold dendrites at the right electrode over the subsequent 134 s. Because the duty cycle at the left electrode is the complement of that at the right electrode, growth (dissolution) at the left electrode occurs simultaneously with dissolution (growth) at the right electrode. A real-time movie of this event showing two growth–dissolution cycles is available online. Fig. 6(i) depicts the square-wave voltage functions used to grow (solid) and dissolve (dashed) the dendrites.

Fig. 7(a) shows a series of duty-cycle dependent Raman spectra that were collected while the microscope was focused on the interface between a bulk gold wire and a 0.1 M KCl solution. The spectrum collected shortly (~5 s) after applying a 45% voltage signal (500 kHz voltage, 4.0 V amplitude) to the working electrode is featureless (black curve). There is little change on stepping the duty cycle up to 50% (cyan). However, a peak centered at 265 cm^{-1} appears when the duty cycle is increased to 55% (pink profile). As discussed above, this feature likely denotes the adsorbate $AuCl_{Ad}$. Also apparent are weak shoulders at 173 cm^{-1}, 324 cm^{-1} and 345 cm^{-1} that denote $Au^{III}Cl_4^-$ (aq.). As the duty cycle is increased further to 60%, 65% and 70%, the

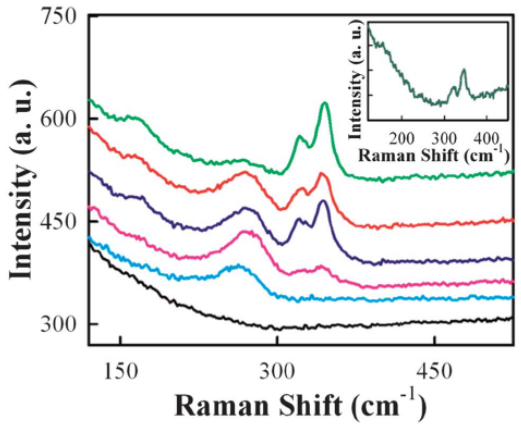

Fig. 7 Raman spectra from gold surface in 0.1 M KCl solution at 4.0 V, 500 kHz amplitude square signal with 45% duty cycle (black), 50% duty cycle (cyan), 55% duty cycle (pink), 60% duty cycle (blue), 65% duty cycle (red), and 70% duty cycle (green). Inset: Raman spectrum of residual solution (dark green) obtained after the duty cycle experiment of 5(a). Indeed, the set of peaks at 173 cm^{-1}, 324 cm^{-1} and 345 cm^{-1} indicate the presence of $AuCl_4^-$.

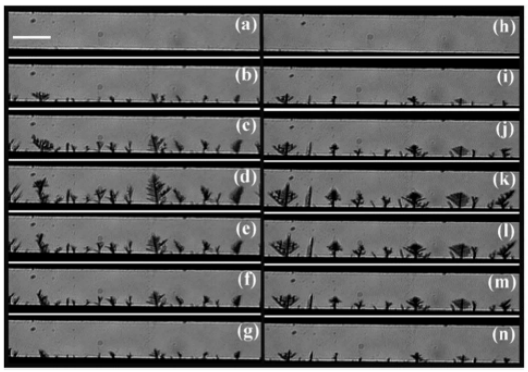

Fig. 8 Optical micrographs showing growth and dissolution (two cycles) of 1D array of gold dendrites on lithographic substrates that were obtained by twice cycling the frequency between 34.0 MHz and 1.4 MHz. Scale bar = 20 μm. Panels (a)–(d) and (h)–(k) depict the growth stage and panels (e)–(g) and (l)–(n) depict the dissolution stage of the dendrites.

$AuCl_{Ad}$ feature at 265 cm^{-1} diminishes in intensity while the $Au^{III}Cl_4^-$ peaks (at 173 cm^{-1}, 324 cm^{-1} and 345 cm^{-1}) increase in intensity. These trends suggests that increasing the duty cycle induces the dissolution of solid gold by first reducing Au^0 to the intermediate $Au^{I}Cl_{Ad}$, in accordance with step [1(a)] of reaction scheme (1). Further increase in the duty cycle causes the gold atom in this species to be reduced to the solvated species $Au^{III}Cl_4^-$ (aq.), in accordance with step [1(b)] of reaction scheme (1). The spectrum in the inset was collected from the solution after performing this study, at which point, the solution was faintly yellow, consistent with the presence of $Au^{III}Cl_4^-$ (aq.).

It is also possible to produce and reconfigure entire arrays of dendrites that coat electrode surfaces. Fig. 8 is a series of images depicting the simultaneous reconfiguration of a dozen roughly evenly spaced dendrites that are positioned along a straight 1D lithographic electrode. The horizontal field-of-view in each image is 100 μm. Panels (a)–(d) illustrate the growth of these dendrites over a 12 s period, as induced by a voltage-signal (8.0 V, 34 MHz, 50% duty cycle) applied to the (lower) working electrode while grounding the (upper) counter-electrode. Panels (e)–(h) depict the complete dissolution of these dendrites over the following 7 s, as induced by reducing the frequency to 1.4 MHz. Panels (i)–(n) illustrate the subsequent reconfiguration cycle. An online movie, from which these snapshots were taken, illustrates 7 reconfiguration cycles. While the shapes of the individual dendrites differ, their growth and dissolution rates are essentially uniform: at a given time (*i.e.* panel), the dendrites have common heights. This 1D forest of dendrites extends along the entire 0.225 mm length of the immersed electrode (not shown).

Discussion

Causing dissolution of a crystal is the key step that makes dendritic crystallization a reconfigurable process. This paper shows that changes in the MHz-level frequencies of voltages

that are applied to the dendrites induce their dissolution. To better understand how this process occurs, we have characterized the redox chemistry of the crystal-solution interface during dissolution. Close similarity between the cyclic voltammagrams of bulk and dendritic gold [Fig. 4(a) and (b), respectively] imply that both materials grow and dissolve *under DC voltages via* the same chemical steps [reaction schemes (1) and (2)]. To interrogate the reconfiguration chemistry *under alternating voltages*, we have employed Raman microscopy. These studies have established that the adsorbate $AuCl_{Ad}$ forms on the dendrite–surface when <3.0 MHz voltage signals, which induce dissolution, are applied to the dendrite [Fig. 5(a)]. This finding is in agreement with step [1(a)] of the bulk dissolution mechanism [reaction scheme (1)]. We have also observed a Raman signal indicating that $Au^{III}Cl_4^-$ (aq.) is produced when this voltage is applied to the gold samples. This finding is in accordance with step [1(c)] of the bulk dissolution mechanism. Structural reconfiguration of dendritic gold is also induced by changes in the duty cycle of the voltage-signals that are applied to the dendrites. As discussed above, increasing (decreasing) the duty cycle to values greater (less) than 50.0% causes the dendrite to dissolve (grow) [Fig. 6(a)–(h)]. Raman analysis indicates that reaction scheme (1) accurately describes how dissolution occurs when duty cycles >50.0% are applied [Fig. 7]. Taken together, these observations indicate that the same dissolution mechanism that occurs under DC voltages (and which is well understood) provides an accurate description of the dissolution portion of the dendrite reconfiguration mechanism.

This analysis provides confidence that reaction schemes (1) and (2) accurately describe the *interfacial* atom-joining and atom-leaving processes that occurs during dendritic reconfiguration and, thereby, validates our use of these reaction schemes in the theoretical formulation presented above. This theory predicts a critical frequency f_C [eqn (8)] for the alternating voltage, above which there is growth and below which there is dissolution. We use the following values in eqn (8) in order to compute the critical frequency. An estimate for the diffusivity D is calculated *via* application of the Stokes–Einstein relation to an $Au^{III}Cl_4^-$ ion of radius $a \sim 4.5 \times 10^{-10}$ m in aqueous solution of viscosity 1×10^{-3} kg m^{-1} s^{-1} having thermal energy $k_BT \sim 4.1 \times 10^{-21}$ J: $D \sim k_BT/(6\pi\eta a) = 4.8 \times 10^{-10}$ m s^{-2}; if we assume that the interfacial concentration of $Au^{III}Cl_4^-$ is ~½ the bulk concentration of 20 mM, then $\Delta c \sim 10$ mM $= 0.5 \times 10^{25}$ m^{-3}. An estimate for oxidative flux j_O is obtained through the observation that a typical gold dendrite of number density $\rho \sim 6 \times 10^{28}$ m^{-3} dissolves at a rate of $v_D \sim 5$ μm s^{-1}; thus $j_O \sim \rho v_D = 3.0 \times 10^{23}$ m^{-2} s^{-1}. The reduction probability during the negative half cycle (P_R) must lie between 0 and 1. Here, we assume a value of $P_R \sim 0.5$. This number seems reasonable as P_R is expected to be significant due to the availability of electrons on the negative dendrite (with which to reduce $Au^{III}Cl_4^-$), but should not be as high as unity due to electrostatic repulsion between the electrode and $Au^{III}Cl_4^-$. Substitution of these values into (8) yields $f_C \sim 1.8$ MHz. Experimentally, we observe the critical frequency to be ~3.0 MHz, so prediction and observation are in reasonable agreement. Qualitative agreement is all that should be expected of this theory, given its approximate treatment of the diffusion equation. Nevertheless, this approach addresses the effects of both the interfacial chemistry and the bulk diffusion of $Au^{III}Cl_4^-$ to illustrate how imbalance between the interfacial and diffusive rates causes either growth or dissolution of dendritic crystals.

This theory also provides an explanation for why variation of the duty cycle induces reconfiguration. Increasing the duty cycle lengthens the duration that the dendrite is positively biased relative to its duration of negative bias. According to the theory, such a change will enhance the extent of dissolution during a complete voltage cycle and reduce the extent of reduction (*i.e.* deposition); hence, dendrites are expected to dissolve under duty cycles >50.0%, as observed. Conversely, reducing the duty cycle shortens the duration that the dendrite is positively biased. This change will retard the extent of dissolution during a compete cycle and enhance the extent of deposition. Hence, dendrites are expected to grow when the duty cycle is less than 50.0%, as observed.

As an extension of the basic reconfiguration-process that *individual* dendrites exhibit, we have demonstrated the reconfiguration of *macroscopic arrays* of dendrites. Fig. 8 illustrates the on-command growth and dissolution of 1D forests of dendrites that extend along the entire (0.25 mm) length of an immersed electrode. In future work, we envision extending this capability to produce regenerative 2D dendritic arrays.

Conclusions

This work presents an electrochemical method for inducing the complete structural reconfiguration of metallic nano-dendrites. Essentially, we cause a dendrite, or an array of dendrites, to grow, dissolve, and grow again in an on-command and repeatable manner. Our observations strongly suggest that the alternating voltages used in the DENA technique cause gold nano-dendrites to grow and dissolve by the same reduction and oxidation mechanisms that bulk gold samples exhibit under DC voltages. A simple theoretical model that accounts for both of these interfacial chemical processes as well as the bulk diffusion of $Au^{III}Cl_4^-$ through the solution succeeds, at least on a semi-quantitative-level, in describing how the dendritic reconfiguration mechanism works. Essentially, the frequency and the duty cycle of the alternating voltage signal control the imbalance between interfacial and diffusive processes to cause either growth or dissolution of dendritic crystals.

A goal for the near future will be to produce fully reconfigurable 2D dendritic arrays. We expect this to be readily achievable as an example of a 2D dendritic array has already been reported.[35] Such a step would provide an innovative way to coat surfaces with nano-structured dendrites in a reconfigurable manner. DENA provides control over both the overall size and the branch-diameter[29] of a dendrite, thereby providing both micro- and nanoscale control; hence, 2D arrays of such structures hold promise as surface modifications that provide reconfigurable or self-healing wettability and adhesion control of the Baxter–Cassie type.[36,37] As a reasonably wide range of metals undergoes dendritic solidification—not just gold, new strategies for anodic protection of metallic surfaces immersed in corrosive environments, such as seawater, become possible. One example is the deposition of 2D forests of Mg or Zn

dendrites onto immersed surfaces in order to serve as rechargeable sacrificial anodes that would be inexpensive and widely available. Finally, given that the plasmonic resonances of the nano-dendrites will alter the color and specular reflectance of a surface that is coated with such an array, variation of the optical properties of the surface may also be achieved.

Acknowledgements

This work was partially supported by National Science Foundation grants PHY-0646966, ECCS-0601362, EAR-0722410. We thank Professor Larry Weaver for countless offerings of insightful theoretical assistance.

Notes and references

1 L. Wang, L. Xu, H. Kuang, C. Xu and N. A. Kotov, *Acc. Chem. Res.*, 2012, **45**, 1916–1926.
2 R. Hanlon, *Curr. Biol.*, 2007, **17**, R400–R404.
3 B. Brown and S. Gibb, *J. Exp. Mar. Biol. Ecol.*, 2002, **277**, 129–144.
4 T. Z. Grove, C. O. Osuji, J. D. Forster, E. R. Dufresne and L. Regan, *J. Am. Chem. Soc.*, 2010, **132**, 14024–14026.
5 S. Sacanna, L. Rossi and D. J. Pine, *J. Am. Chem. Soc.*, 2012, **134**, 6112–6115.
6 W. H. Hilbertz, *IEEE J. Oceanic Eng.*, 1979, **OE-4**, 94–113.
7 A. Neville and A. P. Morizot, *J. Cryst. Growth*, 2002, **243**, 490–502.
8 M. H. Lee, K. M. Moon, J. D. Kim, K. Jun and K. H. Kim, *Trans. Nonferrous Met. Soc. China*, 2009, **19**, s110–s113.
9 B. N. Flanders, *Mod. Phys. Lett. B*, 2012, **26**, 1130001.
10 G. E. Nash and M. E. Glicksman, *Acta Metall.*, 1974, **22**, 1291.
11 S. C. Huang and M. E. Glicksman, *Acta Metall.*, 1981, **29**, 701–715.
12 S. C. Huang and M. E. Glicksman, *Acta Metall.*, 1981, **29**, 717–734.
13 J. S. Langer, *Rev. Mod. Phys.*, 1980, **52**, 1–28.
14 D. A. Kessler, J. Koplik and H. Levine, *Adv. Phys.*, 1988, **37**, 255–339.
15 K. Libbrecht, *Field Guide to Snowflakes*, Voyageur Press, St. Paul, 2006.
16 G. P. Ivantsov, *Dokl. Akad. Nauk*, 1947, **58**, 567.
17 Y. Saito, *Statistical Physics of Crystal Growth*, World Scientific, River Edge, 1996.
18 W. W. Mullins and R. F. Sekerka, *J. Appl. Phys.*, 1964, **35**, 444–451.
19 Y. Saito, G. Goldbeck-Wood and H. Müller-Krumbhaar, *Phys. Rev. Lett.*, 1987, **58**, 1541–1543.
20 I. Talukdar, B. Ozturk, T. D. Mishima and B. N. Flanders, *Appl. Phys. Lett.*, 2006, **88**, 221907.
21 B. Ozturk, T. Mishima, D. R. Grischkowsky and B. N. Flanders, *Nanotechnology*, 2007, **18**, 175707.
22 J. K. Kawasaki and C. B. Arnold, *Nano Lett.*, 2011, **11**, 781–785.
23 M. A. Diaz, G. H. Kelsall and N. J. Welham, *J. Electroanal. Chem.*, 1993, **361**, 25–38.
24 Y. Qiao, J. Chen, X. Guo, D. Cantrell, R. Ruoff and J. Troy, *Nanotechnology*, 2005, **16**, 1598–1602.
25 G. Paneru, P. S. Thapa, S. P. Mcbride, A. Ramm, B. M. Law and B. N. Flanders, *Nanotechnology*, 2012, **23**, 455105.
26 B. H. Loo, *J. Phys. Chem.*, 1982, **86**, 433–437.
27 P. S. Thapa, B. J. Ackerson, D. R. Grischkowsky and B. N. Flanders, *Nanotechnology*, 2009, **20**, 235307.
28 A. J. Bard and L. R. Faulkner, *Electrochemical Methods: Fundamentals and Applications*, John Wiley & Sons, New York, 1980.
29 B. Ozturk, I. Talukdar and B. N. Flanders, *Nanotechnology*, 2007, **18**, 365302.
30 N. Ibl, *Surf. Technol.*, 1980, **10**, 81–104.
31 S. K. Ma, *Statistical Mechanics*, World Scientific, Philadelphia, 1985.
32 J. Herrera-Gallego, C. E. Castellano, A. J. Calandra and A. J. Arvia, 1976.
33 B. M. Abraham, K. Miyano, J. B. Ketterson and S. Q. Xu, *Phys. Rev. Lett.*, 1983, **51**, 1975–1978.
34 P. Gao and M. J. Weaver, *J. Phys. Chem.*, 1986, **90**, 4057–4063.
35 K. M. Watling and G. A. Hope, in *International Conference on Nanoscience and Nanotechnology*, IEEE, Brisbane, Austrailia, 2006, pp. 198–201.
36 K. Liu, X. Yao and L. Jiang, *Chem. Soc. Rev.*, 2010, **39**, 3240–3255.
37 A. B. D. Cassie and S. Baxter, *Trans. Faraday Soc.*, 1944, **40**, 546–551.